AN EXPERIMENTAL STUDY OF THE CABIBBO SUPPRESSED DECAY $D^0 \to K^+K^-\pi^+\pi^-$

A Dissertation submitted to the

Division of Research and Advanced Studies
of the University of Cincinnati

in partial fulfillment of the
requirements for the degree of

DOCTOR OF PHILOSOPHY

in the Department of Physics
of the College of Arts and Sciences

November, 1995

by

Lalith P. Perera

B.Sc. University of Moratuwa, Sri Lanka, 1985
M.S. University of Cincinnati, 1992

Committee Chair: Michael D. Sokoloff

Abstract

I report the measurements of branching ratio and the resonant substructure of the Cabibbo suppressed decay $D^0 \to K^+K^-\pi^+\pi^-$ using data from the Fermilab fixed target hadroproduction Experiment E791

$D^0 \to K^+K^-\pi^+\pi^-$ branching ratio was measured normalizing to the topologically similar decay$D^0 \to K^-\pi^-\pi^+\pi^+$. $D^0 \to K^+K^-\pi^+\pi^-$ branching ratio is estimated to be $0.254 \pm 0.030 \pm 0.033$. A coherent amplitude analysis technique was used to estimate the relative fractions of different resonant modes contributing to the decay. A strong ϕ signal from D^0 is observed and the fractional contribution from all modes containing ϕ is estimated to be $0.18 \pm 0.05 \pm 0.06$. Fractional contribution from $\phi\rho$ mode is measured as $0.21 \pm 0.10 \pm 0.08$. A 90% confidence upper limit of 0.28 is set for the fractional contribution from $K^{*0}\overline{K^{*0}}$ mode. There are no convincing evidence for the presence of $K^{*0}K^-\pi^+$ $\overline{K^{*0}}K^+\pi^-$, $K(1400)^{\pm}K^{\mp}$ or $K(1270)^{\pm}K^{\mp}$ type modes.

Acknowledgements

High energy physics experiments involve highly collaborative efforts and I had the fortune of working with outstanding colleagues at the Fermilab E791 collaboration. I am grateful to all of them for their efforts and achievements conducting a successful experiment and giving me the opportunity to participate.

I wish to express my gratefulness to my thesis advisor Mike Sokoloff for his academic nourishment, guidance, and support while allowing a high level of independence in my work. I enjoyed working with Mike and most thankful for his understanding, encouragement, and help.

I thank the faculty, staff and friends at the Physics Department of the University of Cincinnati. I am especially grateful to Rohana Wijewardana for his friendship, advice, and help which were available whenever needed. I thank Brian Meadows for his help in my analysis work and informative and enjoyable discussions. My thanks to Joseph Scanio and Howard Jackson for serving in my thesis committee and to Peg Franz for her numerous help.

I spent some of my time working in E815 (Nu-TeV) experiment at Fermilab, which was a valuable experience. I thank all members of the E815 collaboration. I am especially grateful to Randy Johnson, my advisor to E815 work. I enjoyed working with Randy and always had something to learn from him. I am thankful to all friends and colleges at the Fermilab, especially to Jean Slaughter and Janet Conrad for their kind help.

I thank Jeff Apple, Milind Purohit, Lucien Cremaldi, Keith Throne, Fritz DeJongh and others who helped in my work various ways.

I wish to express my heartful gratitude to late Professor Cyril Ponnamperuma,

former Director of the Institute of Fundamental Studies, Sri Lanka. I am indebted to him for his kindness, help, and encouragement while I was working there, which paved the way for my graduate studies in the United States.

There are many more people than I could mention here who have helped me in various ways. I am sure all of you know that I am grateful to you.

Contents

1 Introduction **1**

1.1 2

1.1.1 The Standard Model 2

1.1.2 Weak Interactions 3

1.1.3 Strong Interactions 5

1.1.4 Weak Decays of Charmd Mesons 5

1.2 BSW Model of Charm Decays 7

1.3 The Decay $D^0 \to K^+K^-\pi^+\pi^-$ 12

1.3.1 Previous Measurements of $D^0 \to K^+K^-\pi^+\pi^-$ 14

1.3.2 Summary 15

2 Experimental Setup **17**

2.1 The Detector 18

2.1.1 Beam Line and Beam Tracking System 18

2.1.2 The Target 19

2.1.3 Interaction Trigger Counters 21

2.1.4 Silicon Microstrip Detectors (SMDs) 21

2.1.5 Drift Chambers 22

2.1.6 Proportional Wire Chambers 24

2.1.7 Analysis Magnets 24
2.1.8 Cherenkov Counters 25
2.1.9 Calorimetry 26
2.1.10 The Muon Wall 27
2.2 Trigger and Data Acquisition System 29
2.2.1 The Trigger 29
2.2.2 Data Acquisition System 29

3 Event Reconstruction and Selection 31
3.1 Event Reconstruction and Filtering 32
3.1.1 Track Reconstruction. 32
3.1.2 Vertex Reconstruction: 34
3.1.3 Cherenkov Reconstruction 34
3.1.4 Filtering 35
3.1.5 Stripping 36
3.2 Substripping 38
3.2.1 Micro Stripping 40

4 $D^0 \to K^+K^-\pi^+\pi^-$ Branching Ratio 45
4.1 Monte Carlo 45
4.2 Optimization of Analysis Cuts 46
4.2.1 D^0 events from D^* s 50
4.3 Relative Branching Ratio 55
4.4 Systematic Errors 56
4.4.1 Errors due to the Background Shape. 56
4.4.2 Biases in the Selection Criteria 59
4.4.3 Variation of the Acceptance over the Phase Space 61

4.4.4 Charm Backgrounds 61
4.4.5 Correction for Kaon Cherenkov Efficiency. 62

5 $D^0 \to K^+K^-\pi^+\pi^-$ Resonant Substructure 67

5.1 Resonant Mass Distributions 67
5.2 The Fitting Technique 76
5.2.1 The Likelihood Function 76
5.2.2 Signal Probability Distribution Function. 77
5.2.3 Background Probability Distribution. 79
5.2.4 Final form of the Likelihood function 81
5.2.5 Evaluation of integrals 82
5.2.6 Normalized Physical Fractions 82
5.2.7 Fraction of Subset 84
5.2.8 Signal Matrix Elements 84
5.2.9 Background Amplitudes 87
5.3 Fit to $D^0 \to K^+K^-\pi^+\pi^-$ 88
5.3.1 Selection of Decay Modes 88
5.3.2 Signal and Background PDFs 88
5.3.3 The Fitting Process 90
5.3.4 Projections from the Fit 92
5.3.5 Total ϕ signal 93
5.3.6 Interpretation of Fit Results 95
5.4 Systematic Errors: 102
5.4.1 Widths and Masses of Resonances 103
5.4.2 Systematic Differences between Monte Carlo and Data 103
5.4.3 Width, Mass and Background of D^0 signal. 105
5.4.4 Finite size of the Monte Carlo Sample Used: 105

5.4.5 Possible Presence of Additional Amplitudes 105
5.4.6 Error in N_p 107
5.5 Goodness of the Fit 107

6 Conclusions **111**

A Widths and Form Factors **114**

List of Figures

1.1 Charged current and neutral current diagrams of weak gauge bosons . 5

1.2 Hadronic and semileptonic decay of the c quark 6

1.3 Possible decay mechanisms of $D^0 \to \overline{K^0}\phi$ decay with final state rescattering 7

1.4 D decay mechanisms 8

1.5 One-loop gluon corrections 8

1.6 Feynman diagrams for a few resonant modes which might contribute to $D^0 \to K^+K^-\pi^+\pi^-$ 13

2.1 E791 Spectrometer 20

2.2 E791 Target and pretrigger counter region (not to scale) 21

2.3 Different view directions defined in E791. The z axis points into the paper. (The measurment direction shown is orthognal to the corresponding strip direction.) 22

2.4 Expected number of photo electrons produced in Cherenkov counters for π, K^+ and protons assuming refractive index and detector are uniform with wave length 26

3.1 Geometry of a typical reconstructed E791 event in the target region . 38

3.2 Data Selection for the $D^0 \to K^-K^+\pi^-\pi^+$ analysis. Amount of data reduction in each stage is given in parentheses 41
3.3 $K\pi\pi\pi$ and $KK\pi\pi$ invariant mass distributions from SEED4 and SEED3 events with strip level cuts 44

4.1 Comparison of background subtracted parameter distributions for data and MonteCarlo 47
4.2 Parameter distributions of background and background subtracted signal region for $D^0 \to KK\pi\pi$ SEED4 events. 48
4.3 Parameter distributions of background and background subtracted signal region for $D^0 \to KK\pi\pi$ SEED3 events. 49
4.4 D^{*+} signal and ΔM distribution from $D^0 \to K\pi\pi\pi$ stripped events. . 50
4.5 $D^0 \to K^-\pi^+\pi^+\pi^-$ signal from cuts optimized for $D^0 \to K^-K^+\pi^+\pi^-$. 52
4.6 $D^0 \to K^+K^-\pi^+\pi^-$ signal from different cut categories. 53
4.7 $K^+K^-\pi^+\pi^-$ mass distributions from events with different tags. . . . 54
4.8 Total $D^0 \to K^+K^-\pi^+\pi^-$ and $D^0 \to K^-\pi^+\pi^-\pi^-$ signals after the analysis cuts. 55
4.9 Fit projections on the $KK\pi\pi$ and $K\pi\pi\pi$ mass plots (with linear background shapes) 58
4.10 Fit projections on the $KK\pi\pi$ and $K\pi\pi\pi$ mass plots with quadratic background shapes. 60
4.11 $K^+K^-\pi^+\pi^-$ mass plots from decay modes that can be misidentified as $D^0 \to K^-K^+\pi^-\pi^+$ 63
4.12 $K^+K^-\pi^+\pi^-$ mass plots from 142000 $D^0 \to K^-K^+\pi^-\pi^+$ Monte Carlo events 64
4.13 $K^-\pi^-\pi^+\pi^-$ mass plots with and without Cherenkov cut 65

5.1 Invariant mass distributions of $K\pi$ and KK versus $KK\pi\pi$ mass . . . 69

5.2 Invariant mass distributions of $\pi\pi$, $K\pi\pi$ versus $KK\pi\pi$ mass 70
5.3 Invariant mass distributions for possible resonances for events in the D^0 signal region 71
5.4 One dimensional mass distributions for events in the signal and background regions 72
5.5 Invariant mass distributions from $D^0 \rightarrow K^+K^-\pi^+\pi^-$ phase space Monte Carlo events 73
5.6 Invariant mass distributions from $D^0 \rightarrow K^{*0}(892)K^-\pi^+$ Monte Carlo events 74
5.7 Invariant mass distributions from $D^0 \rightarrow \phi\pi^-\pi^+$ Monte Carlo events . 75
5.8 $K\pi$ mass distributions for events in the D^0 signal region with D^{*+} tag 89
5.9 Fit projection on $KK\pi\pi$ mass distribution. 92
5.10 Events pass and does not pass the ϕ mass cut 93
5.11 Fit projections for events in the D^0 signal region 97
5.12 Fit projection for events in the background region 98
5.13 Mass distributions from Monte Carlo events generated according to fit results 109

A.1 projections of the fit for $K^{*0}(892) \rightarrow K^+\pi^-$ and $\phi \rightarrow K^+K^-$ signals. 116

List of Tables

1.1 Elementary particles of the Standard Model 3

1.2 Fundamental interactions. (relative strength in terms of the coupling for a proton. m_p=mass of the proton) 4

1.3 A few BSW predictions for spectator decays of D^0 [7] 11

1.4 BDM predictions for a few $D \to VV$ type decays [14] 12

1.5 Some possible Decay Modes of $D^0 \to K^+K^-\pi^+\pi^-$ 14

1.6 Previous measurements of $D^0 \to K^+K^-\pi^+\pi^-$ and resonant substrucrure. 15

1.7 Theoretical predictions of few decay modes contributing to $D^0 \to K^+K^-\pi^+\pi^-$ 16

2.1 Charm experiments at the Tagged Photon Lab 18

2.2 The beam tracking SMD and the PWC parameters.(* strips were grouped in pairs and read together) 19

2.3 E791 Target parameters 19

2.4 main characteristics of down stream SMD system (* in these planes the outer strips were read out together, thus increasing the effective width of these strips) 23

2.5 Drift Chamber Characteristics 24

2.6 Analysis Magnet Characteristics 25

2.7 Characteristics of the Cherenkov counters 25

2.8 Main parameters of the SLIC. 27
2.9 characteristics of the hadron calorimeter. 28

3.1 Number of events reconstructed for E791 at different computer farms. 32
3.2 Assingment of regions for tracks 33
3.3 particles *a priori* probabilities used in E791 36
3.4 Typical filter selection cuts 37
3.5 Summary of three and four prong strip cuts. 37
3.6 $D^0 \to KK\pi\pi$ and $D^0 \to K\pi\pi\pi$ event selection cuts 42
3.7 Event selection cuts used in the final analysis substrip. 43

4.1 Optimized analysis cuts 51
4.2 MINUIT results for the relative branching ratio fit (without the Cherenkov correction). 57
4.3 Fluctuation of the branching ratio with analysis cuts. 59
4.4 Relative branching ratio with different cuts. 61
4.5 Reconstruction efficiency for different D^0 decay modes 62
4.6 Systematic errors for the branching ratio measurement 65

5.1 properties of some possible resonances in $D^0 \to KK\pi\pi$ [29] 76
5.2 Decay modes selected for the fit 89
5.3 A typical Fit result from MINUIT 96
5.4 Fit results for different fits. 99
5.5 Continuation of Table 5.4 100
5.6 Continuation of Table 5.4 101
5.7 Variation of fit results with the width of the resonances. 103
5.8 Fit results with different cuts applied on $KK\pi\pi$ events 104
5.9 N_i and E_{ij} calculated with different subsets of Monte Carlo. 106

5.10 Estimate of systematic errors for fractional contributions 107
5.11 Fractional contributions with systematic errors 107
5.12 Fit results for Monte Carlo events generated with a given distribution 108
5.13 Fit results with different amplitudes for Monte Carlo events generated according to fit 1 results of Table 5.4 110

6.1 Comparison of E791 (this thesis results) with other measurements. . . 112
6.2 Comparison of E791 results with theoretical predictions 113

A.1 Fit results for $K^{*0}(892)$ and ϕ 115

Chapter 1

Introduction

Ever since the discovery of the J/ψ, more than twenty years ago, charm physics has remained an interesting and active area of investigation. Charm is the lightest of the heavy quarks and provides an intermediate state extending the knowledge from lighter flavors to heavy quark physics. Because many more hadrons are produced containing a charm quark than heavier flavors, it is more easily accessible in experiments than other heavy quarks.

A complete theoretical description of charmed particle decays based on general principles is not yet possible. Although considerable progress has made in areas such as heavy quark effective theories and factorization methods [1] [2] in understanding the physical processes underlying the heavy quark systems, knowledge in this area is still rather incomplete. The weak decay mechanisms apply to charm decays at the bare quark level, while what is observed are hadronized particles under strong interaction. Energies involved in charm decays are in the nonperturbative regime of strong interaction, which makes it difficult to understand the underlying physical process. Detailed analysis of various hadronic charm decays provides some useful insights in understanding heavy quarks physics.

All phenomenological models describing charmed decays that have been developed so far are only applicable to two body decays. However, detailed experimental studies of three body and four-body charm decays have shown that [3] [4] [5] those final status are dominated by contributions from two-body decay modes involving intermediate resonances. Therefore, it will be interesting and important to study resonant structure of more multibody decays. In this thesis I report a detailed experimental analysis of the Cabibbo suppressed decay $D^0 \to K^+K^-\pi^+\pi^-$.

1.1

1.1.1 The Standard Model

The main objective in particle physics is to identify the nature of matter, its constituents and laws governing its behavior in the hope that they will turn out to be simple and understandable. The standard model (of particle physics) is the most successful explanation of the fundamental structure of matter we have today. It is based on the assumption that, at the most fundamental level, matter is composed of a few basic constituents which are point-like particles (fermions), and the interactions between them which are caused by the exchange of another class of fundamental particles called gauge bosons. Quantum field theory is the basic theoretical framework used in understanding the behavior of fundamental particles and the interactions governing them. In these field theories, the invariance of observable physics under continuous phase changes of the underlying matter fields requires the existence of gauge particles.

The standard model of particle physics is an $SU(3) \times SU(2) \times SU(1)$ gauge field theory which incorporates the strong , weak, and electromagnetic interactions. The other known force, gravity, has not yet been included in this picture (Table 1.2)

type	particles			spin	electric charge
quarks	up (u)	charm (c)	top (t)	1/2	2/3
	down (d)	strange (s)	bottom (b)	1/2	-1/3
leptons	electron (e)	muon (μ)	tau (τ)	1/2	1
	e neutrino (ν_e)	μ neutrino (ν_μ)	τ neutrino (ν_τ)	1/2	0
Gauge bosons	photon (γ)	Z boson		1	0
	$W^\pm$ bosons			1	± 1
	8 gluons (g)			1	0
Higgs	Higgs boson (h)				

Table 1.1: Elementary particles of the Standard Model

All fundamental fermions in the standard model (Table 1.1) are divided into two classes, quarks and leptons, depending on whether they are subject to the strong interaction or not. It appears that these particles are grouped into three families although the reason for such grouping is not clear.

$$\begin{pmatrix} u & e \\ d & \nu_e \end{pmatrix} \begin{pmatrix} c & \mu \\ s & \nu_\mu \end{pmatrix} \begin{pmatrix} t & \tau \\ b & \nu_\tau \end{pmatrix} \tag{1.1}$$

1.1.2 Weak Interactions

In the standard model, weak and electromagnetic interactions are described by a unified $SU(2) \times SU(1)$ gauge symmetry. It involves four gauge bosons: W^+ and W^- which are responsible for flavor changing charged current interactions, Z which leads to flavor conserving weak neutral currents (Figure 1.1) and the photon which mediates the electromagnetic interaction.

The eigenstates of the weak interaction Hamiltonian differ from the flavor eigenstates. Thus the weak eiganstates $d^{'}$, $s^{'}$, and $b^{'}$ are superpositions of the d, s, and b mass eigenstates. The relation between the mass eigenstates and weak eigenstates is

interaction	relative strength	gauge boson	participants
strong	$\frac{g^2}{4\pi} = 0.1 - 0.5$	gluons	quarks, gluons
electromagnetic	$\frac{e^2}{4\pi}\frac{1}{137}$	photon	all electrically charged particles
weak	$G_F m_p^2 = 10^{-5}$	W and Z	all except photon and gluons
gravity	$G m_p^2 = 10^{-36}$	graviton (?)	all

Table 1.2: Fundamental interactions. (relative strength in terms of the coupling for a proton. m_p=mass of the proton)

given by the Cabibbo-Kobayashi-Maskawa (CKM) matrix.

$$\begin{pmatrix} d' \\ s' \\ b' \end{pmatrix} = \begin{pmatrix} V_{ud} & V_{us} & V_{ub} \\ V_{cd} & V_{cs} & V_{cb} \\ V_{td} & V_{ts} & V_{tb} \end{pmatrix} \begin{pmatrix} d \\ s \\ b \end{pmatrix} \tag{1.2}$$

To a high degree of accuracy, the first two families are related by

$$\begin{pmatrix} d' \\ s' \end{pmatrix} = \begin{pmatrix} \cos\theta_c & \sin\theta_c \\ -\sin\theta_c & \cos\theta_c \end{pmatrix} \begin{pmatrix} d \\ s \end{pmatrix}. \tag{1.3}$$

The angle θ_c (known as the Cabibbo angle) determines the weak coupling of the c quark to a s or d quark (hence the weak decay rate). Since the value of θ_c is small ($\theta_c = 0.21$), $c \to d$ decays are suppressed by a factor $\tan^2\theta_c$ compared to $c \to s$ decays. This is known as Cabibbo suppression.

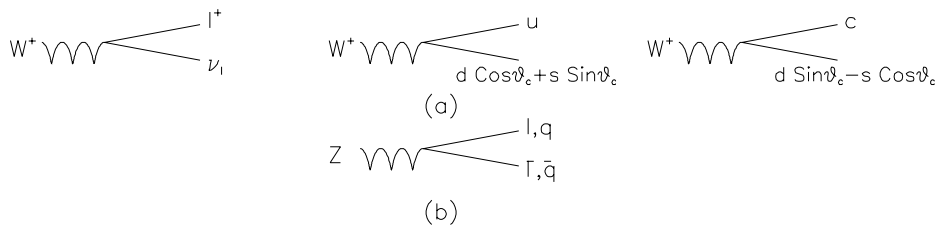

Figure 1.1: Charged current (a) and neutral current (b) diagrams of weak gauge bosons.

1.1.3 Strong Interactions

In the standard model, the strong interaction is described by quantum chromodynamics (QCD) which is an SU(3) gauge theory. There are eight gauge bosons (corresponding to eight generators of the SU(3) group) called gluons which mediate the strong force. All particles subject to strong interactions carry a quantum number known as color, which has three charges. Observable physical particles are always color singlets. Due to its non-abelian nature, the strength of the strong coupling reduces at higher energies. Therefore, at higher energies perturbative QCD calculations can be done. However, at lower energies strong coupling is large and non-perturbative techniques must be used. This makes calculations and predictions involving low energy strong interactions rather difficult.

1.1.4 Weak Decays of Charmd Mesons

Charm quarks (and hence charmed particles containing valence c quarks) decay under the weak interaction into s or d quarks. The W boson produced may decay lepton-

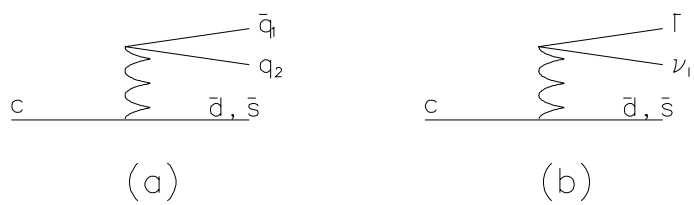

Figure 1.2: (a) hadronic and (b)semileptonic decay of the c quark

ically [to a (l, ν_l) pair] or hadronically [to a$(q_1, \overline{q_2})$ pair], as shown in the Figure 1.2. The quarks produced in the weak decay combine to from color singlet hadrons. Therefore, although the weak interaction is responsible for the decay of charmed particles, strong interactions play an important role in the hadronization process which determines the final state.

According to the way decay quarks combine in the hadronization, there can be six charm decay mechanisms, as shown in the Figure 1.4. The dominant D decays are believed to occur via spectator decays where the other (light) 'spectator' quark of the D meson does not play a direct role in the weak interaction.

W-exchange and annihilation require the overlap of the wave functions of two quarks of the parent meson. These process are also expected to be helicity-suppressed (although this suppression may be reduced by emission of soft gluons at the decay vertex) making such decays less prominent than spectator decays [2] . Evidence for exchange or annihilation type of decays are still not convincing. Although a strong candidate for W- exchange decay, $D^0 \rightarrow \overline{K^0}\phi$, has been observed, there have been arguments [6] that this could be a result of spectator decay undergoing final state scattering as shown in the Figure 1.3.

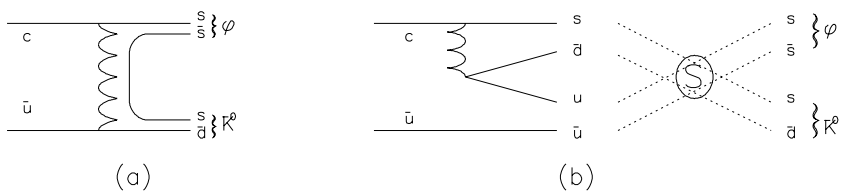

Figure 1.3: Possible decay mechanisms of $D^0 \to \overline{K^0}\phi$ (a) W -exchange (b) spectator decay with final state rescattering

Due to the large number of possible decay mechanisms and the intrinsically complicated nature of the strong interactions which govern the hadronization process, an extensive study of many decay channels is needed for a better understanding of charm decays.

1.2 BSW Model of Charm Decays

A phenomenological model for two body spectator decays of heavy (c and b) mesons which includes 1-gluon perturbative QCD corrections has been introduced by Bauer, Stech and Wirbel (BSW) [7].

The lowest order Hamiltonian of a spectator decay without QCD effects is

$$H^0 = \frac{G_F}{\sqrt{2}}(\overline{q_1}c)(\overline{q_3}q_2) \tag{1.4}$$

where

$$\overline{q_i}q_j = \overline{q_i}\gamma^\mu(1-\gamma^5)q_jV_{q_iq_j} \tag{1.5}$$

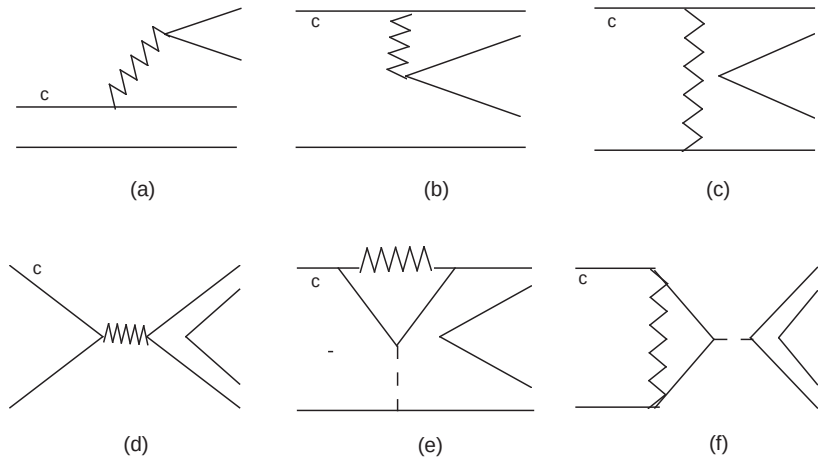

Figure 1.4: D decay mechanisms (a) outer spectator (b) inner spectator (c) W exchange (d) Annihilation (e) vertical penguin (f) horizontal penguin

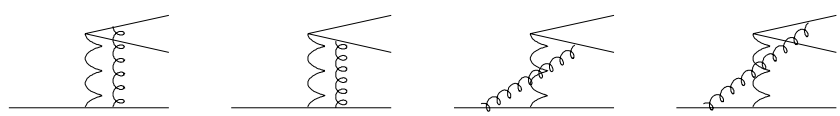

Figure 1.5: One-loop gluon corrections

As shown in the Figure 1.5, there are several contributions from first order gluon interactions to a such process. Also, there are several gluon corrections that are absorbed into the renormalization of the physical masses and couplings. The first order correction is given by [8]

$$H^1 = \frac{G_F}{\sqrt{2}} \frac{3\alpha_s}{8\pi} \ln(\frac{M_W^2}{\mu^2}(\overline{q_1}\lambda^a c)(\overline{q_3}\lambda^a q_2). \tag{1.6}$$

Here λ^a are the generators of SU(3), α_s is the strong coupling strength and μ is the energy scale involved. Using the Fierz identity [9] and color algebra relations of $SU(3)$ above equation can be simplified to [8]

$$(\overline{q_1}\lambda^a c)(\overline{q_3}\lambda^a q_2) = -\frac{2}{3}(\overline{q_1}c)(\overline{q_3}q_2) + 2(\overline{q_1}q_2)(\overline{q_3}c) \tag{1.7}$$

.

Therefore, the gluon exchanges not only modify the strength of the charged current, they induce an effective neutral current.

The Hamiltonian $H = H^0 + H^1$ is often written in terms of symmetric and anti-symmetric parts:

$$H = \frac{G_F}{\sqrt{2}}(c_+ O_+ + c_- O_-) \tag{1.8}$$

where

$$c_+ = 1 + \frac{\alpha_s}{2\pi} ln(\frac{M_W^2}{\mu^2}) \tag{1.9}$$

$$c_- = 1 - \frac{\alpha_s}{2\pi} ln(\frac{M_W^2}{\mu^2}) \tag{1.10}$$

and

$$O_{\pm} = \frac{1}{2}(\overline{q_1}c)(\overline{q_3}q_2) \pm \frac{1}{2}(\overline{s}d)(\overline{u}c). \tag{1.11}$$

After rearranging this further,

$$H = \frac{G_F}{\sqrt{2}}(c_1(\overline{s}c)(\overline{u}d) + c_2(\overline{s}d)(\overline{u}c)) \tag{1.12}$$

with

$$c_1 = c_+ + c_-$$

$$c_2 = c_+ - c_-. \tag{1.13}$$

The Bauer-Stech-Wirbel model [7] further simplifies the above formalism by assuming that the transition amplitudes factorize into a pair of matrix elements. This involves taking only the asymptotic part of the one current of the current product . Then, BSW have further shown that the weak amplitude factorizes and is fully determined by the hadronic matrix element of the other current. With this replacement of interacting fields by asymptotic fields, one neglects any final state interactions of the particles. With these correction terms, the effective Hamiltonian can be written as

$$H = a_1(\overline{s}c)(\overline{u}d) + a_2(\overline{s}d)(\overline{u}c) \tag{1.14}$$

with

$$a_1 = c_1 + \zeta c_2 \tag{1.15}$$

and

$$a_2 = c_2 + \zeta c_1 \tag{1.16}$$

Decay	Type	Widths in $10^{10}s^{-1}$
$D^0 \to K^-\pi^+$	class I	$9.92a_1^2$
$D^0 \to K^{*-}K^{*+}$	class I	$1.45a_1^2$
$D^0 \to \phi\rho$	class II	$0.82a_2^2$
$D^0 \to \phi\eta$	class II	$0.11a_2^2$
$D^0 \to \phi\omega$	class II	$0.74a_2^2$

Table 1.3: A few BSW predictions for spectator decays of D^0 [7]

where $\zeta = \frac{1}{3} = \frac{1}{N_{color}}$, which is called the color mismatch factor. It represents the fact that the quarks recombine as in Figure 1.4(b) without going through the QCD induced term in 1.13 [8].

The BSW factorization ansatz for a D decay into two particles A and B in the final state is

$$< AB|J_\mu J^\mu|D >=< A,B|J_\mu|0 >< A,B|J^\mu|D > \tag{1.17}$$

where

$$J_\mu J^\mu = (\overline{q_1}c)(\overline{q_3}q_2) \text{ or } (\overline{q_1}q_2)(\overline{q_3}c)$$

Predictions about the two body spectator decays of charm mesons have been made using this model. There can be three types of decays: Class I decays of the form $D^0 \to F_1^+F_2^-$ resulting from the charged current term, Class II decays of the form $D^0 \to F_1^0F_2^0$ resulting from the neutral current term, and Class III decays which have contributions from both terms. Table 1.3 shows a few BSW predictions for class I and class II decays. Fitting their model to $D \to K\pi$ decays, Bauer, Stech, and Wirbel estimated the values for a_1 and a_2 to be 1.3 ± 0.1 and -0.55 ± 0.1.

In an alternate approach, Bedaque, Das, and Mathur [14] used a pole dominant SU(4) flavor symmetric model to estimate QCD corrections. Their estimates (also

Decay	Branching ratio
$D^0 \to \overline{K^{*0}}\rho$	8.5×10^{-3}
$D^0 \to \overline{K^{*0}}\omega$	7.9×10^{-3}
$D^0 \to \phi\rho$	2.2×10^{-5}
$D^0 \to \overline{K^{*0}}K^{*0}$	2.6×10^{-4}

Table 1.4: BDM predictions for a few $D \to VV$ type decays [14]

based on fits to $D \to K\pi$ data) of a_1 and a_2 are

$$a_1 = 1.79 \ , \ a_2 = -0.67$$

Table 1.4 shows some of their estimates of branching ratios.

1.3 The Decay $D^0 \to K^+K^-\pi^+\pi^-$

This is the Cabibbo suppressed decay which will be studied in this thesis. In addition to the four body non-resonant mode, there can be a large number of modes that occur via intermediate resonances. Table 1.5 lists some of the possible modes.

Figure 1.6 shows the Feynman diagrams of some of the above modes. One obvious feature of those decays is that for some of the modes there are two decay amplitudes (Figure 1.6a,b, and c) which differ in the sign of the $\sin\theta_c$ term which cancel each other (in the same way the GIM mechanism cancels neutral currents). Therefore such modes can occur only through final state scattering effects. The mode $D^0 \to K^{*0}(892)\overline{K^{*0}(892)}$ is particularly interesting because it can happen only through exchange diagrams which are further helicity suppressed [2]. So any significant decay rate (*i.e.* comparable to $D^0 \to \rho\phi$ which does not have such suppressions but still has the same initial and final states) can only be caused by final state strong scattering effects.

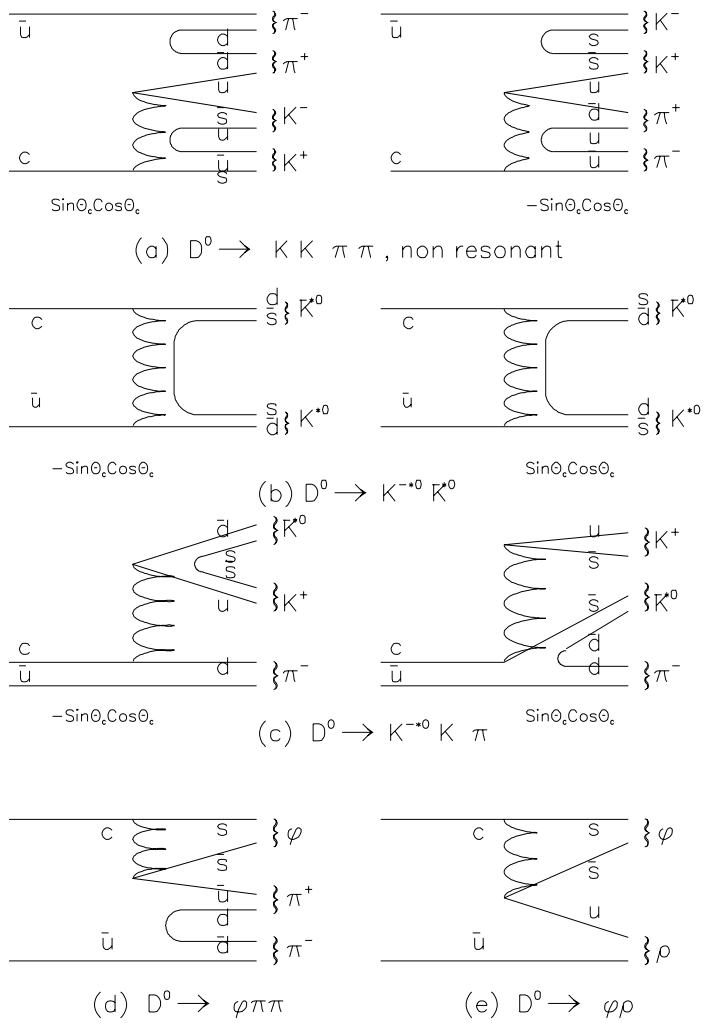

Figure 1.6: Feynman diagrams for a few resonant modes which might contribute to $D^0 \to K^+K^-\pi^+\pi^-$. Modes (a), (b), and (c) have two equal weak decay amplitudes but differ in sign resulting in a suppression in that modes.

decay mode of D^0	Decay modes of resonance
non resonant	
$K^{*0}(892)\overline{K^{*0}(892)}$	$K^{*0}(892) \to K^+\pi^-$
$K^{*0}(892)K^-\pi^+$	$K^{*0}(892) \to K^+\pi^-$
$\overline{K^{*0}(892)}K^+\pi^-$	$\overline{K^{*0}(892)} \to K^-\pi^+$
$\rho\phi$	$\rho \to \pi^+\pi^-, \phi \to K^+K^-$
ρK^+K^-	$\rho \to \pi^+\pi^-$
$\phi\pi^+\pi^-$	$\phi \to K^+K^-$
$K_1^-(1270)K^+$	$K_1^-(1270) \to K^-\pi^+\pi^-$
	$K_1^-(1270) \to \overline{K^{*0}(892)}\pi^-, \overline{K^{*0}(892)} \to K^-\pi^+$
$K_1^+(1270)K^-$	$K_1^+(1270) \to K^+\pi^+\pi^-$
	$K_1^+(1270) \to K^{*0}(892)\pi^+, K^{*0}(892) \to K^+\pi^-$
$K_1^-(1400)K^+$	$K_1^-(1400) \to \overline{K^{*0}(892)}\pi^-, \overline{K^{*0}(892)} \to K^-\pi^+$
$K_1^+(1400)K^-$	$K_1^+(1400) \to K^{*0}(892)\pi^+, K^{*0}(892) \to K^+\pi^-$
$K^{*-}(1430)K^+$	$K^{*-}(1430) \to \overline{K^{*0}(892)}\pi^-, \overline{K^{*0}(892)} \to K^-\pi^+$
$K^{+*}(1430)K^-$	$K^{*+}(1430) \to K^{*0}(892)\pi^-, K^{*0}(892) \to K^+\pi^-$
$K_2^{*-}(1410)K^+$	$K_2^{*-}(1410) \to \overline{K^{*0}(892)}\pi^-, \overline{K^{*0}(892)} \to K^-\pi^+$
$K_2^{*-}(1410)K^-$	$K_2^{*+}(1410) \to K^{*0}(892)\pi^-, K^{*0}(892) \to K^+\pi^-$

Table 1.5: Some possible Decay Modes of $D^0 \to K^+K^-\pi^+\pi^-$

1.3.1 Previous Measurements of $D^0 \to K^+K^-\pi^+\pi^-$

CLEO [10] ARGUS [11] and Fermilab E691 [12] and E687 [13] experiments have measured the branching ratio of $D^0 \to K^+K^-\pi^+\pi^-$. As shown in Table 1.6, some of them have also done incoherent resonance substructure measurements by doing fits to one dimensional invariant mass distributions of resonances. Although all experiments are consistent on the inclusive branching ratio, their values for resonant substructure are not in agreement with each other. E691 has observed most of the signal in the $K^{*0}\overline{K}^{*0}$ mode; this has not been confirmed by other experiments. ARGUS had distinguished $D^0 \to K^{*0}K^-\pi^+$ from $D^0 \to \overline{K^{*0}}K^-\pi^+$ and has observed contributions from both modes which exceed values from E691 and E687.

decay mode (f)	$\frac{BR(D^0 \to f)}{BR(D^0 \to K^-\pi^+\pi^-\pi^+)}$			
	E691 (1991)	CLEO (1991)	ARGUS(1994)	E687(1995)
inclusive	$0.028^{+0.008}_{-0.007}$	0.0314 ± 0.01	$0.041 \pm 0.007 \pm 0.005$	$0.034 \pm 0.04 \pm 0.04$
non-resonant	$0.01^{0.011}_{-0.001}$			< 0.011 (90% C.L.
$D^0 \to K^{*0}\overline{K}^{*0}$	$0.036^{+0.02}_{-0.016}$	< 0.033 (90% C.L.)		0.016 ± 0.006
$D^0 \to K^{*0}K^+\pi^-$	$0.01^{+0.016}_{-0.01}$		$0.043 \pm 0.014 \pm 0.009$ $0.023 \pm 0.013 \pm 0.009$	< 0.017 (90% C.L.)
$D^0 \to \phi\pi^+\pi^-$	$0.0076^{+0.0066}_{-0.0049}$			0.006 (90% C.L.)
$\phi\rho$		0.024 ± 0.006	$0.02 \pm 0.006 \pm 0.005$	0.005 ± 0.003
$K^+K^-\rho$				0.005 ± 0.003

Table 1.6: Previous measurements of $D^0 \to K^+K^-\pi^+\pi^-$ and resonant substrucrure.

1.3.2 Summary

Physical processes involved in the decay of charmed mesons have not yet been clearly understood. Experimental measurements on different charmed decays provide useful information which improve the understanding of heavy quark systems.

Previous studies have shown that final states of many three and four-body decays of charmed particles are dominated by intermediate two-body decay modes. In this thesis I report the measurement of the branching ratio and the resonant substructure of the Cabibbo suppressed decay $D^0 \to K^+K^-\pi^+\pi^-$ using data from Fermilab experiment E791. Although this decay has been studied by several other experiments, they have used incoherent tecniques which fit one dimensional invariant mass distributions to measure the resonant substructure. This does not allow possible interferences among different decay amplitudes and is not a correct quantum mechanical description of the decay. I will be using a maximum likelihood technique which adds all

Decay mode	Author	Branching ratio %
$\phi\rho$	Bauer, Stech, and Wirbel [7]	0.1
	Bedaque, Das and Mathur [14]	0.022
	Kamal,Verma and Singh [15]	0.026-0.08
$K^{*0}\overline{K}^{*0}$	Bedaque, Das and Mathur	0.0026

Table 1.7: Theoretical predictions of few decay modes contributing to $D^0 \rightarrow K^+K^-\pi^+\pi^-$

decays coherently and allows interference among them, thus describing the system correctly. There are a few theoretical predictions for some decay modes (Table 1.7) contributing to $D^0 \rightarrow K^+K^-\pi^+\pi^-$. Those predictions will be compared with the E791 results.

Chapter 2

Experimental Setup

Fermilab experiment E791, an open geometry fixed target hadroproduction experiment, was the fourth open charm experiment done at the Fermilab Tagged Photon Lab (Table 2.1).

The spectrometer, designed to study the photoproduction of charm (hence known as the Tagged Photon Spectrometer), was commissioned in 1979 for experiment E516. It was followed by experiment E691, which used nine planes of silicon microstrip detectors for precision tracking in the vertex region. This enabled E691 to identify charmed particle decays by separating their primary and secondary vertices. E769 followed E691. It used hadron beams containing π^+, π^-, K^+, K^- and protons instead of a photon beam, to study hadroproduction of charm. Finally, E791 further improved the detector, built a fast data acquisition system and collected a 20 billion event sample using a π^- beam during the 1991 fixed target run (from July 1991 to January 1992).

experiment	year	beam	number of reconstructed charm
E516	1979	photon	150
E691	1985	photon	10,000
E769	1988	$\pi^+, \pi^-, K^+, K^-, p$	4,000
E791	1992	π^-	200,000

Table 2.1: Charm experiments at the Tagged Photon Lab

2.1 The Detector

The TPL spectrometer (Figure 2.1) was located in the P-East fixed target experimental area at Fermilab. It had a number of detector elements to measure various properties of particles and their trajectories as they traversed the spectrometer. The major components of the spectrometer were the beam tracking system, the target, the interaction trigger,the downstream silicon microstrip detectors (SMDs), the drift chambers (DCs) and proportional wire chambers (PWCs), the analysis magnets, the threshold Cherenkov counters, the electromagnetic calorimeter, the hadronic calorimeter, muon walls and the data acquisition and monitoring system.

2.1.1 Beam Line and Beam Tracking System

The π^- beam for the experiment was produced by bombarding 800 GeV/c protons from the Tevatron on a 30 cm thick beryllium target upstream of the spectrometer. About about 2×10^{12} protons per spill were allocated to TPL. The typical yield of secondary pions from the primary target was about 40 million per spill (at the target).

Eight PWCs and six SMDs were used to measure the transverse positions of the beam particles. This information was used to reconstruct the beam particle trajectory, which was used in reconstructing the primary vertex and subsequent analysis. Table 2.2 shows the characteristics of beam tracking SMD and PWC planes. PWC and

	PWC Assembly 1	PWC Assembly2	SMD Assembly 1	SMD Assembly 2
number of planes	4	4	3	3
number of instrumented wires/strips	64	64	384,384,448	448,416,416
view ordering	X ,Y,X', W	X,Y,X', W	Y,X, W'	W',Y,X
wire/strip spacing	1.0 mm	1.0 mm	25/50 *μm	25/50 μm*
Location in z	-3117 to -3114	-1212 to -1209	-80.25 to -74.52	-33.16 to -29.48

Table 2.2: The beam tracking SMD and the PWC parameters.(* strips were grouped in pairs and read together)

foil number	1	2	3	4	5
material	platinum	carbon	carbon	carbon	carbon
z position (cm)	-8.191	-6.690	-5.154	-3.594	-2.060
thickness (mm)	0.52	1.57	1.57	1.53	1.58
proton interaction length (%)	0.584	0.589	0.586	0.582	0.582
diameter(cm)	1.61	1.37	1.38	1.37	1.36
radiation length (%)	16.9	1.2	1.2	1.2	1.2

Table 2.3: E791 Target parameters

SMD planes were in two groups.

2.1.2 The Target

The E791 target consisted of five circular target foils, one platinum and four carbon (industrial diamond) (Table 2.1.2), spaced about 1.5 cm from each other as shown in Figure 3.1. This configuration meant that most of the particles decayed outside the target foils, thus reducing backgrounds due to secondary interactions while maintaining a significant interaction length. The overall thickness of the target foils was about 2% of a pion interaction length.

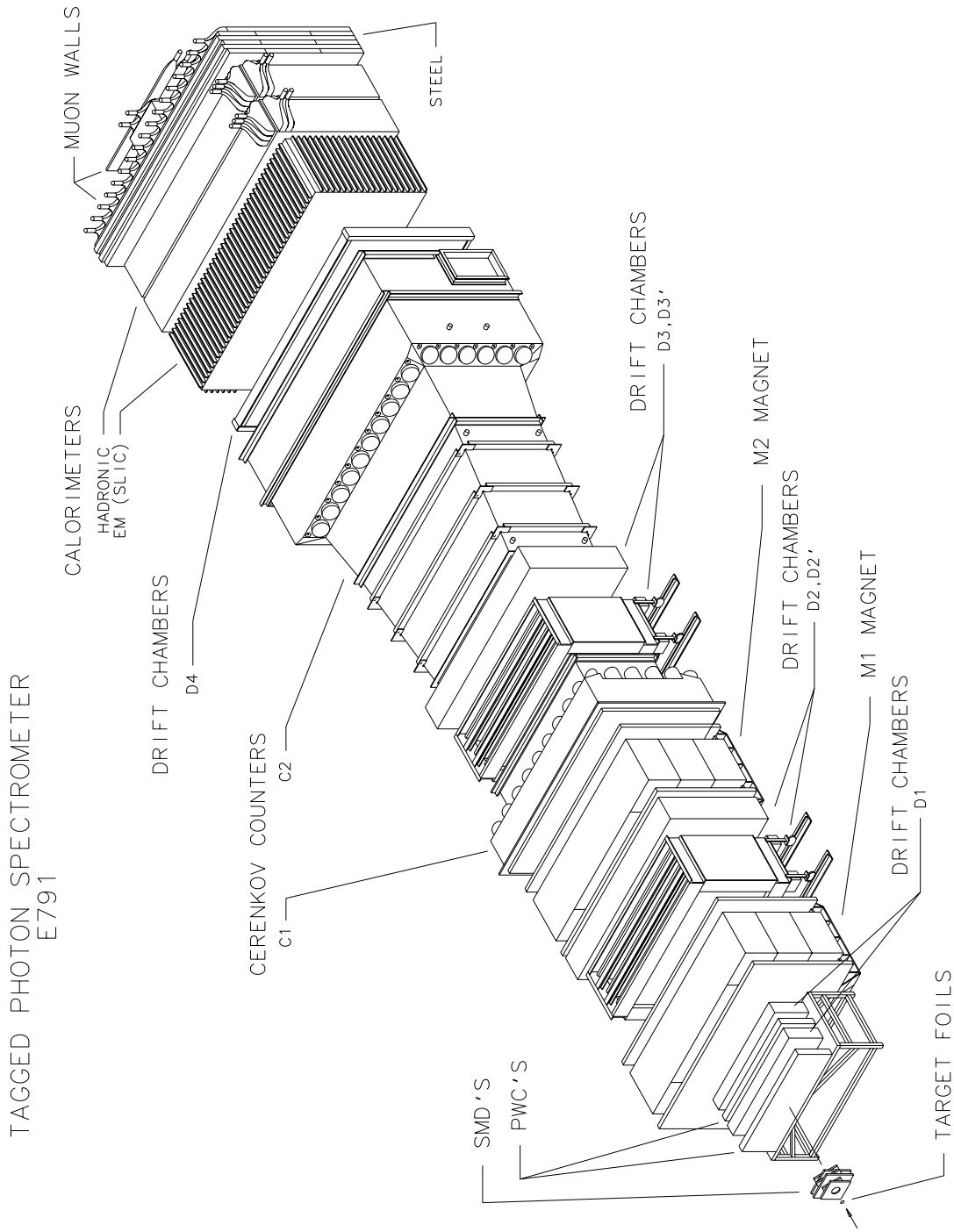

Figure 2.1: E791 Spectrometer

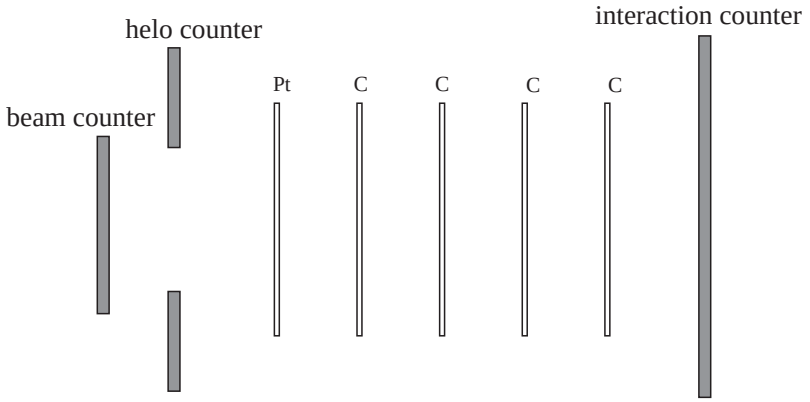

Figure 2.2: E791 Target and pretrigger counter region (not to scale)

2.1.3 Interaction Trigger Counters

There were three scintillator counters in the target region. The beam counter detected incident particles (beam counter), the veto counter vetoed particles outside the target region and the interaction counter indidated whether an interaction had occurred. The interaction counter threshold was set at four minimum ionizing particles. Figure 3.1 shows the layout of the target and interaction counters.

2.1.4 Silicon Microstrip Detectors (SMDs)

The SMDs consist of arrays of reversed biased p-n junction strips arranged in planes. When a charged particle passes through a strip, it generates electron-hole pairs which produce a signal in that channel which were read by a latch bit readout after being amplified and discriminated.

The downstream SMD system consisted of 17 silicon planes. Each SMD plane was 300 μm thick. The overall geometrical acceptance of the system was about ± 100 mrad around the beam axis. Since there were multiple hits in a plane for an event, information from three SMD views was required to determine the the intercept of

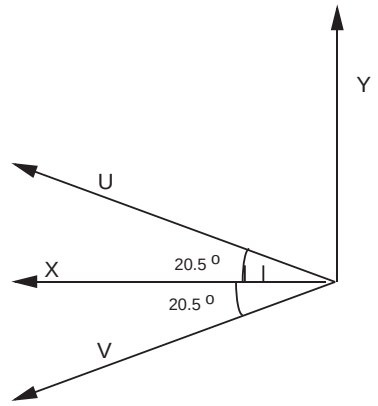

Figure 2.3: Different view directions defined in E791. The z axis points into the paper. (The measurment direction shown is orthognal to the corresponding strip direction.)

a charged particle track with the SMDs. Therefore, SMD planes were assembled in groups of three with SMD's measuring in X, Y and V views. (Figure 2.3).

The main characteristics of the SMD planes are summarized in Table 2.4.

2.1.5 Drift Chambers

Thirty five drift chambers arranged in four groups (D1 ,D2, D3 and D4) were the main elements of the track detection system downstream of SMDs. In each assembly drift chambers were arranged in different views X ,X' ,U,V (X' and X drift chambers both had wires running vertically but X' were offset by half a cell relative to X to improve the resolution in x). The first assembly, D1, was located upstream of the first analysis magnet M1 and, along with the SMD's and PWCs, provided an initial measurement of the track trajectory. D2 was positioned between the two analysis magnets. The third drift chamber group, D3, was located just after the second analysis magnet, M2, and added tracking information for particles with momentum high enough to make it through both magnets. The last chamber, D4, came much further downstream, past

plane	z-position (cm)	strip spacing (μm)	number of strips	view
7	0.670	25;50 *	688	Y
8	1.000	25;50 *	688	X
9	1.931	50 *	512	X
10	3.015	50	512	Y
11	6.684	50	512	V
12	11.046	50	884	Y
13	11.342	50	884	X
14	14.956	50	884	V
15	19.915	50	1000	X
16	20.254	50	1000	Y
17	23.878	50	1000	V
18	27.558	50; 200 *	864	V
19	31.848	50; 200 *	864	X
20	34.548	50; 200 *	864	Y
21	37.248	50; 200 *	864	X
22	39.948	50; 200 *	864	Y
23	45.508	50; 200 *	864	V

Table 2.4: main characteristics of down stream SMD system (* in these planes the outer strips were read out together, thus increasing the effective width of these strips)

DC group	D1	D2	D3	D4
dimensions (cm)	160 × 120	230 × 200	330× 200	550× 300
view ordering	X,X',U,V	X,U,V	X,U,V	X,U,V
number of planes	8	12	12	3
number of channels	1536	2400	1952	416
U and V cell size (cm)	0.446	.892	1.487	2.97
X cell size (cm)	0.476	0.953	1.588	3.18
z-position first plane (cm)	142.49	381.43	928.14	1737.99
z-position last plane (cm)	183.66	500.80	1047.10	1749.42

Table 2.5: Drift Chamber Characteristics

the Cherenkov counters, just before the calorimeters. Its poorer resolution was caused by its intrinsic design (its basic X cell being twice as large as for D3) and higher noise level due to backscattering from the calorimeter. Typical resolutions and efficiencies per chamber are shown in the Table 2.5

As in the case of the SMDs hits in the three different view planes were required to determine the position of a track. Left-right ambiguity of DC hits made this more complicated.

2.1.6 Proportional Wire Chambers

There were two PWC planes downstream from the target (120.4 and 162.9 cm in z) They measured the y coordinate of the tracks and had a wire spacing of 2.0 mm. Like beam PWCs, they used a gas mixture of 82.7% Ar, 17% CO_2, and 0.3% freon.

2.1.7 Analysis Magnets

Two large-aperture copper coil magnets were used in the E791 spectrometer. They provided transverse momentum kicks of 212 MeV/c and 320 MeV/c. The magnetic field of these magnets was measured using the zip track [17].

	M1	M2
z-position front (cm)	222.5	566.9
z-position center (cm)	273.5	617.7
z-position back (cm)	324.1	668.5
aperture (cm^2)	183.2 $\times$ 81	182.9 $\times$ 85.6
length (cm)	101.6	101.6
current (amp)	2500	1800
$\int B_y(0,0,z)dz$ (gauss-cm)	711,097	1,077,242
p_T kick (MeV/c)	212	320

Table 2.6: Analysis Magnet Characteristics

	C1	C2
length (m)	3.7	6.6
number of mirrors	28	32
gas mixture	100% N_2	80% He -20% N_2
$\delta = (n-1)$	290 $\times 10^{-6}$	86 $\times 10^{-6}$
pion momentum threshold (GeV/c)	5.8	10.6
kaon momentum threshold (GeV/c)	20.5	37.6
proton momentum threshold (GeV/c)	38.9	71.5

Table 2.7: Characteristics of the Cherenkov counters

2.1.8 Cherenkov Counters

Two gas Cherenkov threshold counters [16] were part of the E791 particle identification system. The first counter, C1, was positioned partially inside of M1 and the second counter, C2 after M2. The two counters had different thresholds (Table2.7) This allowed the identification of particles in a broad momentum range (6- 60 GeV) (figure 2.4).

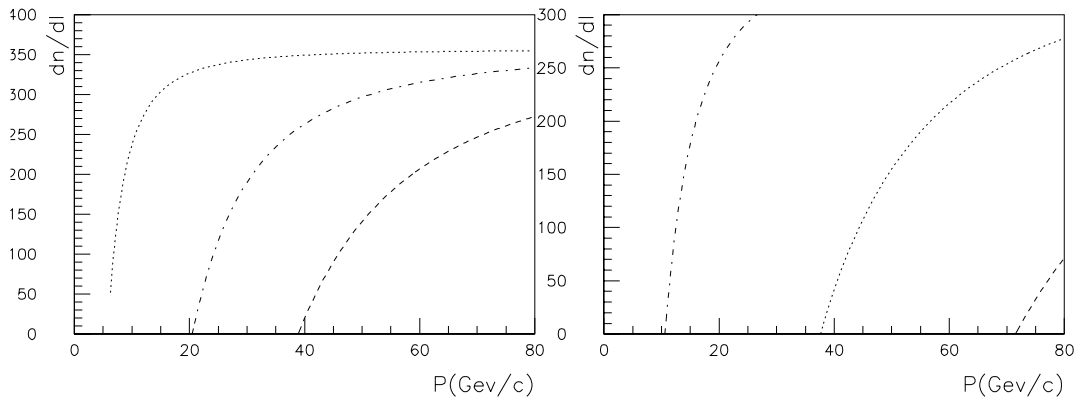

Figure 2.4: Expected number of photo electrons produced in Cherenkov counters for π, K^+ and protons assuming refractive index and detector are uniform with wave length

2.1.9 Calorimetry

There were two calorimeters in the E791 spectrometer. The segmented liquid ionization calorimeter (SLIC) [19]and the hadrometer [18]. Both were used as part of the trigger, selecting events with large energy deposition transverse to the beam line (E_T trigger). Used in conjunction with the Cherenkov counters, tracking detectors and the muon wall, the calorimeters were part of the particle identification system (electrons, photons, muons and hadrons have very different energy deposition patterns in the calorimeters).

The SLIC was an electromagnetic calorimeter. It was composed of sixty layers of channels filled with a liquid sintillator, separated by lead sheets. Twenty layers were devoted to each view and channels alternate in the order of U,V,Y (Table 2.8).

The hadrometer was located just behind the SLIC. It was designed to detect both

	u channels	v channels	y channels
number of channels	109	109	116
orientation from vertical	$-20.5°$	$+20.5°$	$90°$
number of layers	20	20	20
single channel width (cm)	3.17/6.35	3.17/6.35	3.17/6.35
channel length (cm)	260	260	244
view ordering	U, V, Y		
upstream z-position (cm)	1866.		
downstream z-position (cm)	1962.		
active area (cm^2)	$488 \times 244.$		
total radiation length	21.5		
total interaction length	2.07		
energy resolution	$(\frac{\delta E}{E})^2 \approx \frac{(17.4\%}{E)^2} + (11.5\%)^2$		
position resolution (cm)	0.65		

Table 2.8: Main parameters of the SLIC.

hadrons and muons. To maximize nuclear interactions with hadrons, the hadrometer was made of 36 one inch thick layers of steel radiator interleaved with 3/8 inch thick plastic scintillator (Table 2.9). The hadrometer was divided into front and back modules. Each module was three interaction lengths thick. The scintillator layers were broken into 14.5 cm strips alternating in the X and Y directions. The X counters spanned the full height of the detector whereas the Y counters were divided at the vertical midplane. A comparison between the energy deposited in the front and back modules provided some information used to separate muons and hadrons.

2.1.10 The Muon Wall

Muons interact mainly through ionization and consequently retain most of their energy even after going through both calorimeters. E791 had two muon walls made of plastic scintillator paddles placed at the end of the spectrometer to detect these muons. There was a 106 cm-thick steel shield wall meant to block hadrons that had

	X channels	Y channels
number of channels	66	76
number of layers	36	36
single channel width (cm)	14.5	14.5
view ordering	X, Y	
absorber thickness (cm)	2.54	
total interaction length	6	
upstream z-position (cm)	1973.	
downstream z-position (cm)	2131.	
active area (cm^2)	490. $\times$ 270	
energy resolution	$\frac{\Delta E}{E} \approx \frac{75\%}{\sqrt{E}}$	

Table 2.9: characteristics of the hadron calorimeter.

not interacted in the calorimeters. Only muons above 4 GeV and a few punch-through hadrons were seen in the muon walls. The X-wall, which is 3 m in height, consisted of 12 vertical paddles each 40.6 cm wide with center paddles 61 cm wide. The center paddle consisted of three parts. The middle paddle was 60 cm in height and two paddles above and below it were 120 cm in height. The second wall, the Y-wall, had 16 paddles, each 14 cm wide and 3 m in length.

2.2 Trigger and Data Acquisition System

2.2.1 The Trigger

The E791 trigger was a two-level decision making process. A pretrigger detected a beam particle and the occurrence of an interaction. The pretrigger decision was made in about 160 ns allowing for an early digitizing start. The calorimeter-based trigger decision took about 470 ns.

The calorimetric trigger was based on the fact that the decay products of relatively massive charm quarks are produced with more transverse momentum than light quark decay products. To take advantage of this, the E791 trigger was designed to select events in which the amount of energy deposited transverse to the beamline is at least 4.2 GeV. Tranverse energy (E_T) was estimated by summing the energy deposited in all the channels of the SLIC and the hadrometer weighted by $\sin\theta$. Here θ is the angle between the beam direction and the line joining the target and the calorimeter element. The calorimeters made this measurement in about 470 ns. In addition, events with more than 700 GeV of total energy were rejected. This got rid of events in which multiple beam particles interacted. Most of the events recorded by E791 satisfied both trigger requirements. However, there were special data runs (called interaction runs) which recorded data with only the pretrigger requirements. About 10% of the data was interaction data.

2.2.2 Data Acquisition System

Beam particles interacted in the targets every 25 μs on average. Approximately half of these interactions passed the trigger requirements. Therefore, there was about 50 μs between triggered interactions. Digitization took about 50 μs. Therefore, there was about 50% deadtime.

Digitized event segments were compressed to a, typical length of 2.5 kbytes, formatted and writen to 8 mm tapes using 42 exabyte tape drives and 54 ACP 1 processors. A 640 Mbytes memoery buffer allowed writing of data during the interspill. The DAQ collected and recorded data at a rate of 207k events per spill averaging 9.6 Mb/s [20].

Chapter 3

Event Reconstruction and Selection

The raw data sample collected by E791 during the 1991 fixed target run was about 20 billion events 0n 24 000 8 mm 2.2 GB tapes. This raw data sample had to be reconstructed and reduced to a manageable level before any physics analysis could be done. Data reduction was done in several stages: reconstructing and filtering, stripping, substripping and microstripping. Each stage reduced the data sample to smaller subsets (Figure 3.2). This required a formidable amount of computing power.

Reconstruction and filtering was a general process for all analysis and needed a huge amount of computing power. It was done on four computer farms [24](Table 3.1) and took about 10,000 MIPS years. Stripping and substripping were more focused on selecting events for different physics analysis and were I/O rather than CPU bound. They were done on single workstations.

Institution	Events Reconstructed (billions)
Centro Brasileiro de Pequisas Fisicas	1.8
Fermilab	4.7
Ohio/Kansas State University	6.2
University of Mississippi	6.4

Table 3.1: Number of events reconstructed for E791 at different computer farms.

3.1 Event Reconstruction and Filtering

Reconstruction of an event from raw data included reconstructing the tracks, finding primary and secondary vertices, calorimetry and Cherenkov reconstruction and muon identification. Events were first partially reconstructed and then filtered. Events passing the filter were fully reconstructed.

3.1.1 Track Reconstruction.

Charged tracks were reconstructed from SMD and DC hit information. SMDs upstream of the target were used (with PWCs) to reconstruct the beam track and the downstream SMDs were used for the main tracking. The SMD tracking algorithm started with finding straight line segments in each view using a minimum χ^2 fit. Each X and Y view required a minimum of four hits and the V view required three hits in a line segment. Finally, one dimensional tracks from the three views were combined to form three dimensional straight line tracks.

Track segments found in the silicon tracking were extended to include drift chamber hits. Using the drift chamber hit information from three views, the possible positions of the actual hit on each drift chamber group (which were called triplets) were first reconstructed. These triplets, rather than individual DC hits were used

region 0	hits in SMDs
region 1	hits in D1
region 2	hits in D2
region 3	hits in D3,D4

Table 3.2: Assingment of regions for tracks

in tracking. Because tracks were deflected by the analysis magnets in the xz plane, their y intercept on drift chambers was used to associate silicon tracks with DC hits. First, the silicon track was extended up to the D3 and all triplets which had the same Y elevation were taken as candidates for the extended SMD track. The best possible track was found by fitting the candidate track with triplets along the track. This was repeated for all silicon tracks working from D3 upstream until all tracks with acceptable χ^2 per degree of freedom (χ^2/ν) were found. In E791 terminology, those tracks which had both SMD and DC hits were called SESTR tracks. The momenta of tracks were also calculated during the track reconstruction.

Drift Chamber hits left unused by the SESTR tracks were used to reconstruct drift chamber only tracks (called ESTR tracks). This was done by first finding the track segments in D3 (and D2) and projecting them into other drift chambers.

For characterization purposes, the E791 the detector was divided into four physical regions along the z axis (Table 3.2). Each track was assigned a track category given by,

$$\sum 2^i$$

where i takes the value of the region number the track is passing through. Thus, a charged track which originated at the target and had hits in SMDs, D1, D2, and D3 was category 15, a track which originated after the SMDs and decayed between D2

and M2 had a category 6, and so on.

About a third of category 3 tracks were found to be ghost tracks (false tracks which were formed by the tracking algorithm). Later on, an algorithm tuned by a neural net was used to discard most of the ghost tracks from the category 3 sample.

3.1.2 Vertex Reconstruction:

After reconstructing the SESTR tracks, primary and secondary vertices were found. Vertex reconstruction started with the primary vertex. Presence of the beam track and the occurrence of the primary interaction in a target foil were among the factors used to reconstruct the primary vertex. Primary vertex reconstruction started with finding the best two prong seed vertex of the beam track with a SESTR track and then proceeded adding more tracks to form a vertex with good χ^2/ν. Events which do not have a good beam track were also vertexed by starting with a two prong SESTR seed vertex inside a target foil. If a good primary vertex was found, tracks which were not used in the primary were used to find secondary vertices. Secondary vertex finding was also proceeded starting with two prong seeds and then adding more tracks. All independent secondary vertices with acceptable χ^2 were formed and some sharing of tracks among different secondary vertices was allowed.

3.1.3 Cherenkov Reconstruction

Cherenkov information was used to predict the probability that the each track was due to a particle of particular type. This was done by comparison of the light collected by each unit to the number of photoelectrons each particle type would generate at the given momentum. This required the knowledge of thresholds and efficiencies of mirror-cone-phototube units which had been measured in the calibration (Gains of the phototubes had been measured before they were installed). The overall efficiencies

were measured observing the response of each unit to very high momentum isolated tracks (which had Cherenkov light centered within a single mirror).

The probability that n photons are observed in counter i if the particle has the type j is given by

$$f_{ij} = \frac{\mu_{ij}^n e^{-\mu_{ij}}}{n!}$$

where μ_j is the predicted number of photons for the particle type j. Combining the probabilities from the two Cherenkov counters a total probability that a particle was of the type j

$$f_j = f_{1j} f_{2j}$$

The final particle identification probability P_j was calculated by normalizing this to *a priori* expected probabilities.

$$P_j = \frac{f_j}{\sum f_k A_k}$$

The *a priori* expectations A_j, were the probability of natural occurrence of each particle type j in the data . There values were taken from E516 results (Table 3.3). For the tracks which do not have Cherenkov information, the *a priori* probabilities were assigned.

3.1.4 Filtering

Filtering was done as the events were reconstructed. An event having a primary vertex would be accepted by the filter if one of the following three criteria were met:

1. presence of a secondary vertex with good separation;

particle type	a priori probability
electron	0.02
muon	0.01
pion	0.81
kaon	0.12
proton	0.04

Table 3.3: particles *a priori* probabilities used in E791

2. presence of a K_s or a Λ from ESTR vertex reconstruction;

3. presence of a ϕ from two SESTR tracks.

Table 3.4 shows the typical cuts used in the filter.

In addition to the raw data, all reconstructed physical parameters (tracks, vertices, particle identification information, *etc.*) were written on the output data summary tapes (DSTs). This enabled subsequent processing to use that information without repeating the reconstruction. The filtering reduced the data sample to about 7500 DSTs.

3.1.5 Stripping

As a further step to reduce the data set to a smaller size for physics analysis, events that were filtered and fully reconstructed were passed though the selection criterion called the stripping. Stripped data were written to two output streams (stream A and B). The analysis described in this thesis used events selected by the Stream A. In addition to the SESTR secondary vertex stripping tag (which selected the events used for this thesis analysis, Table 3.1.5), events were tagged by a multi-lepton tag, a K_s and Λ tag, a pentaquark tag and many more [21]. Stripping reduced the data set into 2000 DSTs in each stream.

Filter	requirement	cut made	events kept
SMD vertex	well separated secondary	$SDZ > 6$ for 2 prongs $SDZ > 4$ for 3 or more prongs	9%
ESTR V	presence of K_s	track χ^2/DOF < 5 $0.5 <$ track momentum < 500 DCA of two tracks $< 0.5cm$ $0.470 < M(\pi^+\pi^-) < 0.520$ GeV (region 1) $0.465 < M(\pi^+\pi^-) < 0.525$ GeV (region 2) (region 2)	9%
	presence of Λ	track χ^2/DOF < 5 $0.5 <$ track momentum < 500 DCA of two tracks $< 0.7cm$ $1.106 < M(p\pi^-) < 1.125$ GeV (region 1) $1.100 < M(p\pi^-) < 1.130$ GeV (region 2) (region 2)	
ϕ	presence of ϕ	track χ^2/DOF < 5 $0.5 <$ track momentum < 500 DCA of two tracks $< .5cm$ Joint Kaon Probability > 0.05 $1.015 < M(K^+K^-) < 1.025$	1%

Table 3.4: Typical filter selection cuts

multiplicity	SDZ	p_T *balance*	lifetime
3	> 5	< 1 *GeV*	< 5 *ps* (assuming a $D^{\pm}$)
4	> 5	< 1 *GeV*	

Table 3.5: Summary of three and four prong strip cuts.

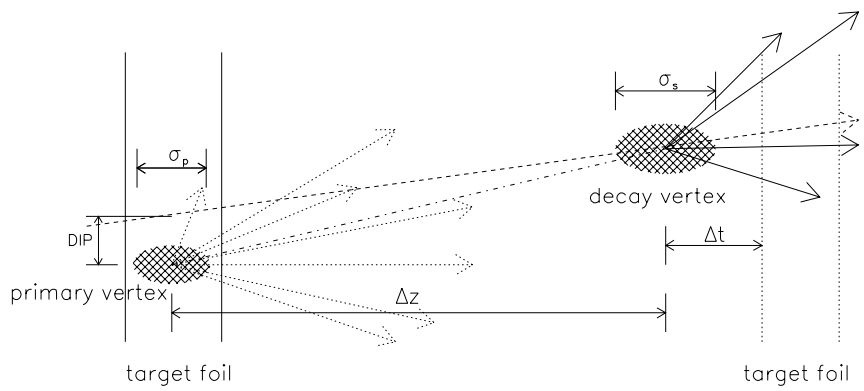

Figure 3.1: Geometry of a typical reconstructed E791 event in the target region

3.2 Substripping

The stripped data set was still too big for a physics analysis. Selection criteria had to be applied which preferentially selected the events for specific type of physics topics, thus reducing the data sample significantly. This was done at the substripping stage. Tighter cuts on various event parameters reduced the number of events which were not relevant for the analysis but kept most of the interesting events. Cuts were applied on following parameters at the substrip and subsequent stages.

SDZ: The significance of the z separation of the primary and the secondary vertices in terms of the error.

$$SDZ = \frac{\Delta Z}{\sqrt{\sigma_{pri}^2 + \sigma_{sec}^2}}$$

The relatively large lifetime of D^0 gives a physically measurable separation (order of 2-15 mm) between the production vertex and the secondary decay

vertex. Therefore, a well separated secondary vertex is a good signature for a charm signal.

DIP: The projected transverse separation of the parent (D) track from the primary vertex

In an ideal event, the reconstructed D momentum should point back to the primary vertex and should should have zero DIP. However, (due to resolution effects), it is not zero. Nevertheless, it tends to be small (a few tens of microns) for the real signal while more uniformly distributed for random backgrounds. For misidentified charm backgrounds where there are missing or incorrectly identified tracks, DIP can be high.

p_T balance: The transverse component of the parent momentum to the line of flight.

This is similar to the DIP but depends on the vertex separation differently.

SPRI: The significance of transverse separation of the decay tracks from the primary vertex (in terms of error).

Larger separation of decay tracks assures that they are not misidentified tracks from the primary vertex.

STRG: The significance of separation of the decay vertex from the nearest target foil.

$$STRG = \frac{\Delta t}{\sigma_{sec}}$$

A cut on this parameter reduced the backgrounds from secondary interaction in target foils.

z_{sec}: z position of the decay vertex.

A cut on this eliminated the backgrounds from the secondary interactions in the interaction counter and downstream SMD planes.

C(K): Cherenkov identification probability of kaons.

Kaons had an *a priori* probability of 0.125. A Cherenkov probability of being a kaon above this value gave a positive indication of the particle's being a kaon.

p: Track momentum

Since Cherenkov identification is effective only in 6-60 GeV, restricting the momentum to this range made the Cherenkov identification more effective.

Track χ^2/DOF : χ^2/DOF of the tracks from the track fitting.

Candidate $D^0 \rightarrow KK\pi\pi$ and the normalizing $D^0 \rightarrow K\pi\pi\pi$ events were selected from the stream A strip. The substripping algorithm selected candidate $D^0 \rightarrow KK\pi\pi$ and $D^0 \rightarrow K\pi\pi\pi$ events from four SESTR track combinations which from a good secondary vertex ($\chi^2 < 15$). To reduce the number of combinations that had to be checked, the vertex was required to include at least two tracks from the secondary vertices in the vertex list. This algorithm was a part of a larger event selection algorithm which substripped events for more than 20 different analyses. This substrip wrote events to three different streams, each containing events for several physics analyses and reduced the data set to 330 DST tapes in each stream. Stream C output was used for this analysis. Table 3.6 shows the cuts used in the substrip (for candidate $D^0 \rightarrow KK\pi\pi$ and $D^0 \rightarrow K\pi\pi\pi$ events).

3.2.1 Micro Stripping

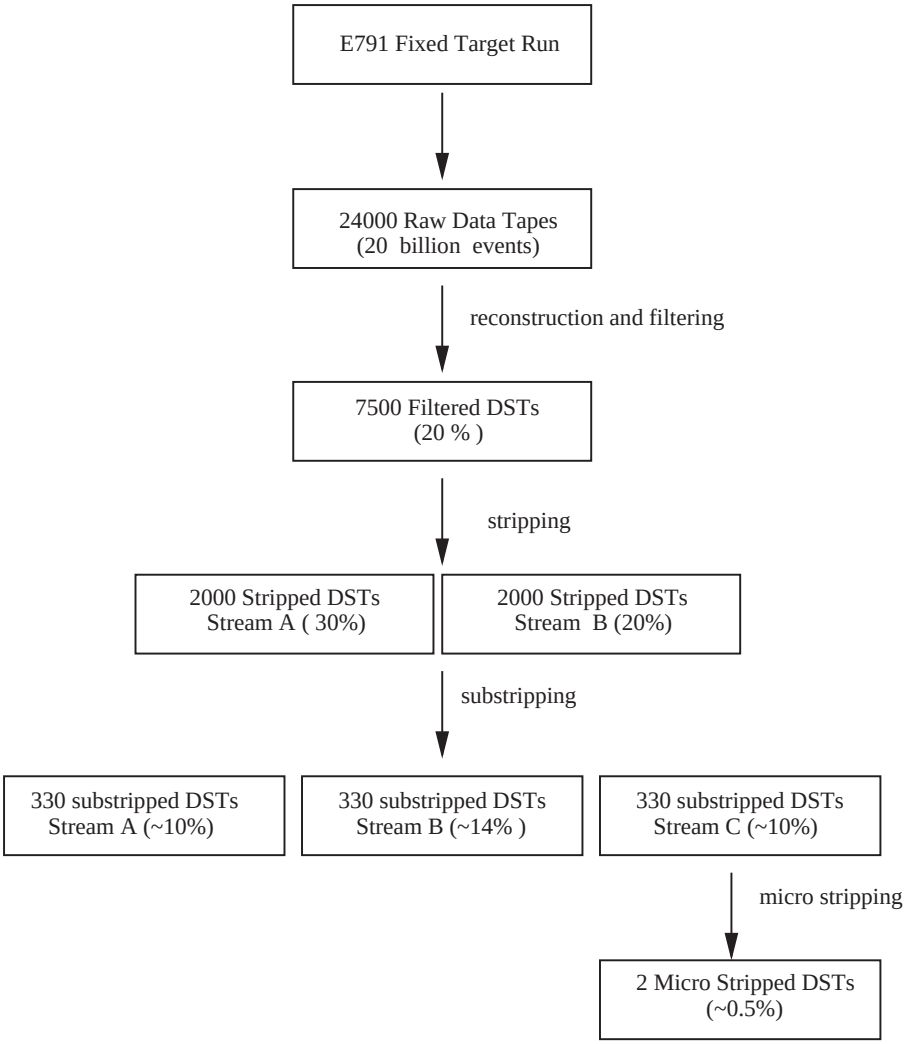

Figure 3.2: Data Selection for the $D^0 \rightarrow K^-K^+\pi^-\pi^+$ analysis. Amount of data reduction in each stage is given in parentheses

parameter	cut
SDZ	>8
DIP	<80μ m
p_T *balance*	<0.6 GeV
SPRI	$> 4\sigma$
secondary vertex χ^2	< 15
$STRG$	> 0
Track χ^2	< 6
Track momentum	$> 0.5GeV$
Track Category	≥ 3
$M(KK\pi\pi)$	$1.7 < M2.1 < GeV/c$
$M(K\pi\pi\pi)$	$1.7 < M < 2.0GeV/c$

Table 3.6: $D^0 \rightarrow KK\pi\pi$ and $D^0 \rightarrow K\pi\pi\pi$ event selection cuts used in the substrip.

Final events for the analysis were selected from substripped DSTs. A vertex driven algorithm was used to select candidate $D^0 \rightarrow KK\pi\pi$ (and $D^0 \rightarrow K\pi\pi\pi$ for normalization) events . The algorithm first looked for a four prong secondary vertex found by the E791 vertexer. If this vertex satisfied a few requirments (Table 3.7), the parent mass of the four tracks combination was calculated assuming $D^0 \rightarrow KK\pi\pi$ and $D^0 \rightarrow K\pi\pi\pi$ hypothesis. Those candidates which had parent masses 1.7 GeV/c^2 to 2.0 GeV/c^2 were kept by the micro strip.

Since the E791 vertexer was optimized to find vertices with different multiplicities, its efficiency to find four prong vertices was not optimum. Some actual four prong vertices were partially reconstructed as two or three prong vertices. Some of those partially reconstructed four prong vertices were recovered by combining remaining SESTR tracks with three prong vertices to form four prong vertices with reasonable χ^2 (< 15). Those events which were extracted from a 3 prong vertex were called SEED3 events and coming from 4 prong vertices were called SEED4 events.

The cuts listed in Table 3.7 were used in selecting events in the final substrip.

parameter	cut
SDZ	>8
DIP	<60μ m
p_T *balance*	<0.5 GeV
SPRI	$> 4\sigma$
z_{sec}	$< 0.3\ cm$
secondary vertex χ^2	< 15
$STRG$	> 0
Track χ^2	< 6
Track momentum	$> 0.5GeV$
Track Category	≥ 3
$M(KK\pi\pi)$	$1.7 < M < 2.0\ GeV/c^2$
$M(K\pi\pi\pi)$	$1.7 < M < 2.0\ GeV/c^2$

Table 3.7: Event selection cuts used in the final analysis substrip.

Figure 3.3 shows the resulting $K\pi\pi\pi$ and $KK\pi\pi$ mass distribution from events passed the substrip.

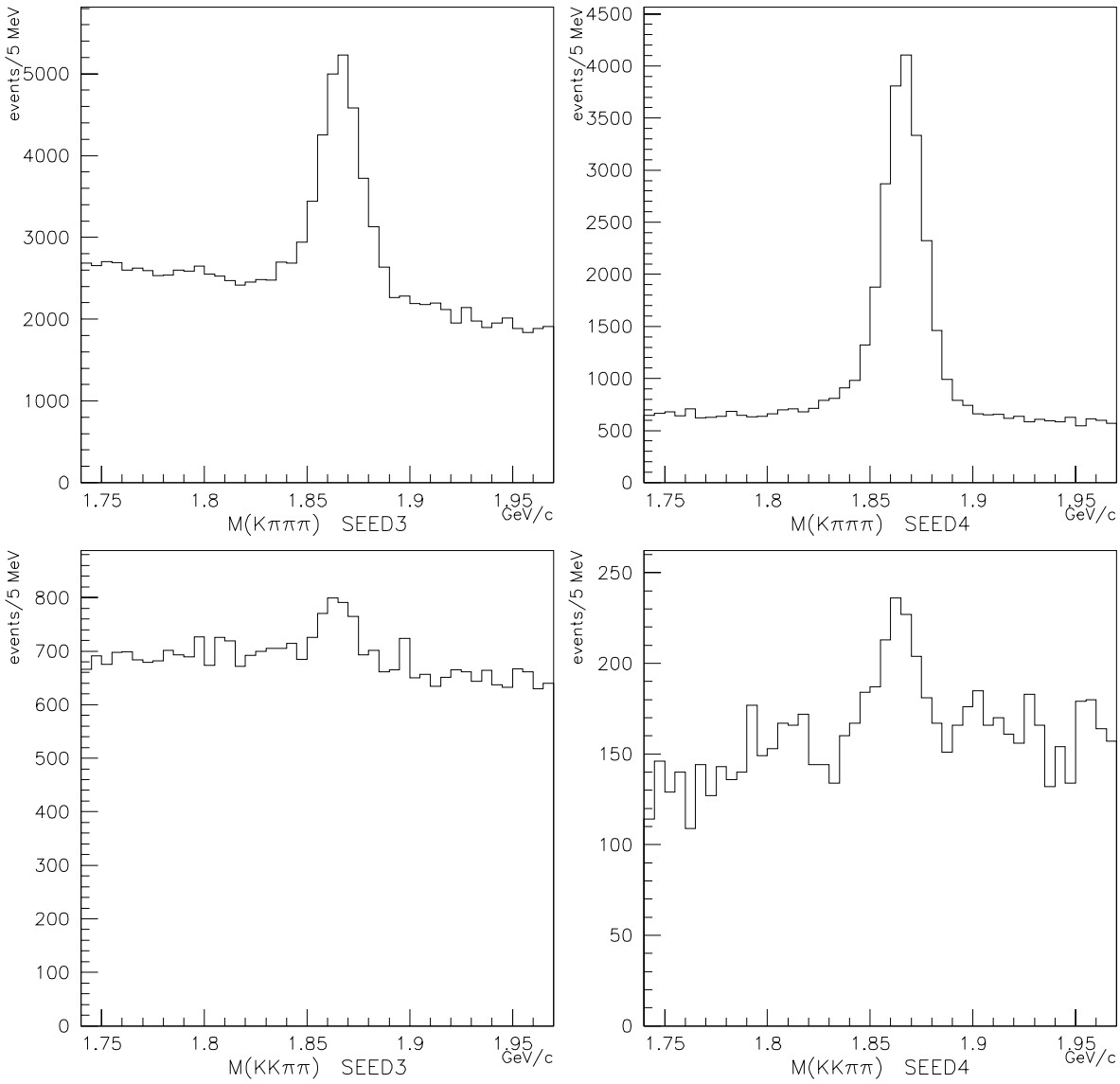

Figure 3.3: $K\pi\pi\pi$ and $KK\pi\pi$ invariant mass distributions from SEED4 and SEED3 events with strip level cuts

Chapter 4

$D^0 \to K^+K^-\pi^+\pi^-$ Branching Ratio

At the analysis stage, event selection cuts were optimized to obtain the $KK\pi\pi$ signal with the greatest sensitivity. The relative branching ratio $\frac{D^0 \to K^+K^-\pi^+\pi^-}{D^0 \to K^+\pi^-\pi^+\pi^-}$ was determined and the systematic errors were estimated.

4.1 Monte Carlo

Events generated by Monte Carlo simulations were used to study detector acceptance and reflections, to calculate normalizations in the fit, *etc.* The E791 Monte Carlo was used to generate Monte Carlo events. It used the LUND Monte Carlo package (JETSET 7.401 and PYTHIA 5.702 [25]) to simulate particle interaction and decays, propagated the generated particles through the detector with a detailed detector simulation, digitiized the detector output to simulate the actual digitization of the detector and wrote them to tapes in the same format as the actual data so that they could be read and used similarly to real data. In addition to digitized data, all relevant information on particles and tracks before digitization were written to the event record so that the reconstructed parameters could be compared with actual

values.

Figure 4.1 shows the background subtracted distribution [1] of various event parameters from reconstructed real and Monte Carlo events for the $D^0 \rightarrow K\pi\pi\pi$ signal. (Monte Carlo distributions have been normalized to the real data distributions). Monte Carlo distributions agree with data closely.

4.2 Optimization of Analysis Cuts

Figure 3.3 shows the $D^0 \rightarrow KK\pi\pi$ signal from the strip level cuts. For further analysis these signals were cleaned up using tighter cuts. Cuts were optimized to get a $D^0 \rightarrow KK\pi\pi$ signal with highest significance

$$\gamma = \frac{S}{\sqrt{S+B}} \tag{4.1}$$

where S is the number of signal events and B is the number of background events under the signal in a mass window of $\pm 3.5\sigma$ around the central value. (This assumed a linear background shape, σ was the width of the peak). To avoid tuning cuts to statistical fluctuation of the event sample used, S from a large $D^0 \rightarrow KK\pi\pi$ Monte Carlo event sample (after scaling to the expected signal level) and B from the wings of $D^0 \rightarrow KK\pi\pi$ data events were used. To account for different background levels (Figure 3.3) and other systematic differences between SEED3 and SEED4 events (Figures 4.2 and 4.3), cuts were separately optimized and applied to them.

[1] For all distributions in this chapter, the signal region was $|M(K\pi\pi\pi) - 1.865| < .020$ GeV, and the background region was $0.040 < |M(K\pi\pi\pi) - 1.865| < .060$ GeV. Background subtraction was done by subtracting background distribution from the signal region distribution.

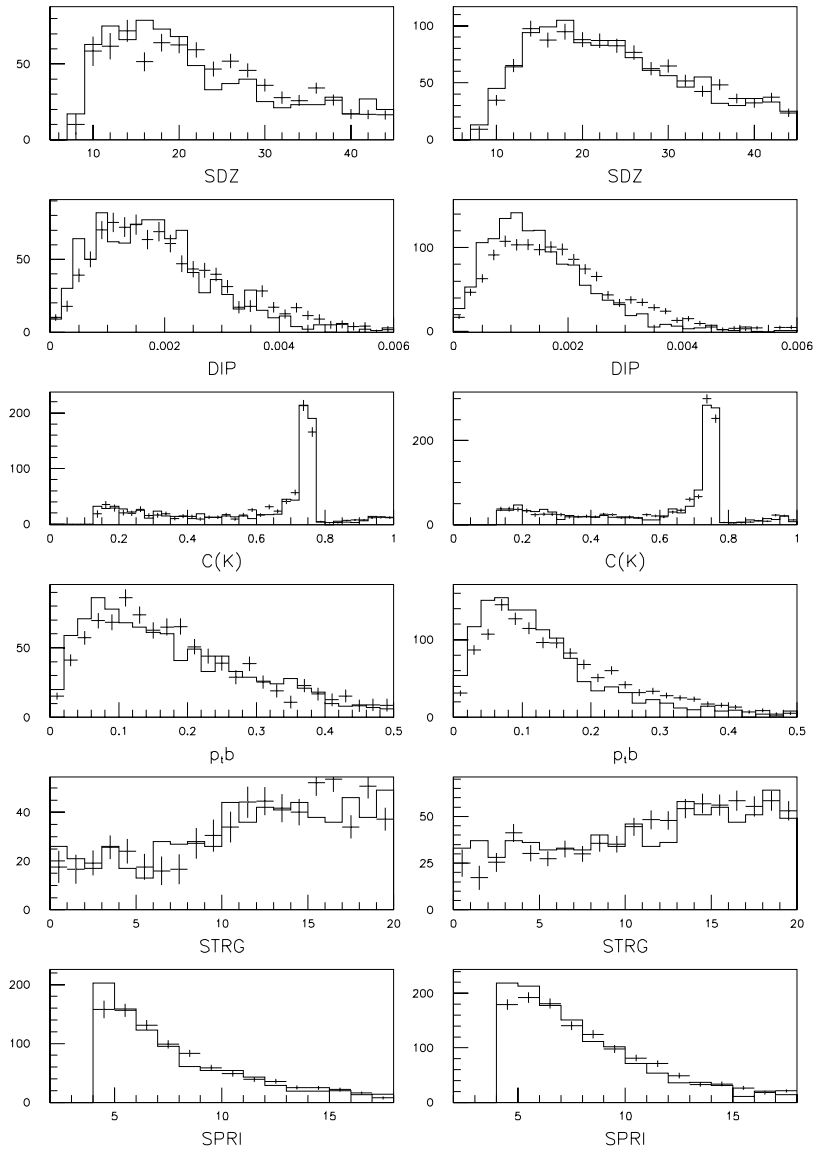

Figure 4.1: Comparison of background subtracted parameter distributions for data (curve) and Monte Carlo (points) for $D^0 \to K\pi\pi\pi$ events. Distributions from SEED3 events are in the left column and SEED4 in the right

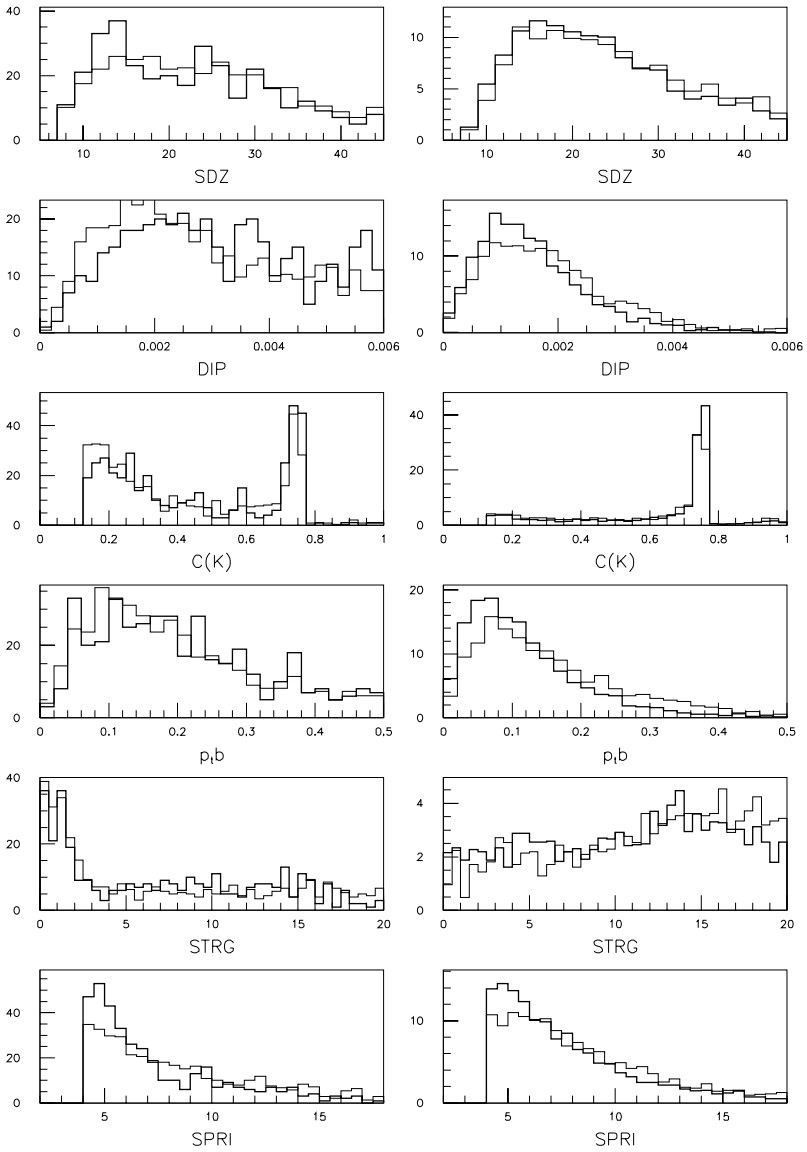

Figure 4.2: Parameter distributions of background (left) and background subtracted signal region (right) for $D^0 \to KK\pi\pi$ SEED4 events. (darker curve, signal from MC, background from data) and $D^0 \to K\pi\pi\pi$ (lighter curve, both signal and background from data.)

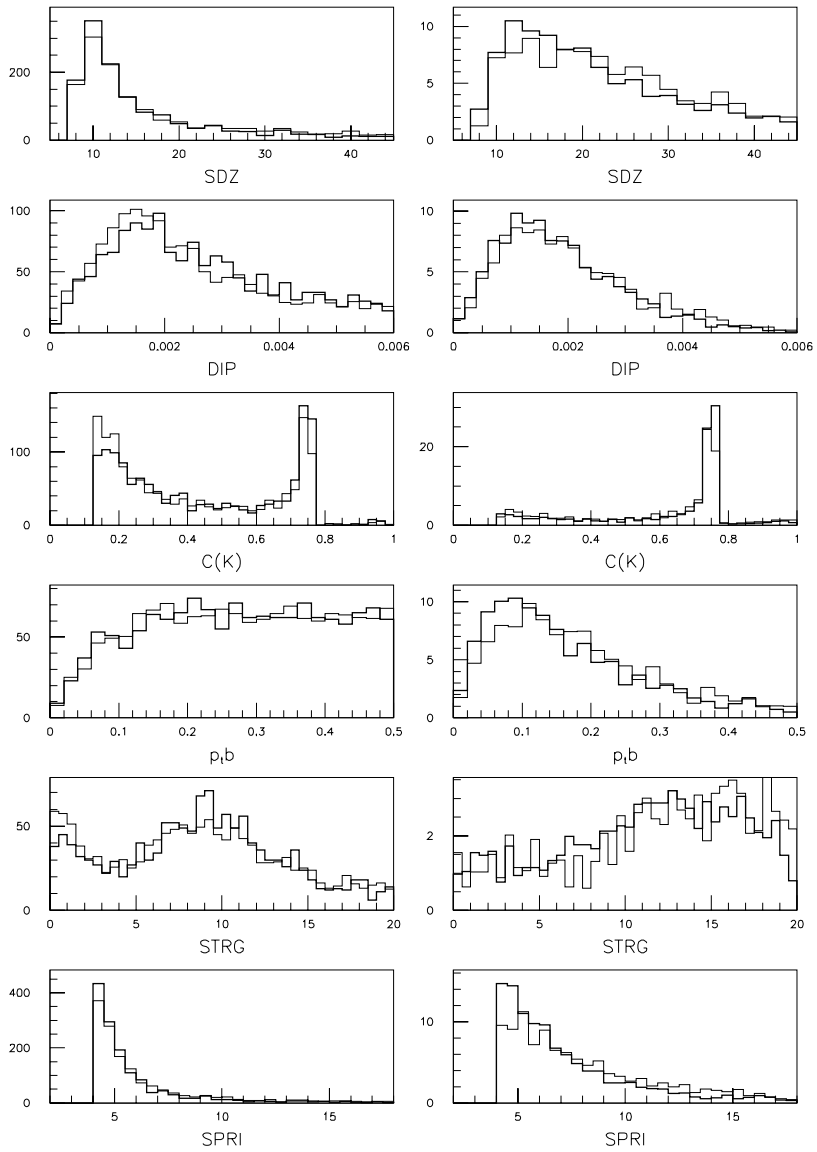

Figure 4.3: Parameter distributions of background (left) and background subtracted signal region for $D^0 \to KK\pi\pi$ SEED3 events. (darker curve, signal from MC, background from data) and $D^0 \to K\pi\pi\pi$ (lighter curve, both signal and background from data.)

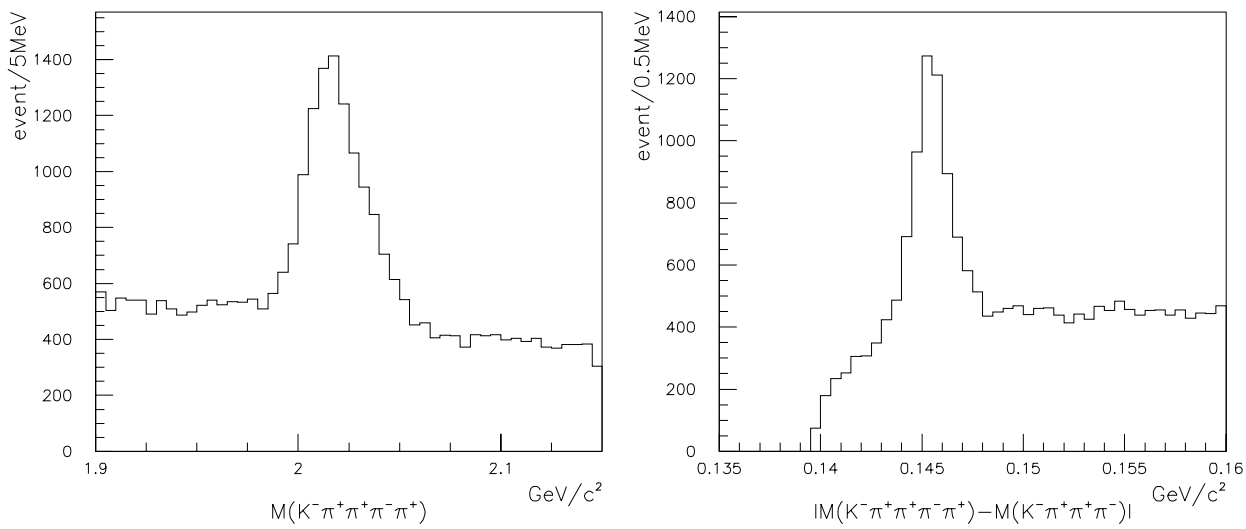

Figure 4.4: D^{*+} signal and ΔM distribution from $D^0 \to K\pi\pi\pi$ stripped events.

4.2.1 D^0 events from D^* s

About 20% of D^0 s came from D^{*+} decay via $D^{*+} \to D^0\pi^+$. Identification of the D^* from $D^0\pi^+$ combination enhanced the D^0 identification. D^{*+} s were tagged by combining the candidate D^0 with the remaining SESTR tracks (one at a time) to calculate the parent D^{*+} mass. ΔM defined by

$$\Delta M = |M(K^+K^-\pi^+\pi^-\pi^+) - M(K^+K^-\pi^+\pi^-)| \tag{4.2}$$

had a narrower width than the width of the D^{*+} distribution.(figure 4.4) Therefore a cut on ΔM ($|\Delta M - 0.1455| < 0.0015\ GeV/c^2$) was used as the D^{*+} tag. Since events with D^{*+} tag had a lower background, looser cuts were used for them.

Table 4.2 shows the analysis cuts chosen for the final analysis and Figures 4.5 and 4.6 shows the contributions from those four categories to the $D^0 \to K\pi\pi\pi$ and

cut	SEED4		SEED3	
	with D^* tag	no D^* tag	with D^* tag	no D^* tag
$p_T balance$ GeV	0.3	0.3	0.35	0.35
SDZ	8	10	8	14
$DIP(\mu m)$	35	35	35	35
C(K)	0.2	0.2	0.2	0.3
$STRG$	2	2.5	2	4
secondary vertex χ^2 <15				
$z_{sec} < -0.3cm$				
$SPRI > 4.5\sigma$				
Track Category (NEWCATSG)= $3, 7, 15$				

Table 4.1: Optimized analysis cuts

$D^0 \rightarrow KK\pi\pi$ signals. Figure 4.7 shows the D^0 signal from events with different tags. For $D^0 \rightarrow KK\pi\pi$ events, Cherenkov cuts were applied on both kaons. Figure 4.8 shows the total $D^0 \rightarrow KK\pi\pi$ and $D^0 \rightarrow K\pi\pi\pi$ signal after analysis cuts.

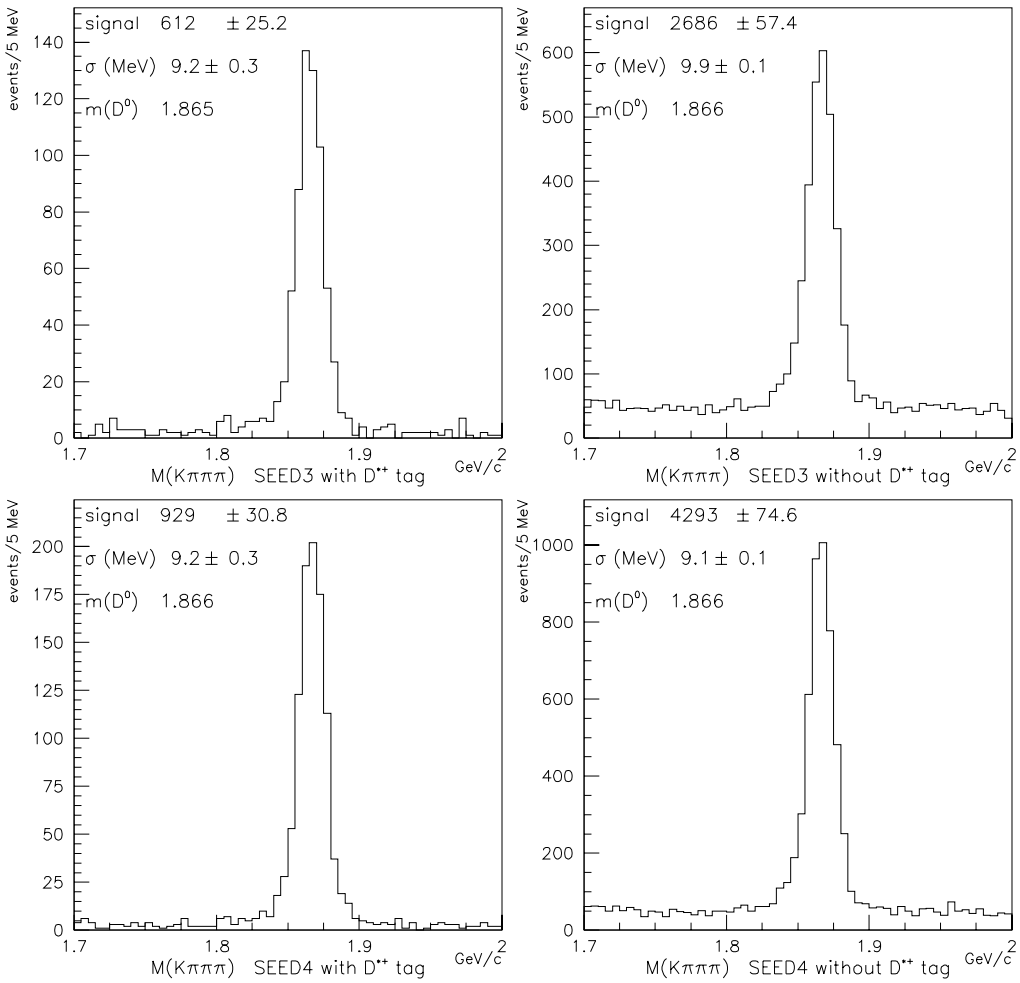

Figure 4.5: $D^0 \to K^-\pi^+\pi^+\pi^-$ signal from cuts optimized for $D^0 \to K^-K^+\pi^+\pi^-$.

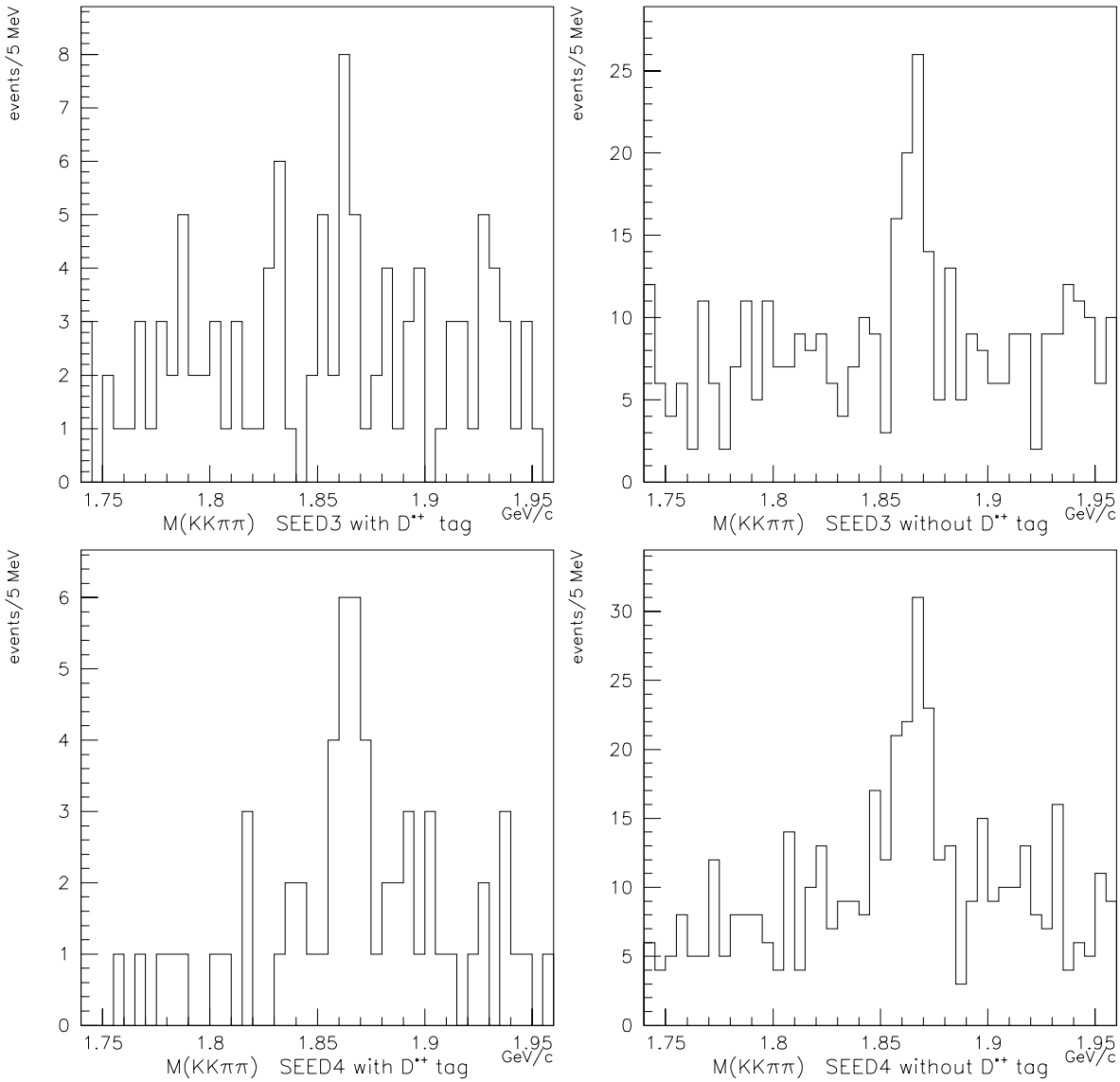

Figure 4.6: $D^0 \to K^+K^-\pi^+\pi^-$ signal from different cut categories.

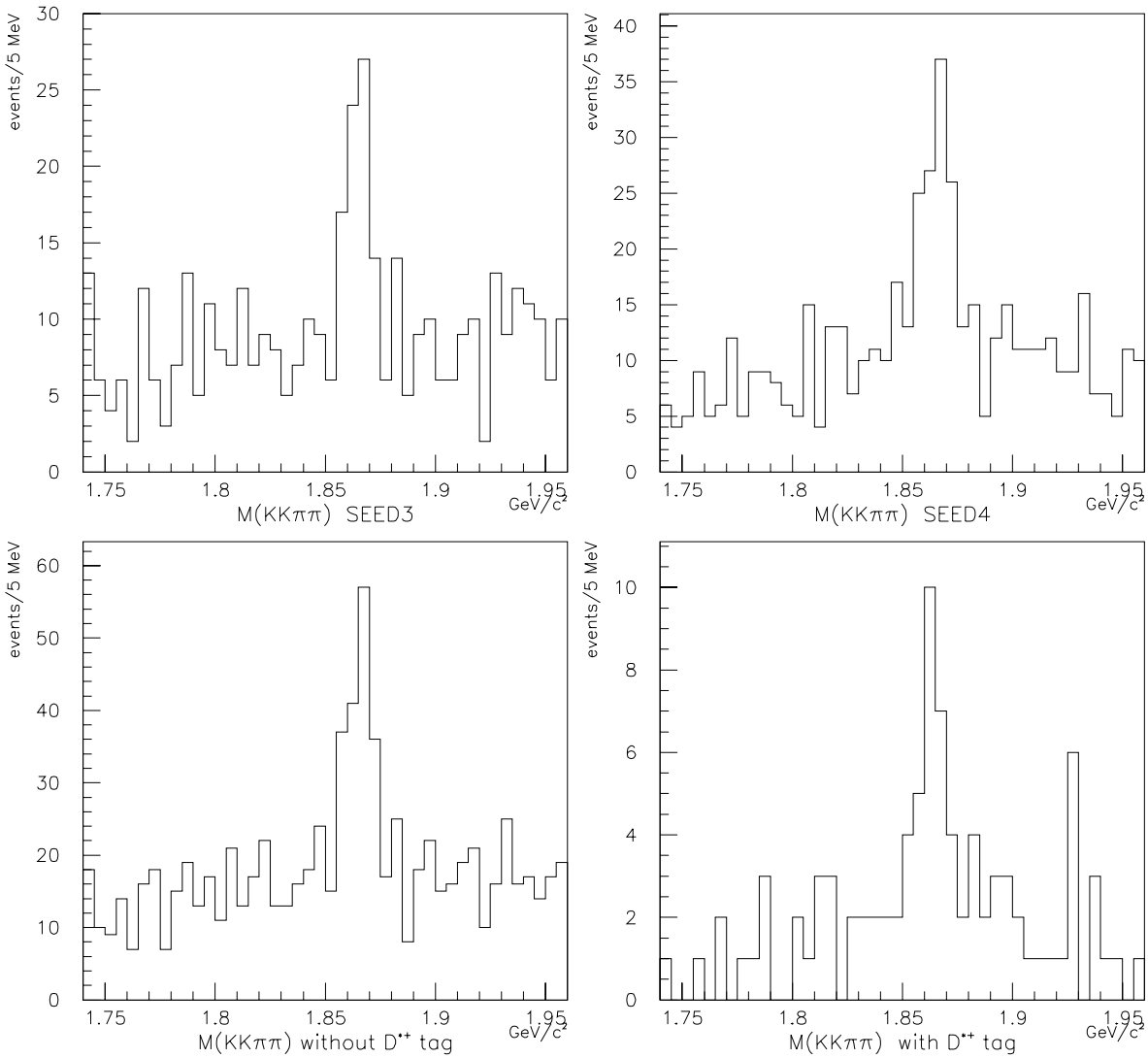

Figure 4.7: $K^+K^-\pi^+\pi^-$ mass distributions from events with different tags.

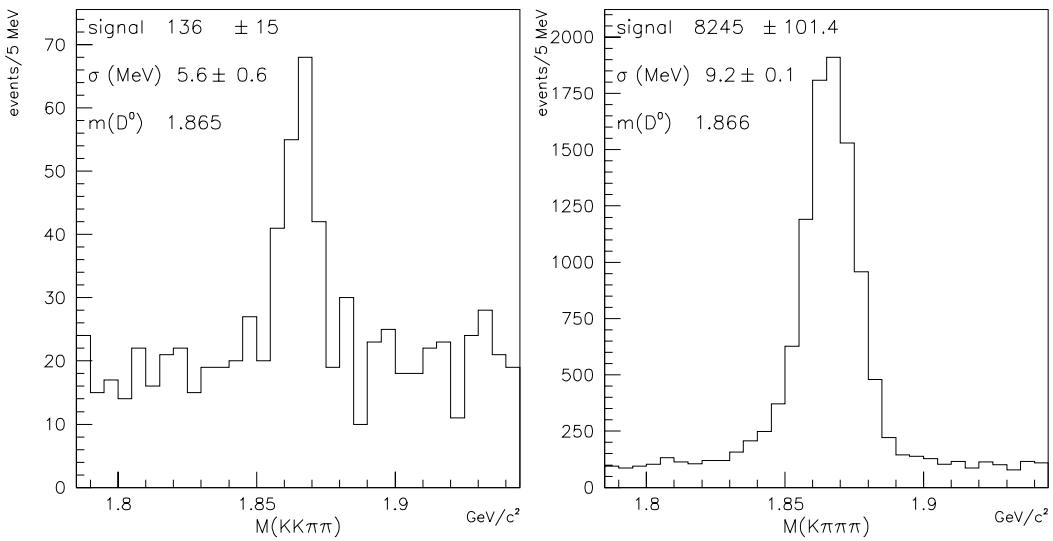

Figure 4.8: Total $D^0 \to K^+K^-\pi^+\pi^-$ and $D^0 \to K^-\pi^+\pi^-\pi^-$ signals after the analysis cuts.

4.3 Relative Branching Ratio

The relative branching ratio $\frac{D^0 \to K^+K^-\pi^+\pi^-}{D^0 \to K^-\pi^+\pi^+\pi^-}$ was measured by comparing the $KK\pi\pi$ and $K\pi\pi\pi$ signals. This is simply the ratio of $D^0 \to K^-K^-\pi^+\pi^-$ signal events to $D^0 \to K^-\pi^-\pi^+\pi^+$ signal events corrected for acceptances of the two decay modes. Monte Carlo events were used for acceptance correction. Since $K^+K^-\pi^+\pi^-$ has an extra Cherenkov cut on the kaons and since there may be systematic differences between Monte Carlo and data Cherenkov distributions, analysis cuts except the kaon Cherenkov cut were applied to the Monte Carlo samples for correcting for the acceptance. A correction was latter applied for the additional Cherenkov cut on the $K^+K^-\pi^+\pi^-$ sample. Without the Cherenkov correction,

Branching Ratio ($\frac{D^0 \to K^+K^-\pi^+\pi^-}{D^0 \to K^+\pi^-\pi^+\pi^-}$)

$$= \frac{\text{Signal}_{\text{K}^+\text{K}^-\pi^+\pi^-\ (\text{Data})}}{\text{Signal}_{\text{K}^+\pi-\pi^+\pi^-\ (\text{Data})}} \cdot \frac{\text{Signal}_{\text{K}^+\pi^-\pi^+\pi^-(\text{MC})}}{\text{Signal}_{\text{K}^+\text{K}^-\pi^+\pi^-(\text{MC})}} \cdot \frac{\text{K}^+\text{K}^-\pi^+\pi^-\text{MCevents used}}{\text{K}^+\pi - \pi^+\pi^-\text{MCevents used}} \quad (4.3)$$

Samples of one million $D^0 \to K^-\pi^-\pi^+\pi^=$ events and three million $D^0 \to K^+K^-\pi^+\pi^-$ events were used. All four event samples, Monte Carlo and real, $D^0 \to K^-K^-\pi^+\pi^-$ and $D^0 \to K^+\pi^-\pi^+\pi^-$, were fitted with a single maximum likelihood fit using the MINUIT [26] function minimization and error analysis package. Linear background and Gaussian signal shapes were assumed in the fit. Each signal was parameterized with the total number of signal events (S), mean of the Gaussian (m) and the width (σ). Backgrounds were parameterized with the number of background events (BG) (in a mass window from 1.785 -1.945 GeV/c^2) and the slope (s) of the assumed linear shape. In the fit, the $D^0 \to K^-K^-\pi^+\pi^-$ Monte Carlo signal was expressed in terms of the relative branching ratio so that it (with errors) was directly given by the fit. Table 4.2 shows the fit results and figure 4.9 shows the fit projections.

4.4 Systematic Errors

The measurement of the relative branching ratios has uncertainties from the following systematic effects. Each of them was studied and systematic errors associated with them were estimated.

4.4.1 Errors due to the Background Shape.

The assumed linear background shape is only an approximation and effects the number of signal events found by the fit. This effect was studied by fitting the data assuming a quadratic background shape. As shown in Figure 4.10, this gave a better fit to the background and the relative branching ratio was measured to be 0.0187 ± 0.0024,

Parameter	Value	Error
$S_{KK\pi\pi\ \mathrm{Data}}$	129.89	14.320
$S_{K\pi\pi\pi\ \mathrm{Data}}$	8490.8	103.2
$S_{K\pi\pi\pi\ \mathrm{MC}}$	5147.4	83.3
Branching Ratio	$0.18518\ 10^{-1}$	$0.224\ 10^{-2}$
$\sigma_{KK\pi\pi\ \mathrm{Data}}$	$0.52357\ 10^{-2}$	$0.69561\ 10^{-3}$
$\sigma_{K\pi\pi\pi\ \mathrm{Data}}$	$0.92316\ 10^{-2}$	$0.10620\ 10^{-3}$
$\sigma_{K\pi\pi\pi\ \mathrm{MC}}$	$0.74399\ 10^{-2}$	$0.12016\ 10^{-3}$
$\sigma_{KK\pi\pi\ \mathrm{MC}}$	$0.59184\ 10^{-2}$	$0.59876\ 10^{-4}$
$m_{KK\pi\pi\ \mathrm{Data}}$	1.8652	$0.72548\ 10^{-3}$
$m_{K\pi\pi\pi\ \mathrm{Data}}$	1.8661	$0.11960\ 10^{-3}$
$m_{K\pi\pi\pi\ \mathrm{MC}}$	1.8675	$0.15835\ 10^{-3}$
$m_{KK\pi\pi\ \mathrm{MC}}$	1.8667	$0.95737\ 10^{-4}$
$BG_{KK\pi\pi\ \mathrm{Data}}$	638.09	27.811
$BG_{K\pi\pi\pi\ \mathrm{Data}}$	3783.2	75.996
$BG_{K\pi\pi\pi\ \mathrm{MC}}$	4420.7	78.541
$BG_{KK\pi\pi\ \mathrm{MC}}$	7758.0	100.86
$s_{KK\pi\pi\ \mathrm{Data}}$	5.4982	5.3677
$s_{K\pi\pi\pi\ \mathrm{Data}}$	-4.1842	2.3222
$s_{K\pi\pi\pi\ \mathrm{MC}}$	17.528	2.0863
$s_{KK\pi\pi\ \mathrm{MC}}$	29.159	1.5284

Table 4.2: MINUIT results for the relative branching ratio fit (without the Cherenkov correction).

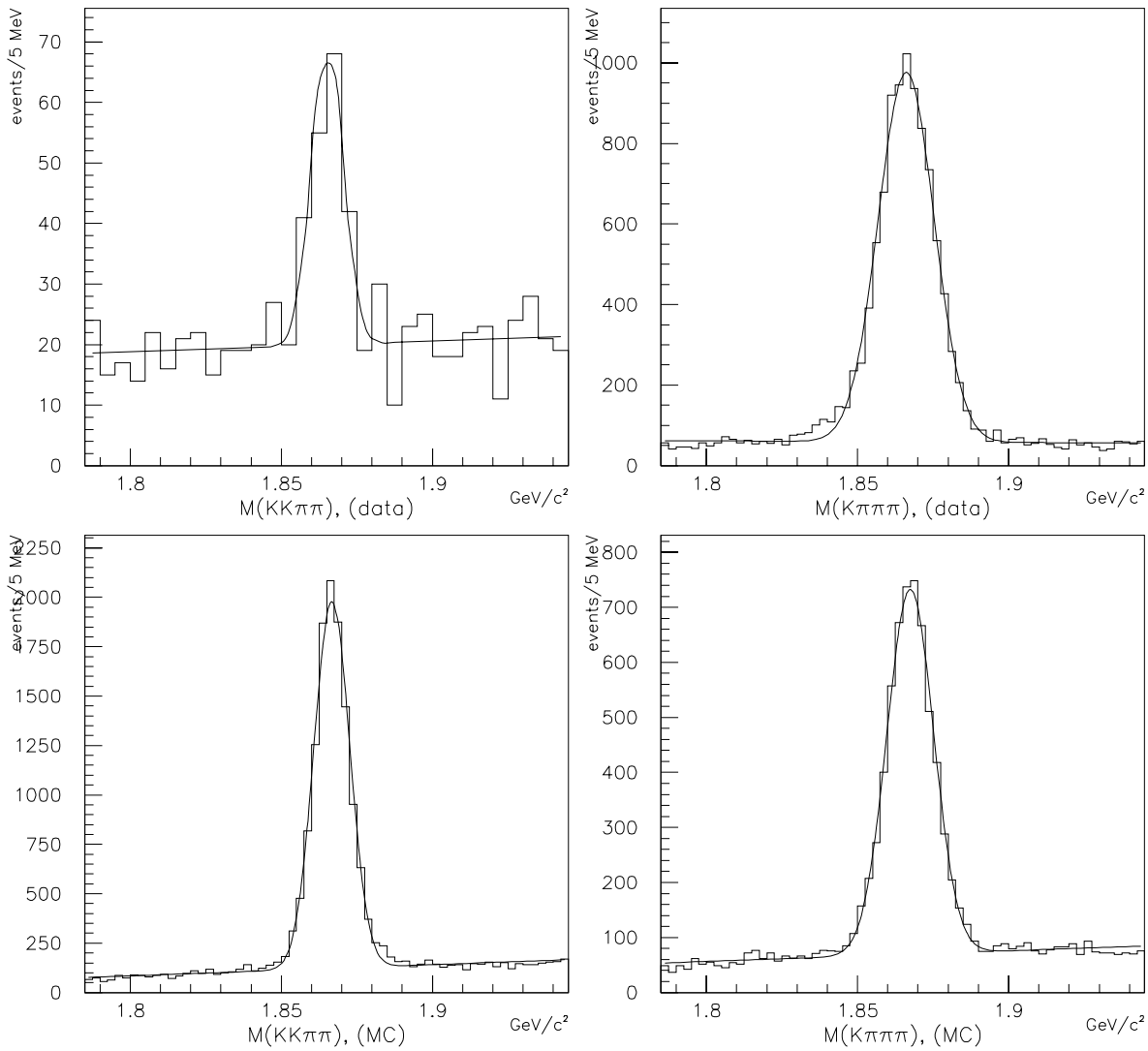

Figure 4.9: Fit projections on the $KK\pi\pi$ and $K\pi\pi\pi$ mass plots (with linear background shapes)

parameter	variation from optimized cut	relative branching ratio
DIP (μm)	-5	0.0191 ± 0.0025
	+5	0.0193 ± 0.0023
$p_T b$ GeV/c)	-0.05	0.0182 ± 0.0023
	+0.05	0.0180 ± 0.0031
SDZ	+1	0.0175 ± 0.0023
	-1	0.0188 ± 0.0026
C(K)	+.05	0.0180 ± 0.0023
	-.05	0.0186 ± 0.0023
SPRI	-0.5	0.0178 ± 0.0023
	+0.5	0.0183 ± 0.0025
STRG	+1	0.0180 ± 0.0022
	-1	0.0179 ± 0.0024

Table 4.3: Fluctuation of the branching ratio with analysis cuts.

almost unchanged (1.1%) from the previous value.

The mass window used to estimate background may also affect the estimated background shape, so another fit was done with a narrower mass window ($1.865 \pm .050$ GeV instead of $1.865 \pm .080$ GeV used in the original fit) which gave the branching ratio 0.184 ± 0.0018 , a change of 1.6%.

4.4.2 Biases in the Selection Criteria

A possible bias of analysis cuts on the event samples used may incorrectly estimate the branching ratio. The dependence of the branching ratio on the cuts used were studied by changing the cuts slightly from the optimized value and and estimating the branching ratio from the fit again.

Table 4.3 shows the variation of the relative branching ratio with different fit parameters. These results show that the relative branching ratio is fairly stable with respect to the variations of the analysis cuts. The systematic error due to the possible

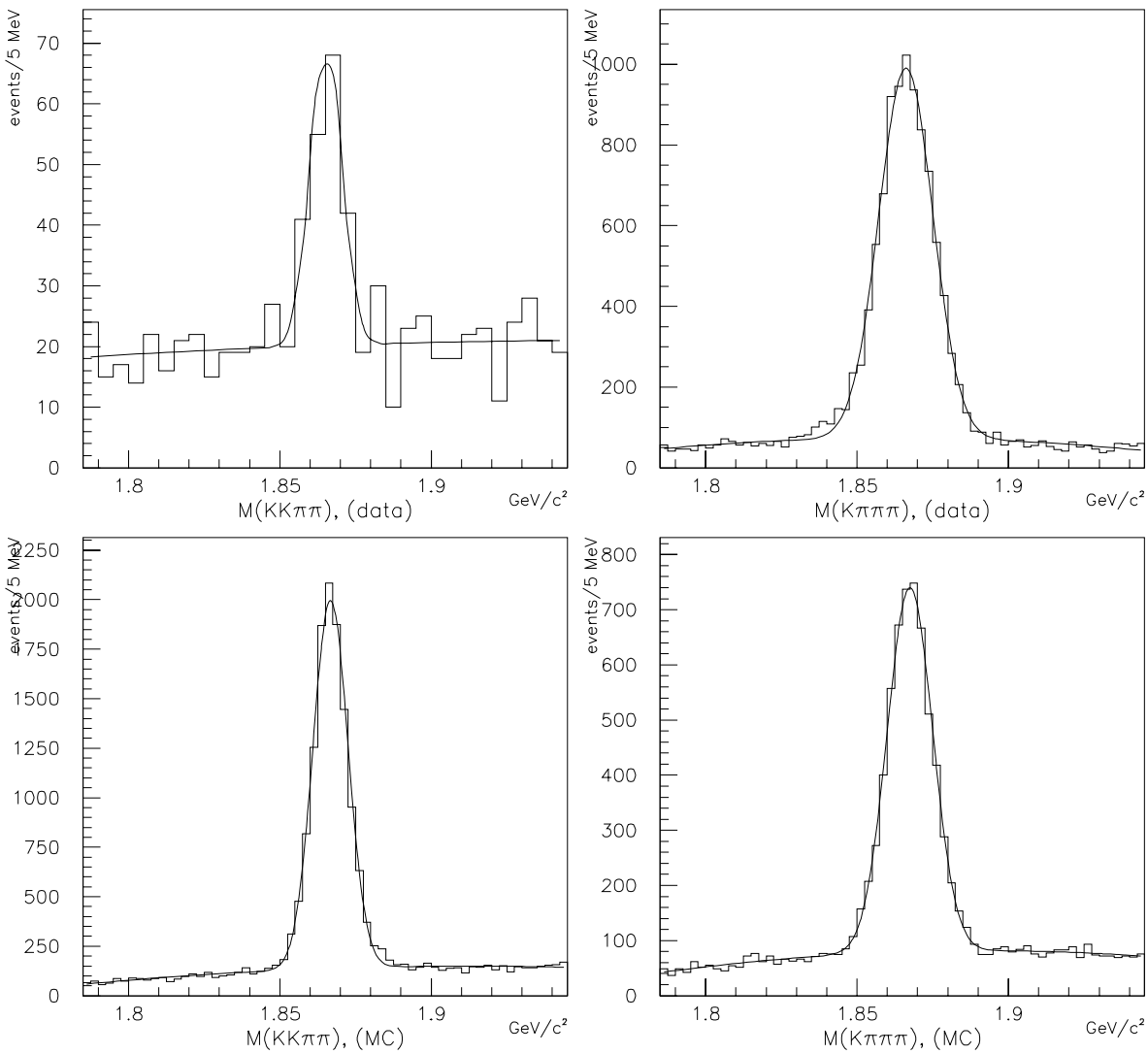

Figure 4.10: Fit projections on the $KK\pi\pi$ and $K\pi\pi\pi$ mass plots with quadratic background shapes.

	$KK\pi\pi$ signal	relative branching ratio
tight cuts	110 ± 16	0.0194 ± 0.0028
loose cuts	153 ± 20	0.0179 ± 0.0024
optimized cuts	130 ± 14.3	0.0185 ± 0.0022

Table 4.4: Relative branching ratio with different cuts.

bias of the branching to the cuts used was estimated by calculating the branching ratio with a tight and loose set of cuts. The tight and loose set of cuts used were the cuts shown in table 4.3 with all cuts at tighter or looser values respectively. Tight and loose cuts had $KK\pi\pi$ signals $\pm\sigma$ from the optimized cuts. Table 4.4 shows the results with tighter and looser cuts. Variation of the branching ratio with these cuts were less than 0.0009 from the optimized value, a 4.9% efect.

4.4.3 Variation of the Acceptance over the Phase Space

The acceptance of the detector may not be uniform over the entire $KK\pi\pi$ phase space. Both $D^0 \to KK\pi\pi$ and $D^0 \to K\pi\pi\pi$ have large numbers of resonant modes, so the acceptance correction done with non-resonant Monte Carlo may introduce an systematic error. This error was estimated by generating 250000 Monte Carlo events in different resonant modes and observing the variation of the reconstructed signals from different modes. As can be seen from Table 4.5, the root mean square variation of the acceptance is about 4.2% for $KK\pi\pi$ and about 1.1% for $K\pi\pi\pi$.

4.4.4 Charm Backgrounds

The backgrounds to $D^0 \to K^-K^+\pi^-\pi^+$ could be either random backgrounds (where four random tracks form a fake event) or can be due to reflections from other decays

mode	reconstruction efficiency%
$KK\pi\pi$ (nr)	0.179 ± 0.006
$K^{*0}K^{*0}$	0.195 ± 0.006
$K^{*0}K^{-}\pi^{+}$	0.185 ± 0.006
$\phi\pi^{+}\pi^{-}$	0.176 ± 0.006
$K\pi\pi\pi$ (nr)	0.249 ± 0.01
$K^{*0}\pi^{+}\pi^{-}$	0.252 ± 0.01
$K^{-}\pi^{+}\rho$	0.256 ± 0.01

Table 4.5: Reconstruction efficiency for different D^0 decay modes

misidentified as $D^0 \rightarrow K^-K^+\pi^-\pi^+$. Since they are resulting from charm decays, they can pass though most of the analysis cuts. It was important to study such reflections to make sure no known decays were faking the signal systematically. To study possible reflections, Monte Carlo events were generated in possible modes. They were reconstructed, and the $D^0 \rightarrow K^-K^+\pi^-\pi^+$ signal region from events passing the analysis cuts was examined for reflections.

Figure 4.11 shows the $KK\pi\pi$ mass distributions from reconstructed Monte Carlo events generated (142000 events in each mode) from different charm decay modes. There is no significant enhancement in the D^0 mass region in any of these distributions. The corrosponding plot from a 142,000 event $KK\pi\pi$ Monte Carlo sample is shown in Figure 4.12 for comparision.

4.4.5 Correction for Kaon Cherenkov Efficiency.

The efficiency of the cut on the kaon Cherenkov probability was estimated from $D^0 \rightarrow K^-\pi^+\pi^+\pi^-$ events substripped without a Cherenkov cut. To estimate the efficiency, D^0 signal from events that passed the analysis cuts and from the events that passed analysis cuts except the kaon Cherenkov cut were determined. These samples are shown in Figure 4.13. Fitting these data, the efficiency of the kaon

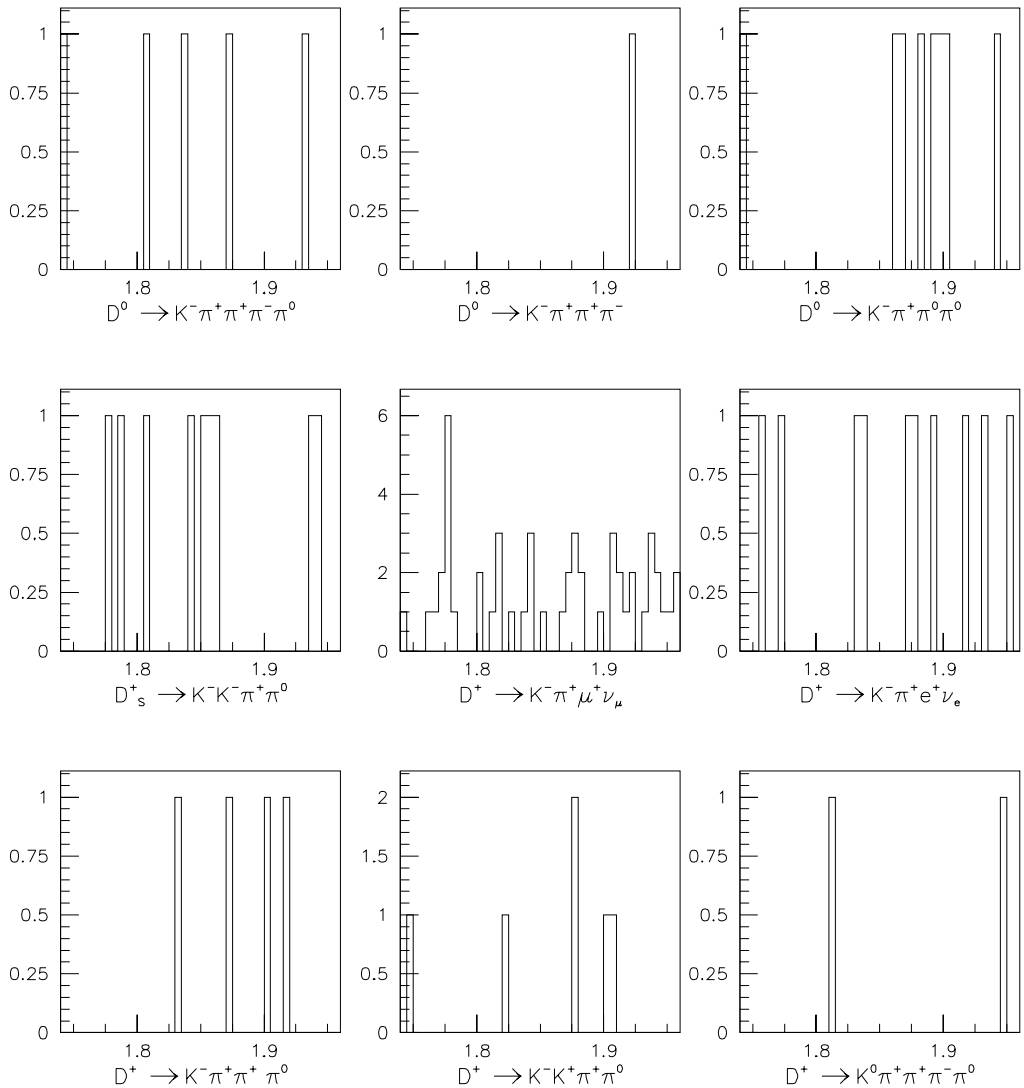

Figure 4.11: $K^+K^-\pi^+\pi^-$ mass plots from decay modes that can be misidentified as $D^0 \to K^-K^+\pi^-\pi^+$. Each plot comes from 142,000 generated Monte Carlo events

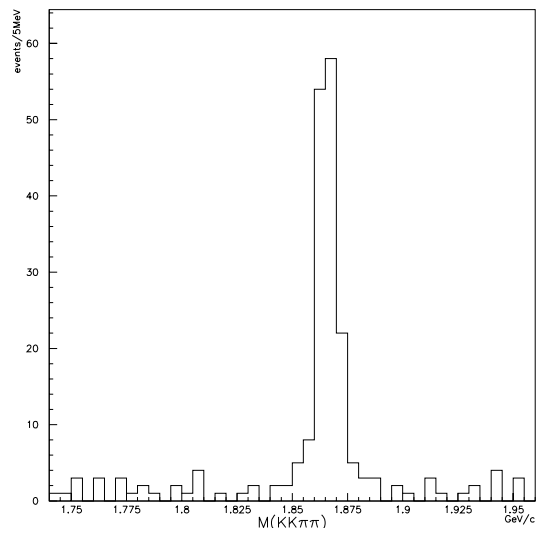

Figure 4.12: $K^+K^-\pi^+\pi^-$ mass plots from 142000 $D^0 \rightarrow K^-K^+\pi^-\pi^+$ Monte Carlo events

Cherenkov cut, is measure to be

$$\epsilon_{C(K)} = \frac{7874 \pm 103}{(7874 \pm 103) + (5419 \pm 124)}$$

$$= 0.59 \pm 0.01.$$

Comparing with similar studies by others[23], a 10% systematic error was assigned to the above calculated efficiency.

Since the Cherenkov cut was applied twice to $KK\pi\pi$ signal and only once to the $K\pi\pi\pi$ signal, correcting the branching ratio for Cherenkov efficiency,

$$\text{Relative B.R.} = \frac{0.0185 \pm 0.0022 \pm 0.0016}{\epsilon_{C(K)}}$$

$$= 0.0313 \pm 0.0037.$$

From Table 4.4, total systematic error is 11.8% =0.0036

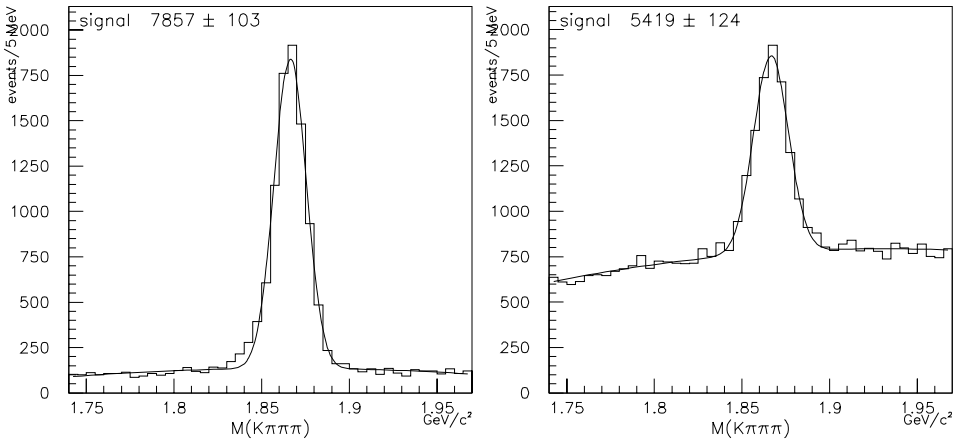

Figure 4.13: $K^+\pi^-\pi^+\pi^-$ mass plots from events which passed the analysis cuts (left) and from events which epassed the other analysis cuts but failed the Cherenkov cut (right).

source	error %
possible biases of cuts	4.2
background shape	1.1
mass window used	1.6
change in acceptance	4.1 ($KK\pi\pi$)
over phase space	1.3 ($K\pi\pi\pi$)
Cherenkov ID	10.0
Total	11.8

Table 4.6: Systematic errors for the branching ratio measurement

Therefore,

$$\text{Relative B.R. } \frac{\mathrm{D}^0 \to \mathrm{K}^+\mathrm{K}^-\pi^+\pi^-}{\mathrm{D}^0 \to \mathrm{K}^-\pi^-\pi^+\pi^-} = 0.0313 \pm 0.0037 \pm 0.0036.$$

Using Particle Data Group [30] value for the branching ratio of $D^0 \to K^-\pi^-\pi^+\pi^-$,

$$\mathrm{BR}(D^0 \to K^+K^-\pi^+\pi^-) = (0.0313 \pm 0.0037 \pm 0.0036) \cdot (8.1 \pm 0.5)\%$$

$$= 0.254 \pm 0.030 \pm 0.033\ \%$$

The uncertainty in the $D^0 \to K^-\pi^-\pi^+\pi^-$ branching ratio has been added in quadrature to the systematic error here.

Chapter 5

$D^0 \to K^+K^-\pi^+\pi^-$ Resonant Substructure

The resonant substructure of the decay $D^0 \to K^-K^+\pi^+\pi^-$ was studied qualitatively by making various two and three body invariant mass distributions. It was studied quantitatively using a maximum likelihood technique to estimate the contributions from different modes whose amplitudes were allowed to interfere coherently.

5.1 Resonant Mass Distributions

The decay $D^0 \to K^-K^+\pi^+\pi^-$ has a large number of possible decay modes with intermediate resonant modes as shown in Table 1.2. Some properties of these possible intermediate resonances are given Table 5.1. The five dimensional phase space of four-body decays makes it difficult to visualize the resonances in the decay. Unlike those of the non-resonant three body decays, there are no uniform Dalitz plot distributions [27] for four-body decays. Figures 5.1 and 5.2 show scatter plots of invariant mass combinations corresponding to the decays of resonant components versus $KK\pi\pi$ in-

variant mass from the data and from phase space Monte Carlo events passing the analysis cuts for comparison. There are clear indications for ϕ, $K^{*0}(892)$ and ρ in the D^0 mass region. An enhancement of events in the $K\pi\pi$ distributions near 1.3 GeV is also apparent.

The scatter plot of KK invariant mass versus $\pi\pi$ in Figure 5.3 shows some enhancement in the region corrosponding to $D^0 \to \phi\rho$. There also seems to be evidence for the presence of $D^0 \to K^{*0}\overline{K^{*0}}$ in the $K^-\pi^+$ versus $K^+\pi^-$ invariant mass scatter plots, though the broad $K^-\pi^+$ mass distribution of K^{*0} makes it difficult to draw a definite conclusion.

Figure 5.3 (c) shows the $\pi^+\pi^-$ mass distribution for events in the ϕ signal region, with backgrounds subtracted using events in the wings of the $KK\pi\pi$ mass distribution. Again, it shows the evidence for the presence of $\phi\rho$ signal. A similar projection for $K^{*0}\overline{K^{*0}}$ is shown in Figure 5.3 (d).

Figure 5.4 shows the one dimensional projections of the invariant mass distributions for signal and background region events, which shows some excess events in resonant mass regions. However excess events in an invariant mass distribution may also result from the kinematic effects of other resonances present. This can be seen in Figure 5.5-5.7 where various invariant mass distributions from $D^0 \to K^+K^-\pi^+\pi^-$ phase space, $D^0 \to K^{*0}(892)K^-\pi^+$, and $D^0 \to \phi\pi^-\pi^+$ Monte Carlo are shown. For example, in Figure 5.6, due to the presence of ϕ there is an enhansment of events in the high end of $\pi\pi$ mass distribution and depletions in the low end of $K\pi\pi$ distributions comparerd to phase space. In Figure 5.7, the presence of $K^{*0}(892)$ has resulted in different distriutions for $K^+\pi^-\pi^+$ and $K^-\pi^-\pi^+$.

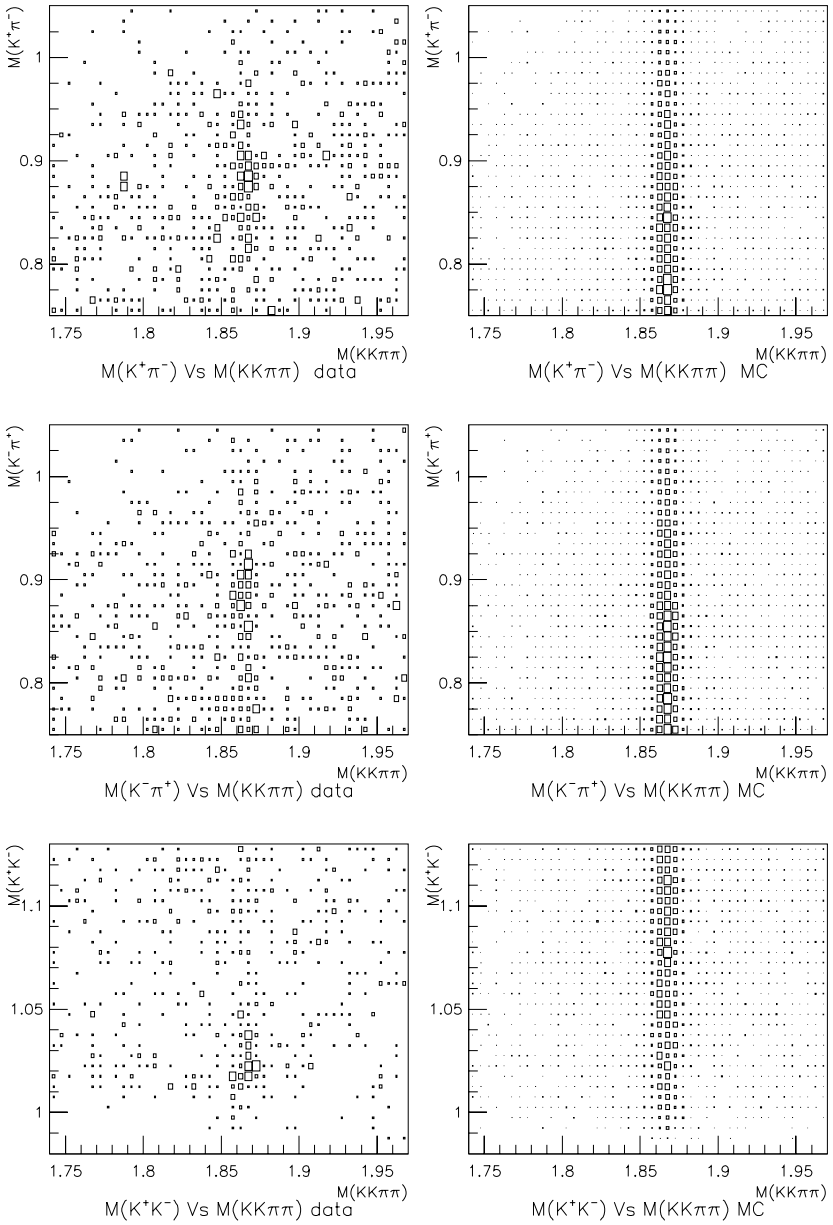

Figure 5.1: Invariant mass distributions of $K\pi$ and KK versus $KK\pi\pi$ mass for data (left) and for non-resonant $D^0 \to KK\pi\pi$ Monte Carlo events (right). (All masses are in GeV.)

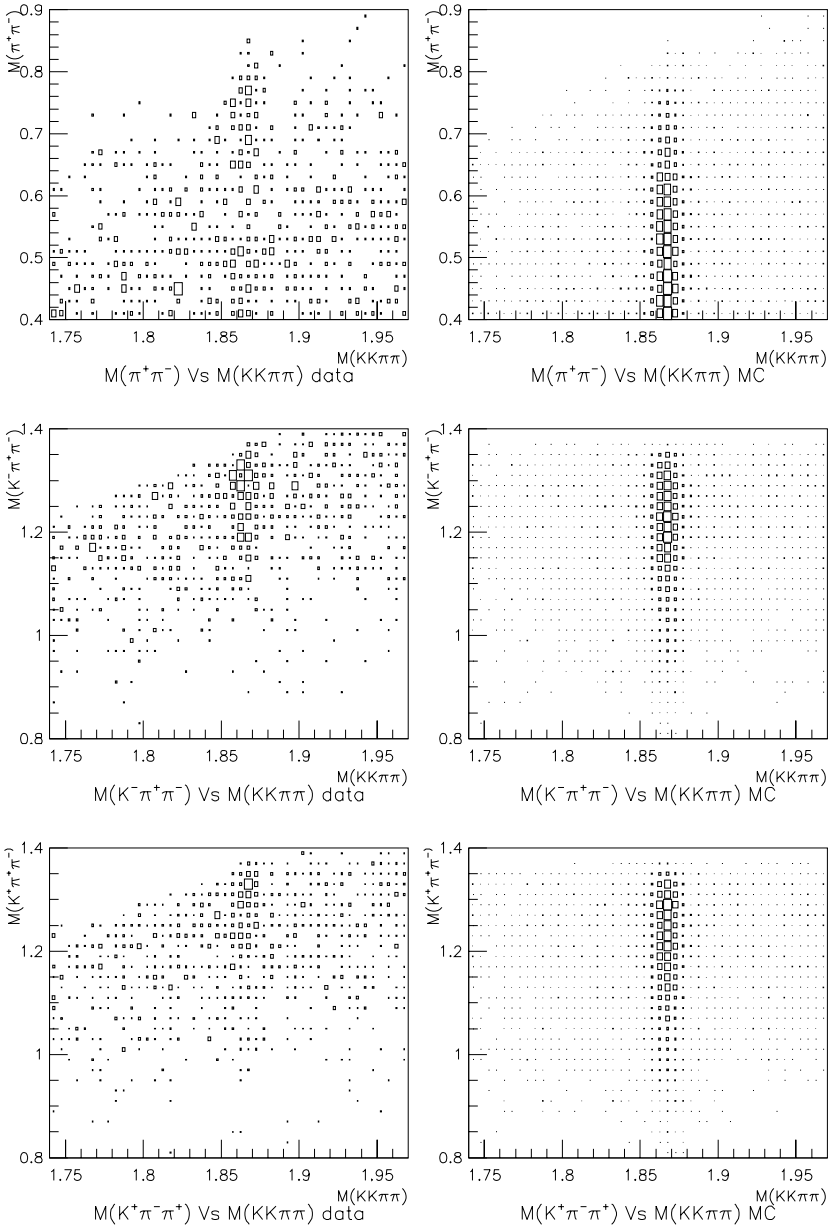

Figure 5.2: Invariant mass distributions of $\pi\pi$ and $K\pi\pi$ versus $KK\pi\pi$ mass for data (left) and for non-resonant $D^0 \to KK\pi\pi$ Monte Carlo (right). (All masses are in GeV.)

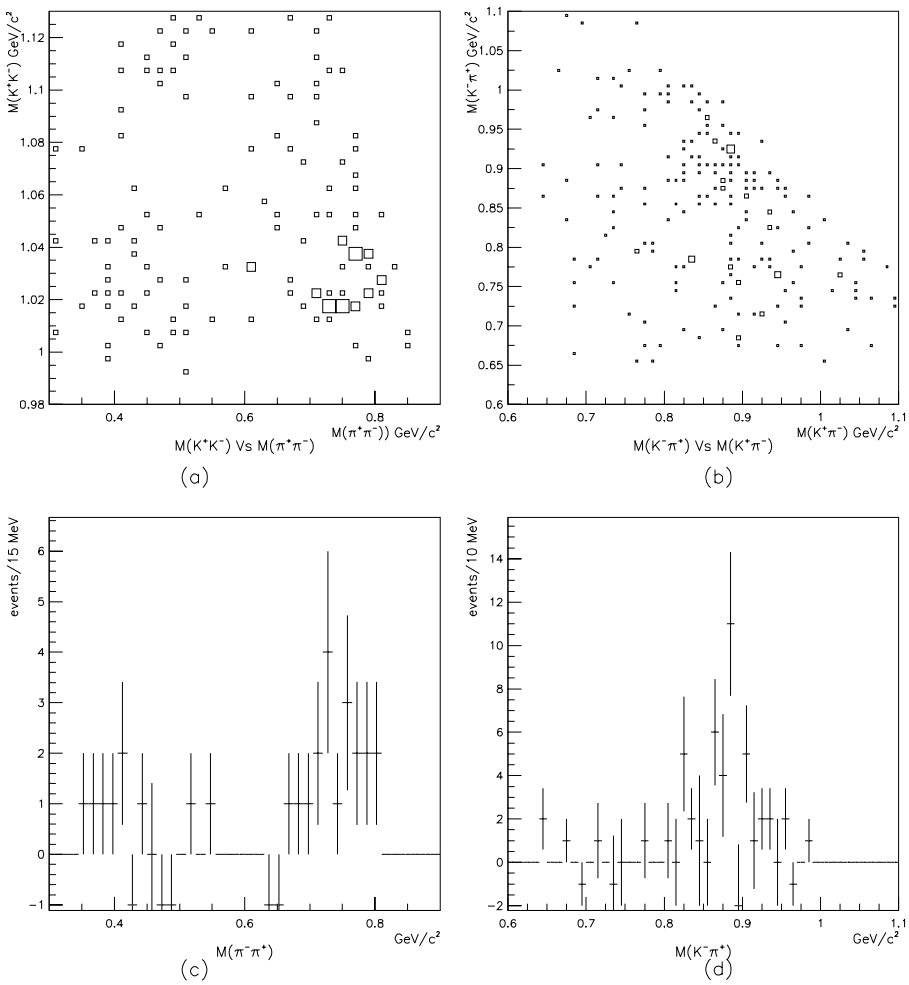

Figure 5.3: Invariant mass distributions for possible resonances for events in the D^0 signal region (a) $M(\pi^+\pi^-)$ versus $M(K^+K^-)$ for $|M(KK\pi\pi) - 1.866| < .012$ GeV (b) $M(K^-\pi^+)$ versus $M(K^+\pi^-)$ for $|M(KK\pi\pi) - 1.866| < .012$ GeV (c) $M(\pi^+\pi^-)$ for $|M(K^+K^-) - 1.020| < 0.006$ GeV for events in D^0 signal region (background subtracted) (d) $M(K^+\pi^-)$ for $|M(K^-\pi^+) - 0.896) < .050$ GeV for events in D^0 signal region (background subtracted).

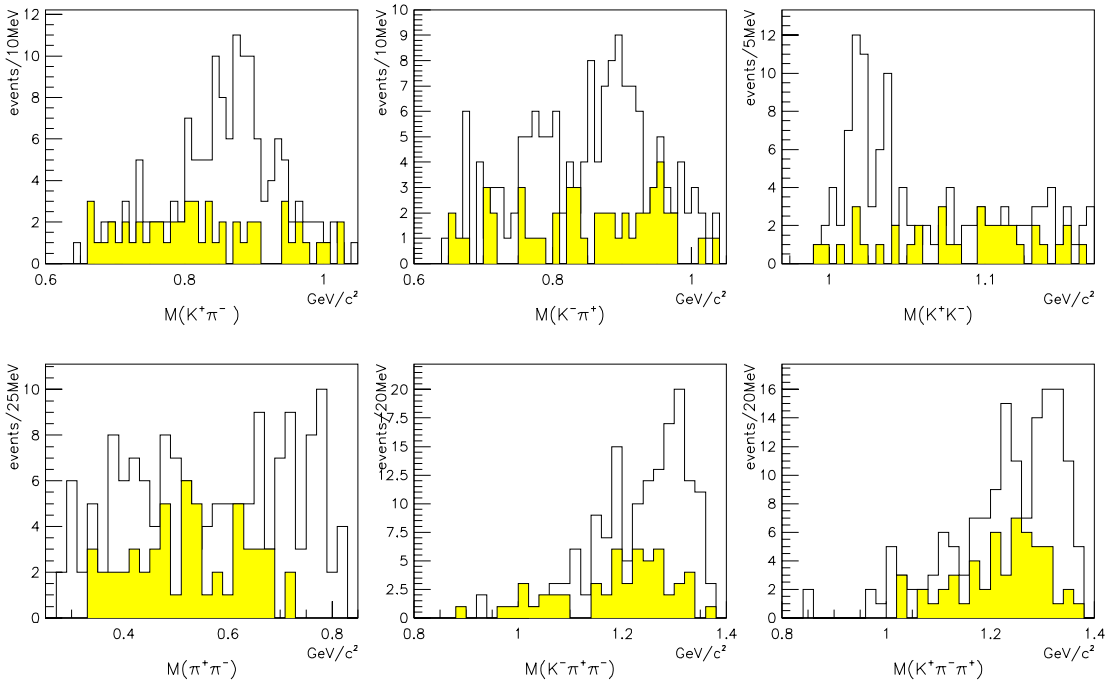

Figure 5.4: Invariant mass distributions for events in the D^0 signal region ($|M(KK\pi\pi) - 1.865| < 0.012$ GeV, solid curve) and background region ($0.018 < |M(KK\pi\pi) - 1.865| < 0.030$ GeV, shaded.)

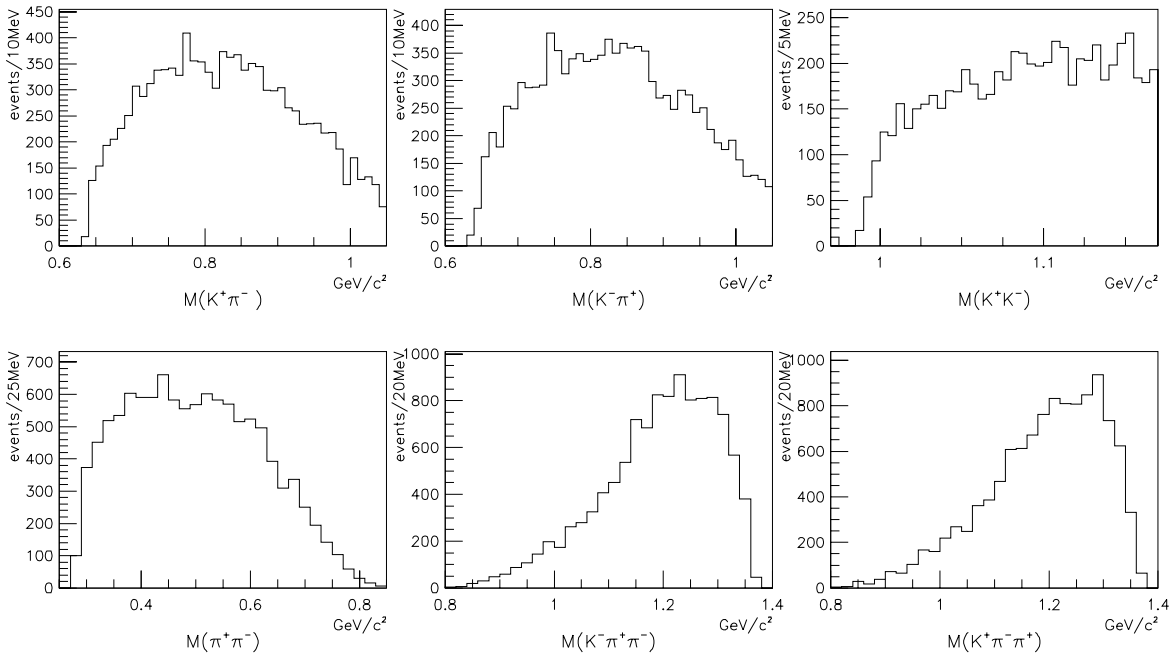

Figure 5.5: Invariant mass distributions from $D^0 \to K^+K^-\pi^+\pi^-$ phase space Monte Carlo events

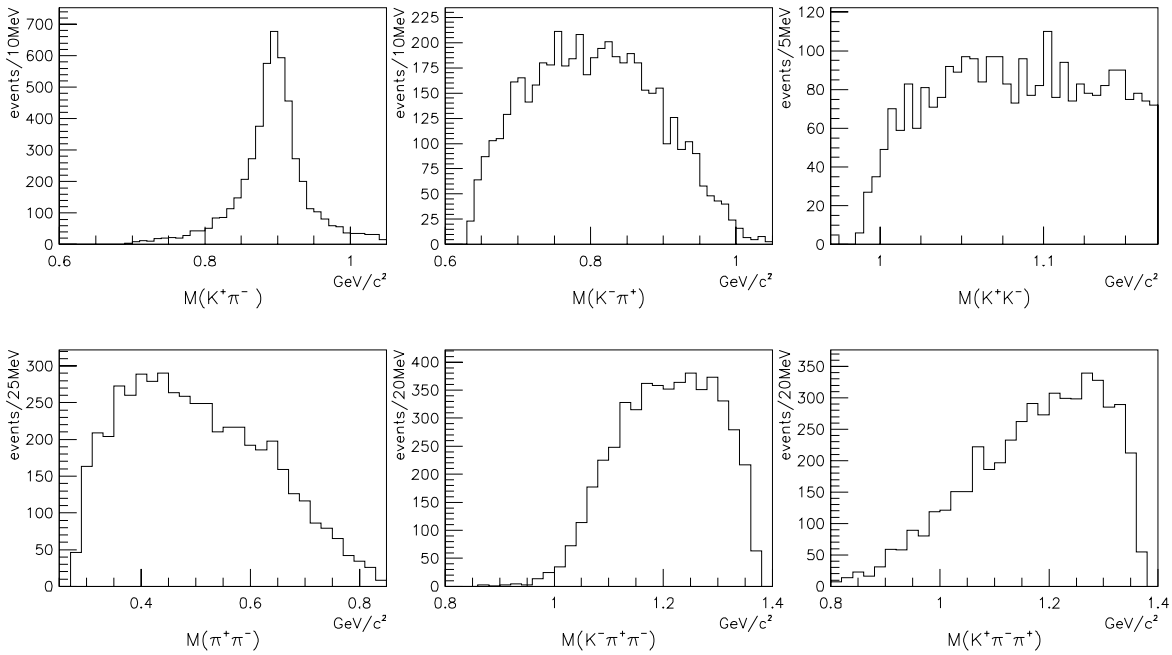

Figure 5.6: Invariant mass distributions for $D^0 \to K^{*0}(892)K^-\pi^+$ Monte Carlo events

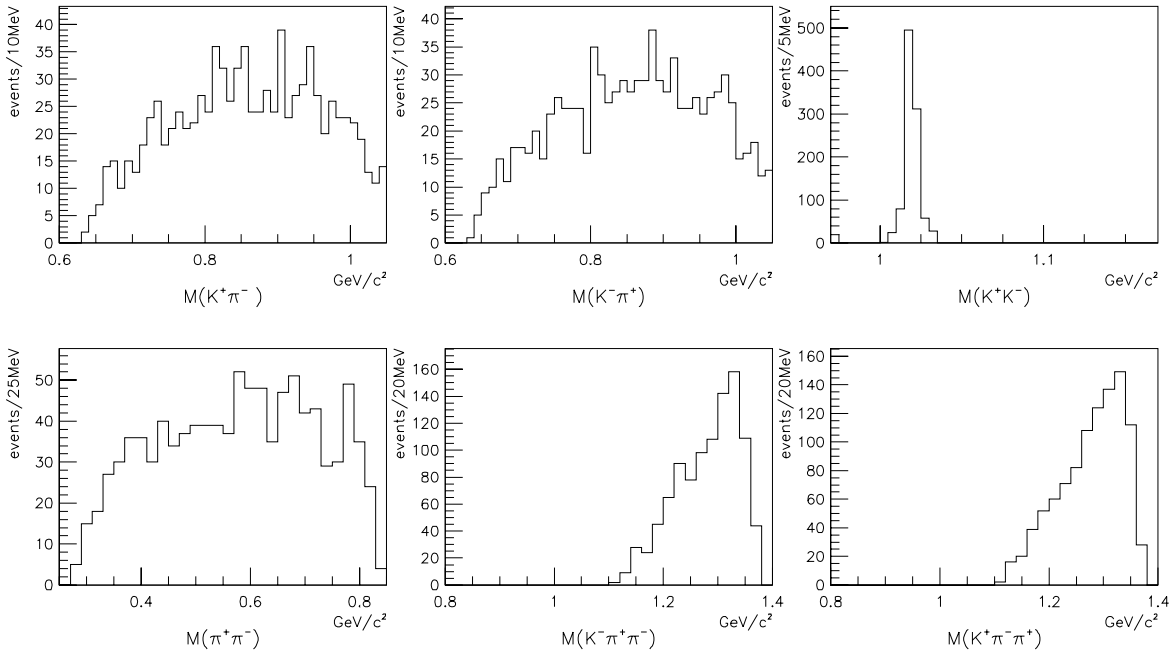

Figure 5.7: Invariant mass distributions from $D^0 \to \phi\pi^-\pi^+$ Monte Carlo events

Resonance	$I(J^P)$	mass (MeV)	width (MeV)	decay mode	% fraction
ϕ	$1(1^-)$	1019.4 ± 0.008	4.43 ± 0.06	K^+K^-	49.1
$\rho(770)$	$1(1^-)$	769.9 ± 0.8	151.2 ± 1.2	$\pi\pi$	100
$K^{*0}(892)$	$\frac{1}{2}(1^-)$	896.1 ± 0.28	49.8 ± 0.8	$K^+\pi^-$	66.6
$K_1^+(1270)$	$\frac{1}{2}(1^+)$	1273 ± 7	90 ± 20	$K^+\rho$	42.6
				$K_0^*(1430)\pi^+$	28
				$K^{*0}(892)\pi$	16
$K_1^+(1400)$	$\frac{1}{2}(1^+)$	1402 ± 7	174 ± 13	$K^{*0}(892)\pi$	94
$K_1^+(1410)$	$\frac{1}{2}(1^-)$	1412 ± 7	227 ± 22	$K^{*0}(892)\pi$	> 40

Table 5.1: properties of some possible resonances in $D^0 \to KK\pi\pi$ [29]

5.2 The Fitting Technique

The resonant substructure of $D^0 \to K^+K^-\pi^+\pi^-$ was estimated quantitatively using a maximum likelihood technique. This is similar to the techniques used by other experiments to measure resonant substructure in three and four-body decays [3] [4]. The likelihood function was defined in terms of a probability density function (PDF) for the decay to have particular resonant components. The likelihood was maximized with respect to the parameters (amplitudes, phases, *etc.*) which define the resonant substructure.

5.2.1 The Likelihood Function

The likelihood function $\mathcal{L}$ has the following form:

$$\mathcal{L} = \frac{e^{\nu}\nu^n}{n!}\prod_{i=1}^{n}\mathcal{P}_i \tag{5.1}$$

where n is the number of events in the data sample

ν is the number of events estimated by the fit,

i.e.

$$\nu = S + B \tag{5.2}$$

S and B are number of signal and background events determined by the fit.

$\mathcal{P}_i$ is the probability of occurring the ith event. An event can be a either $D^0 \rightarrow K^+K^-\pi^+\pi^-$ or a background event. So $\mathcal{P}_i$, can be written in terms of the probability of observing a signal $\mathcal{P}_{iS}$ and the probability of observing a background event $\mathcal{P}_{iB}$ as

$$\mathcal{P}_i = \frac{S \cdot \mathcal{P}_{iS} + B \cdot \mathcal{P}_{iB}}{S + B}. \tag{5.3}$$

5.2.2 Signal Probability Distribution Function.

The transition probability for a $D^0 \rightarrow F$ with final state at the point ϕ in the phase space is

$$p_S(\phi) = | < D^0|F(\phi) > |^2 d\phi \tag{5.4}$$

If this transition could occur via m intermediate modes X_i, p_S can be written as

$$p_S(\phi) = |\sum_{i=1}^{m} < D|X_i >< X_i|F(\phi) > |^2 d\phi \tag{5.5}$$

This can be rewritten as

$$p_S(\phi) \propto |\sum_{i=1}^{m} a_i S_i(\phi)|^2 d\phi \tag{5.6}$$

where a_i is a complex amplitude for the ith mode. S_i is the transition matrix of the decay $< D|X_i >< X_i|F >$, which is normalized such that

$$\int_{phase\ space} S_i S_i^* d\phi = 1. \tag{5.7}$$

Writing a_i as $A_i e^{i\alpha_i}$ (for later convenience),

$$p_S(\phi) \propto |A_1 e^{i\alpha_1} S_1 + A_2 e^{i\alpha_2} S_2 + ...A_m e^{i\alpha_m} S_m|^2 d\phi. \tag{5.8}$$

Therefore, the probability for D^0 to decay as $KK\pi\pi$ according to this superposition of modes (substructure) and to be detected at ϕ is

$$\mathcal{P}_S(\phi) \propto \epsilon(\phi)|\mathcal{A}_\infty]^{\rangle\alpha_\infty}\mathcal{S}_\infty + \mathcal{A}_\in]^{\rangle\alpha_\in}\mathcal{S}_\in + ...\mathcal{A}_\Updownarrow]^{\rangle\alpha_\Updownarrow}\mathcal{S}_\Updownarrow|^{\in}\lceil\phi. \tag{5.9}$$

where $\epsilon(\phi)$ is the detector acceptance. This can be written as:

$$\mathcal{P}_S(\phi) \propto \epsilon(\phi)\sum_{j=1}^{m}\sum_{k=1}^{m} A_j A_k \mathcal{R}e(e^{i(\alpha_j-\alpha_k)} S_j S_k^*) d\phi \tag{5.10}$$

Since a detected event should have been generated somewhere in phase space,

$$\int_{phase\ space} \mathcal{P}_S d\phi = 1. \tag{5.11}$$

Thus,

$$P_S = \frac{1}{N_S}\epsilon(\phi)\sum_{j=1}^{m}\sum_{k=1}^{m} A_j A_k \mathcal{R}e(e^{i(\alpha_j-\alpha_k)} S_j S_k^*) d\phi \tag{5.12}$$

where N_S is the overall normalization defined by

$$N_S = \sum_{j=1}^{m}\sum_{k=1}^{m} A_j A_k \mathcal{R}e(e^{i(\alpha_j-\alpha_k)} E_{jk}) \tag{5.13}$$

and

$$E_{jk} = \int_{phase\ space} \epsilon S_j S_k^* d\phi. \tag{5.14}$$

Equation 5.12 gives the probability for a $D^0 \rightarrow K^+K^-\pi^+\pi^-$ event to decay at ϕ given the particular resonant substructure. The total signal probability distribution function is the product of this and the probability of observing a $D^0 \rightarrow K^+K^-\pi^+\pi^-$ event. Since detector resolution gives the $K^+K^-\pi^+\pi^-$ mass distribution a Gaussian form, the probability for an event to be a $D^0 \rightarrow K^+K^-\pi^+\pi^-$ was assumed to be given by

$$\frac{1}{\sqrt{2\pi}\sigma} \exp\left(\frac{-(M_i - M_0)^2}{2\sigma^2}\right). \tag{5.15}$$

Here, M_i is the observed $K^+K^-\pi^+\pi^-$ invariant mass, M_0 and σ are the mean and width of the $K^+K^-\pi^+\pi^-$ mass distribution. Therefore, the total signal PDF is

$$\mathcal{P}_S = \frac{1}{\sqrt{2\pi}\sigma} \exp\left(\frac{-(M - M_0)^2}{2\sigma^2}\right). \frac{1}{N_S} \left| \sum_{j=1}^{m} \sum_{k=1}^{m} A_j A_k \mathcal{R}e(e^{i(\alpha_j - \alpha_k)} S_j S_k^* \right| d\phi. \tag{5.16}$$

5.2.3 Background Probability Distribution.

Backgrounds may come to the event sample as a random background or as a misidentified charm background. In either case there can be some resonances contained in the background. The background probability distribution function must account for all these contributions.

For the signal, the different amplitudes are coherent. For the background they are not. If the $D^0 \rightarrow KK\pi\pi$ consists of four random tracks or a misidentified D^0 decay with tracks from a D combined with a random track (*eg.* $D^+ \rightarrow K^+K^-\pi^+$ with one random track) or a D^0 decay with one of its decay tracks lost (*eg.* $D^0 \rightarrow$

$K^-\pi^+\pi^+\pi^-\pi^0$), then any signals would not be expected to keep a coherent phase relationship with each other. The only exception would be D^0 background from four tracks coming from $D^0 \to K\pi\pi\pi$ which should be treated coherently. However, the $KK\pi\pi$ mass window selected for the fit (1.835 GeV to 1.895 GeV) removed virtually all these events explicitly from the event sample. So only incoherent backgrounds were considered.

Therefore,

$$P_B = \frac{1}{N_B}\sum_j^l b_j \cdot B_j d\phi \tag{5.17}$$

where l is the number of possible backgrounds, b_j are numbers proportional to the fraction of each background and B_j are the functions which describe the backgrounds. They are normalized such that

$$\int_{phase\ space} B_j d\phi = 1 \tag{5.18}$$

and N_B is the overall normalization of the background

$$N_B = \int_{phase\ space} P_B d\phi \tag{5.19}$$

$$= \sum_j^l b_j \tag{5.20}$$

Similar to the signal PDF, the total background PDF is the product of the probability of observing a background event and the background event to have a particular background structure. As shown in the previous chapter, the background distribution in $KK\pi\pi$ mass was described well by a linear function. Therefore the total background PDF is

$$\mathcal{P}_B = (\frac{1}{\Delta m} + s.(M - M_0))\frac{1}{N_B}\sum_j^l b_j B_i d\phi. \tag{5.21}$$

Here, Δm is the width of the $KK\pi\pi$ mass window used in the fit (which is assumed to be centered around M_0) and s is the slope of the assumed linear distribution.

5.2.4 Final form of the Likelihood function

It is more convenient to maximize $\ln \mathcal{L}$ instead of $\mathcal{L}$ in the fit as multiplication over events becomes a sum over events which prevents too big (or small) numerical values.

$$-\ln \mathcal{L} = -\sum_{data\ events} \ln(\frac{S \cdot \mathcal{P}_{iS} + B \cdot \mathcal{P}_{iB})}{S + B}) - n \ln \nu - \nu + \ln n \tag{5.22}$$

The functions ϵ and $d\phi$ do not depend on the parameterization of the signal and background probabilities, so can be factored out before the minimization. Thus, defining $\mathcal{P}_S = \epsilon P_S$ and $\mathcal{P}_{iB} = \epsilon P_{iB}$,

$$-\ln \mathcal{L} = -\sum_{data\ events} \ln(\frac{S \cdot P_S + B \cdot P_{iB})}{S + B}) - n \ln \nu - \nu \sum_{data\ events} \ln \epsilon d\phi + \ln n \tag{5.23}$$

The term $\ln \epsilon(\phi) d\phi + \ln n$ is a constant for a particular data sample and can be ignored in the minimization of $-\ln \mathcal{L}$. In the minimization process, parameters S, B, A_i, α_i, b_i (and any other parameters used to model the decay) are varied to find the best possible set of parameters which describes the data according to the physical model of the decay assumed.

5.2.5 Evaluation of integrals

Phase space integrals can be numerically calculated (up to a constant factor) by summing over a large number of phase space Monte Carlo events generated according to the four body decay. So the normalization condition becomes

$$\sum_{MC\ events\ generated} S_j S_j^* = 1 \tag{5.24}$$

$$\sum_{MC\ events\ generated} B_j = 1 \tag{5.25}$$

E_{jk} are also calculated using phase space Monte Carlo events.

$$E_{jk} = \sum_{MC\ events\ generated} \epsilon S_j S_k^* \tag{5.26}$$

$$= \sum_{MC\ events\ accepted} S_j S_k^* \tag{5.27}$$

Thus the terms $d\phi$ and $\epsilon(\phi)$ never explicitly need to be evaluated, they are entirely taken in to account by Monte Carlo.

5.2.6 Normalized Physical Fractions

After finding the set of parameters which maximize the probability distribution function for a given data sample, the parameters A_i can be uncertain up to a common scale factor. So they have to be normalized to get the actual physical fractions.
Since the sum of the signal probability distribution function over all available states should be unity, it implies that before acceptance effects,

$$\int \mathcal{P}_S d\phi = 1 \tag{5.28}$$

where

$$\mathcal{P}_S = \frac{1}{N_P} |\sum_{j=1}^{m} A_j e^{i\alpha_j} S_j|^2 d\phi. \tag{5.29}$$

This requires the normalization,

$$N_P = \sum_{j=1}^{m} \sum_{k=1}^{m} A_j A_k \mathcal{R}e(e^{i(\alpha_j - \alpha_k)} N_{jk}) \tag{5.30}$$

where

$$N_{jk} = \int_{phase\ space} S_j S_k^* d\phi \tag{5.31}$$

since in evaluating integrals, phase space was assumed to be represented by the Monte Carlo sample used to calculate the integrals. Numerically,

$$N_P = \sum_{MC\ events\ generated} S_j S_k^*. \tag{5.32}$$

The physical fractions f_i are then given by

$$f_j = \frac{A_j^2}{N_p}. \tag{5.33}$$

The error on N_P is given by

$$(\text{Error N}_\text{P})^2 = \sum_{i.j} \frac{\partial N_P}{\partial x_i} \frac{\partial N_P}{\partial x_j} Var(x_i, x_j) \tag{5.34}$$

where x_i includes A_i and α_i and $Var(x_i, x_j)$ is the error matrix of x_i.

Evaluating the derivatives,

$$\frac{\partial N_p}{\partial A_k} = \sum_j A_j \mathcal{R}e(e^{i(\alpha_j - \alpha_k)} N_{jk}) \tag{5.35}$$

$$\frac{\partial N_p}{\partial \alpha_k} = -2\sum_j A_k A_j \mathcal{I}m(e^{i(\alpha_k-\alpha_j)}N_{kj}) \tag{5.36}$$

5.2.7 Fraction of Subset

The total contribution from a subset of decay modes is given by the coherent sum of amplitudes.

$$\sum_{i=1}^{subset}\sum_{j=1}^{subset} A_i A_j \mathcal{R}e(e^{i(\alpha_i-\alpha_j)}N_{ij}) \tag{5.37}$$

The error on the above sum is also given by equations 5.29-5.31, except that the sum is only taken over the modes involved.

5.2.8 Signal Matrix Elements

Signal elements S_i are usually written in terms of a Breit-Wigner, momentum dependant partial width, form factors, and an angular distribution function [4] [5].

5.2.8.1 Breit-Wigners :

The relativistic Breit-Wigner [28]

$$\frac{\sqrt{,}}{m^2 - m_0^2 + im_0, {}_0} \tag{5.38}$$

is used for each resonant state. $, {}_0$ is the total width of the resonanance and $,$ is the partial width of the decay which is assumed to have the following p dependance [27]

$$, \ \propto p^{2L}. \tag{5.39}$$

Here, p is the momentum of the decay particles in the parent rest frame and L is the orbital angular momentum of decay products.

5.2.8.2 Form Factors :

The Blatt and Weisskoff form factors [29], defined for two body decays of a resonance with spin L to be

$$F = 1 \tag{5.40}$$

for $L = 0$ and

$$F = \frac{1}{\sqrt{1 + R^2 p^2)}} \tag{5.41}$$

for $L = 1$,

are used for each decay vertex. R represents the meson radius in this model. Typical values used by others are 5 GeV^{-1} for D^0 and 3 GeV^{-1} for ρ, ϕ, K^* s [4]).

5.2.8.3 Angular Distributions :

Each decay has a characteristic angular distribution which depends on the spins and angular momenta of the decay particles. For example, a non-resonant decay of a pseudoscalar particle into pseudoscalars is isotropic in space and the angular distribution is uniform. In the case of pseudoscalar decay into two vectors [31] (*eg.* $D^0 \to K^{*0}\overline{K^{*0}} \to K^+K^-\pi^+\pi^-$), there are three helicity states for the resonant vector

states, $\mathcal{A}_{11}$, $\mathcal{A}_{-1-1}$, and $\mathcal{A}_{00}$ (where subscripts denote the helicity of each resonance). The transverse amplitude is defined as

$$\mathcal{A}_T = \mathcal{A}_{11} + \mathcal{A}_{-1-1} \tag{5.42}$$

$$= \sin\theta_1 \sin\theta_2 \cos\phi. \tag{5.43}$$

The longitudinal amplitude is defined as,

$$\mathcal{A}_L = \mathcal{A}_{00} \tag{5.44}$$

$$= \cos\theta_1 \cos\theta_2 \tag{5.45}$$

Here, θ_1 and θ_2 are the helicity angles which are defined as the angles of the vector decay products measured in the vector rest frame relative to the direction of the D^0. ϕ is the angle between two vector decay planes.

The remaining $l = 1$ amplitude in this formalism is [31]

$$\mathcal{A}_{l=1} = \mathcal{A}_{1,1} - \mathcal{A}_{-1,-1} \tag{5.46}$$

$$= \sin\theta_1 \sin\theta_2 \sin\phi \tag{5.47}$$

Generally, there is a particular angular distribution for each angular momentum state of the decay. Therefore, for decays with a large number of possible helicity states (eg.$D \rightarrow VP_1P_2$ has nine helicity states), the description of the complete angular distribution is complicated.

5.2.9 Background Amplitudes

The background amplitude for the random background, which has no structure, is a constant (=1). The typical resonant background term has the form of a Breit-Wigner multiplied by a form factor:

$$B_i = \frac{p_i^2}{({m_i}^2 - {m_{i0}}^2)^2 + ,\ {}_i{}^2 {m_{i0}}^2} . \frac{1}{1 + r^2 {p_i}^2} \tag{5.48}$$

where p_i is the decay momentum in the resonant rest frame.

5.3 Fit to $D^0 \to K^+K^-\pi^+\pi^-$

5.3.1 Selection of Decay Modes

There are large number of possible decay modes which contribute to the the resonant structure of $D^0 \to K^+K^-\pi^+\pi^-$. Each decay mode may have several angular momentum states. Given our statistics, it is not practical to perform fits that include all possible decay modes simultaneously. Some simplifying assumptions had to be made to make the fit practically possible.

Inclusion of angular distributions and momentum dependent form factors and widths would have required a large number of amplitudes for certain decays (eg. $D^0 \to \phi\rho$ has three possible helicity states, $D^0 \to K^{*0}K^-\pi^+$ has nine). Therefore, the signal amplitudes were modeled only with a Breit-Wigner. As shown in the Appendix A, ignoring the form factors and the p^{2L} factor does not make a significant difference. However ignoring the angular distributions reduces the ability of the fit to distinguish different decay modes.

There is an ambiguity for the decay modes $D^0 \to K^{*0}K^+\pi^-$. Both $D^0 \to K^{*0}K^-\pi^+$ and $D^0 \to \overline{K^{*0}}K^+\pi^-$ are allowed, and both D^0 and $\overline{D^0}$ are present in the data sample. It is not possible to distinguish these two modes without D^0, $\overline{D^0}$ identification. Although D^0 and $\overline{D^0}$ can be identified using the D^{*+} tag, as shown in the Figure 5.8, there are not enough $D^{*\pm}$ events in the event sample to distinguish $D^0 \to K^{*0}(892)K^-\pi^+$ from $D^0 \to \overline{K^{*0}}(892)K^+\pi^-$

5.3.2 Signal and Background PDFs

As explained earlier, the following signal and background PDFs were used in the fit:

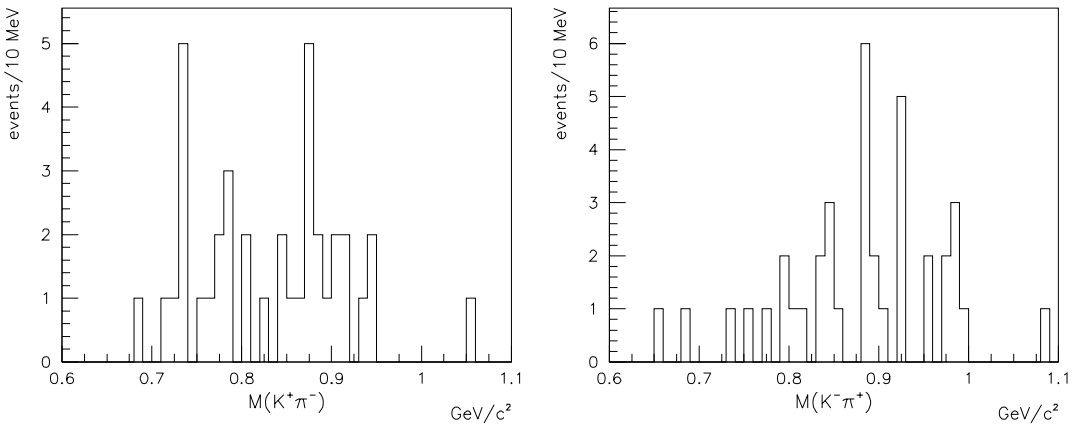

Figure 5.8: $K\pi$ mass distributions for events in the D^0 signal region with D^{*+} tag used to identify (a) $D^0 \to K^{*0}K^-\pi^+$ + c.c. and (b) $D^0 \to \overline{K^{*0}}K^+\pi^-$ + c.c. modes

1	$D^0 \to KK\pi\pi$ non resonant
2	$D^0 \to K^{*0}(892)K^{*0}(892)\overline{K^{*0}(892)}$, $K^{*0}(892) \to K^+\pi-$
3	$D^0 \to K^{*0}(892)K^-\pi^+$, $K^{*0}(892) \to K^+\pi-$
4	$D^0 \to \overline{K^{*0}(892)}K^+\pi^-$, $\overline{K^{*0}(892)} \to K^-\pi^+$
5	$D^0 \to \rho\phi$, $\rho \to \pi^+\pi^-$, $\phi \to K^+K^-$
6	$D^0 \to \rho K^+K^-$, $\rho \to \pi^+\pi^-$
7	$D^0 \to \phi\pi^+\pi^-$, $\phi \to K^+K^-$
8	$D^0 \to K_1^-(1270)K^+$, $K_1^-(1270) \to K^-\rho$, $\rho \to \pi^+\pi^-$
9	$D^0 \to K_1^+(1270)K^-$, $K_1^+(1270) \to K^+\rho$, $\rho \to \pi^+\pi^-$
10	$D^0 \to K^-(1400)K^+$, $K^-(1400) \to \overline{K^{*0}(892)}\pi^-$, $\overline{K^{*0}(892)} \to K^-\pi^+$
11	$D^0 \to K^+(1400)K^-$, $K^+(1400) \to K^{*0}(892)\pi^-$, $K^{*0}(892) \to K^+\pi^-$

Table 5.2: Decay modes selected for the fit

$$\mathcal{P}_S = \frac{1}{\sqrt{2\pi}\sigma} \exp\left(\frac{-(M_i - M_0)^2}{2\sigma^2}\right) . \frac{1}{N_S} \sum_{j=1}^{m} \sum_{k=1}^{m} A_i A_j \mathcal{R}e(e^{i(\alpha_j - \alpha_k)} S_j S_k^*) \tag{5.49}$$

where the signal amplitudes were approximated by a product of Breit-Wigners,

$$S_i = \frac{1}{\sqrt{N_i}} \prod_l^k \cdot \frac{1}{m_{il}^2 - m_{il0}^2 + i m_{il0},\ _{il0}}, \tag{5.50}$$

where k is the number of resonances in the decay mode and N_i is the normalization which is defined by Eq. 5.7 (numerically by Eq. 5.24);

$$\mathcal{P}_B = \left(\frac{1}{\Delta m} + s.(M_i - M_0)\right) \cdot \frac{1}{N_B}(b_1.B_1 + b_2 B_2 + ...b_m B_m). \tag{5.51}$$

Background resonances were also approximated by Breit-Wigners:

$$B_i = \frac{1}{K_i} \cdot \frac{1}{(m_i{}^2 - m_{i0}{}^2)^2 + ,\ _i{}^2 m_{i0}{}^2}. \tag{5.52}$$

K_i is the normalization which was defined by Eq. 5.18 (numerically by Eq. 5.25).

The decay modes chosen for the fit as candidates for $D^0 \rightarrow K^+K^-\pi^+\pi^-$ are shown in Table 5.2. A random distribution and resonances ϕ, $K^{*0}(892)$, ρ and K_s were included in the background.

5.3.3 The Fitting Process

The normalization and other phase space integrals in the fit were calculated using Monte Carlo events generated according to $D^0 \rightarrow K^+K^-\pi^+\pi^-$ phase space. The coefficients E_{ij} were calculated using phase space Monte Carlo events which were reconstructed and passed all the analysis cuts. Since none of the signal amplitudes had any dependence on fit parameters, they were calculated only once at the beginning

of the fit. To respect the kinematcal boundaries, decay tracks (in data) were refitted to constrain their total invariant mass to be the D^0 mass. These constrained track parameters were used in calculating signal amplitudes S_i. Unconstrained parameters were used to calculate background amplitudes B_i.

Maximum likelihood fitting was done using the MINUIT [26] function minimization and error analysis software. The following form of the loglikelihood function was minimized

$$\mathcal{M} = -2 \cdot \ln \mathcal{L}$$

where the factor of -2 was introduced so that the parabolic errors given by MINUIT could be interpreted correctly (*ie.* correspond to changes in χ^2 for Gaussian distributions.)

The signal amplitudes (A_i); relative phase angles (α_i); number of estimated D^0 events (S); D^0 mass and width (m_0 and σ); an estimate of number of background events in the sample (BG); the slope of the assumed linear background distribution (s); and the background probabilities (B_i) were included as the parameters in the fit. The parameters m_0, σ, and s were held constant after they were determined from one fit. Since amplitudes and phases are only relative quantities, for each fit a signal amplitude, a phase, and a background amplitude were kept constant. (Since there was a clear indication for significant $D^0 \to \phi\rho$ decay, that amplitude and phase were chosen to be held constant).

Since $K_1^+(1400)$ decays into $K^{*0}(892)\pi^+$, except for the very broad $K_1^+(1400)$ Breit-Wigner, $K^{*0}(892)K^+\pi^-$ and $K_1^+(1400)K^-$ have identical two and three-body invariant mass distributions. Fits with both of these amplitudes failed to produce an improved fit. Instead, the fractions for each of these two amplitudes become large and highly uncertain. This occurs because the relative phases for these amplitudes adjust so that the two amplitudes interfere destructively to an extent that depends

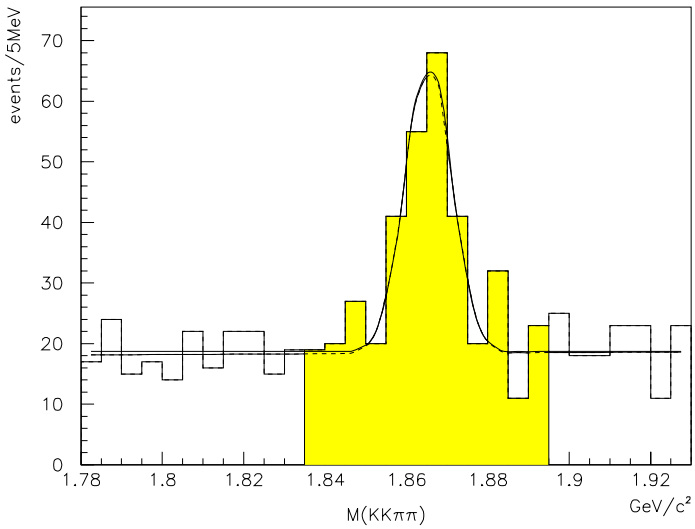

Figure 5.9: Fit projection on $KK\pi\pi$ mass distribution. Events in the shaded region were used in the fit.

sensitively on the conditions of each particular fit, making the systematic effects large and highly uncertain. Therefore, fits with such similar decay modes did not provide any additional information.

The fits were done with the events in the mass window $|M(KK\pi\pi - 1.865| < 0.030$ GeV (Figure 5.9). A number of fits were performed with different combinations of decay modes allowed in the fit. To assure that each fit converged to a true minimum, not to a local minimum, in each case a number of fits (at least five) were done with different starting values for the parameters. From the fit results, normalized physical fractions (f_i) were calculated (as explained in 5.2.6), which were used to compare results from different fits.

5.3.4 Projections from the Fit

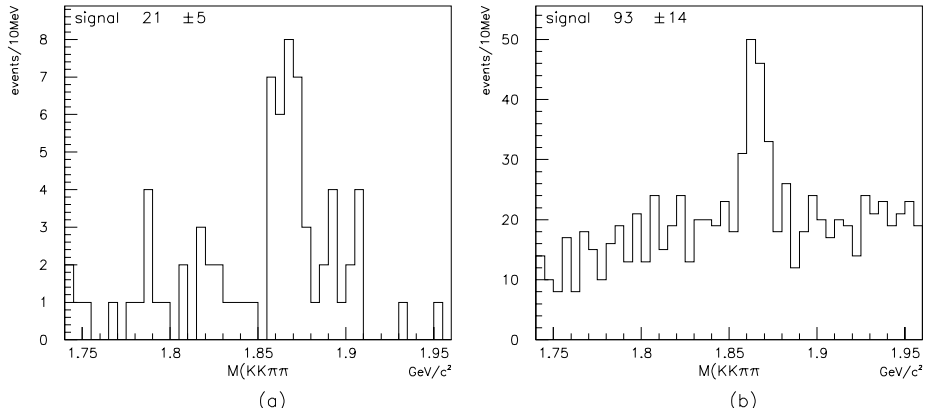

Figure 5.10: Events pass the ϕ mass cut $|M(K^+K^)-1.02| < 0.006$ (left) , events did not pass the ϕ mass cut (right).

Fit projections were made by filling the histograms with $D^0 \to KK\pi\pi$ phase space Monte Carlo events which passed the analysis cuts (there were 17,000 such events) weighted by the probability distribution function $\mathcal{P}_S$ (Eq. 5.3). The resulting distributions were then normalized to the corresponding distributions from data. Figures 5.11 and 5.12 show projections for signal region and background region events using the fit 1 results in table 5.3. Fit projections have reproduced all the features within errors and are in good agreement with data. However, due to the limited statistics of the data sample, the χ^2 per degree of freedom [1] of the the projections was not an indication of the goodness of one fit compared to another. Generally, all fits gave equally good projections.

5.3.5 Total ϕ signal

[1]The contribution to χ^2 from each bin was calculated using the square root of the predicted number of events as the expected error. χ^2 per degree of freedom was calculated as the sum of χ^2s of individual bins divided by the total number of bins in the histogram.

There is a significant ϕ signal from D^0 which can be seen in Figure 5.4(c). The ϕ signal was estimated by applying a ± 6 MeV mass cut around the ϕ peak at 1.020 GeV. Figure 5.10 shows the D^0 signal within and outside this mass cut. From the results on Figure 5.10, the fraction of the signal with ϕ was calculated to be 0.184 ± 0.054 (This estimate ignores the background events under the ϕ signal and assumed the mass cut was 100% efficient. Due to the narrow width of the ϕ these assumtions do not introduce any significant systamatic error). This value was compared with the physical fraction of the sum of the modes $D^0 \to \phi\rho$ and $D^0 \to \phi\pi^+\pi^-$ from fit results, as another consistency check of the fit.

5.3.6 Interpretation of Fit Results

Results from a number of fits are shown in Table 5.4-5.6. In addition to amplitudes and phases of the decays, normalized fractions, values of the likelihood functions and the fractions of the D^0 events which decay into ϕs estimated from the fits (sum of $\phi\rho$ and $\phi\pi\pi$, as explained in section 5.2.7) are shown.

Due to the limited statistics available,the fits did not give statistically significant estimates for many modes. Large numbers of possible decay modes and interferences and enhancements among them make definite conclusions from fit results difficult.

The first fit (fit 1) had all the modes selected for the analysis (shown in Table 5.2) except modes involving $K_1(1270)$ and $K^*(1400)$. The only difference in the fit between the $K_1(1270)$ modes and the $\rho\pi\pi$ mode is the (wide) Breit-Wigner of $K(1270)$. As mentioned before, differences between the modes $K(1400)$ and $K^{*0}K\pi$ are not significant. So this was the reasonable minimum number of modes to start with. Subsequent fits were done by excluding and including different modes to fit 1.

Fit 1 finds a large non-resonant and ρKK contribution with large errors. This may be just an interference effect because the only difference between them is the broad Breit-Wigner of the ρ. Fits done forcing ρKK and non-resonant contributions to zero (fit4 and fit5) indicate that ρKK is more likely than a non-resonant mode. Figure 5.1 also gives some indications of ρ not associated with $\phi\rho$.

ρKK can be either a direct three body decay of D^0 or may be resulting from $K_1(1270)K$. Adding $K_1(1270)K$ to the fit with both non-resonant and ρKK shows clear interference effects. (f_4 and f_8 are large). With $K_1(1270)K$ in the fit, fits 9, 11, and 12 indicate that all ρKK is consistent with coming from $K_1(1270)K$. When both ρKK and and non-resonant amplitudes forced to zero, it still gave a good fit (fit 12), indicating that both non-resonant and ρKK could be explained by $K_1(1270)K$. Since none of the modes are significant enough for a definite conclusion, no quantitative

```
FCN=   4690.736  FROM MIGRAD  STATUS=CONVERGED   3365 CALLS  3368 TOTAL
      EDM=  0.34E-06  STRATEGY=1  ERROR MATRIX UNCERTAINTY=  1.2%
```

EXT NO.	PARAMETER NAME	VALUE	ERROR	STEP SIZE	FIRST DERIVATIVE
1	signal	120.01	12.873	-0.19511E-02	0.31686E-04
2	mass	1.8650	constant		
3	sigma	0.53000E-02	constant		
4	BG	244.99	18.630	0.23001E-01	-0.24162E-04
5	bs	2.0600	constant		
6	A1 non res	1.9069	0.87751	-0.18340E-03	-0.89323E-03
7	A2 phi rho	1.0000	constant		
8	A3 phi 2pi	0.84574	0.23115	-0.11733E-04	0.17580E-02
9	A4 rho 2K	1.77752	0.86931	0.39305E-03	-0.85857E-03
10	A5 K*0K*0~	0.80211	0.41350	-0.33973E-04	-0.82252E-03
11	A6 K*0Kpi	0.49300	0.53886	0.49524E-03	-0.15450E-02
12	A7 K*0~Kpi	0.29432	0.39622	0.26847E-03	-0.11064E-02
13	A10 K*(127	0.10000	constant		
14	A10 K*~(12	0.00000E+00	constant		
15	A8 K*(1400	0.10000	constant		
16	A9 K*~(140	0.00000E+00	constant		
17	alpha1	1.6599	0.43439	0.25583E-03	-0.13100E-02
18	alpha2	0.00000E+00	constant		
19	alpha3	3.192591	0.48472	-0.14417E-03	0.49479E-03
20	alpha4	-1.5882	0.45065	0.35410E-03	0.14420E-02
21	alpha5	-1.2285	0.53414	0.62211E-03	0.87635E-03
22	alpha6	-3.0771	0.75647	0.41371E-03	-0.38633E-03
23	alpha7	0.84359	1.2223	0.17343E-02	-0.16769E-03
24	alpha8	0.00000E+00	constant		
25	alpha9	0.00000E+00	constant		
26	alpha10	0.00000E+00	constant		
27	alpha11	0.00000E+00	constant		
28	B1(rand)	1.0000	constant		
29	B2(K*0)	0.10142	0.80549E-01	-0.11783E-04	0.65543E-03
30	B3(K*0~)	0.21759E-10	0.41242E-01	-0.19936E-04	0.13469E-04
31	B4(phi)	0.47534E-01	0.27663E-01	-0.13789E-04	0.14131E-01
32	B5(K_s)	0.56004E-01	0.32636E-01	-0.15175E-04	0.44300E-03
33	B6(rho)	0.30788E-07	0.83753E-01	0.19103E-05	0.20364E-05

Table 5.3: A typical Fit result from MINUIT

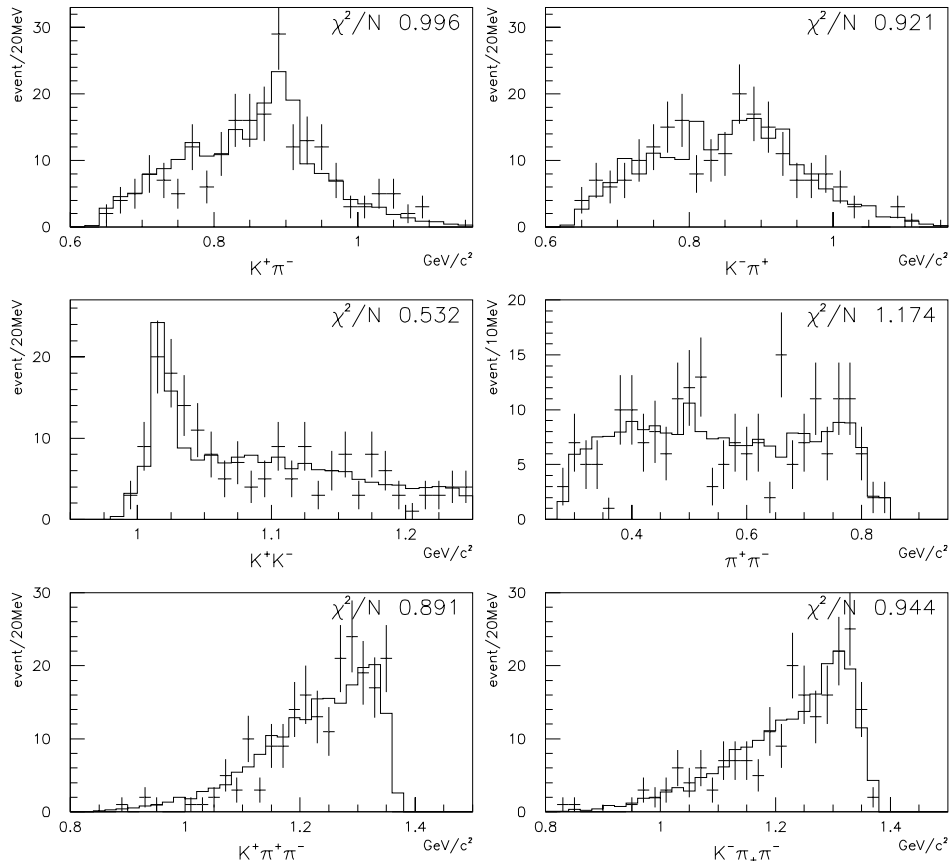

Figure 5.11: Fit projections for events in the D^0 signal region ($|M(KK\pi\pi) - 1.865| < 0.012$) for the fit 1 results in table 5.3 (Data is indicated by points with error bars and the fit projection by the curve)

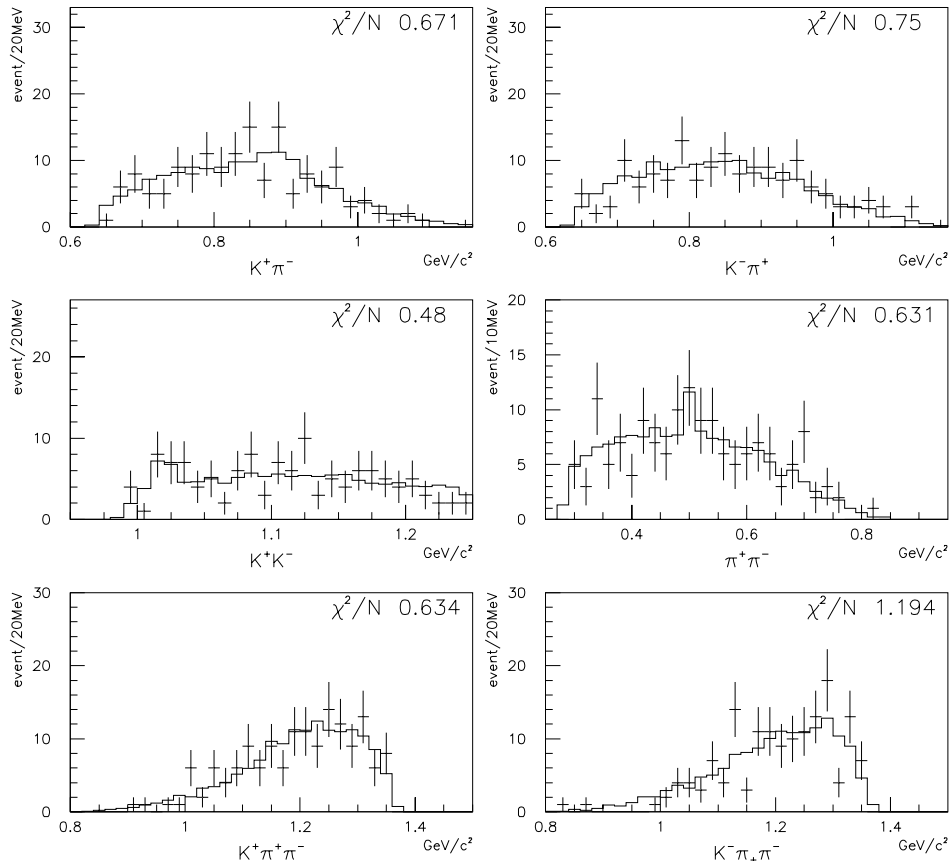

Figure 5.12: Fit projection for events in the background region ($0.03 > |M(KK\pi\pi) - 1.865| > 0.012$) for the fit 1 results in table 5.3 (Data is indicated by points with error bars and the fit projection by the curve)

parameter	fit 1	fit 2	fit 3	fit 4	fit 5
A_1, non-res.	1.89 ± 0.78	1.54 ± 0.78	1.39 ± 0.55	0.00	0.51 ± 0.22
A_2, $\phi\rho$	1.00	1.00	1.00	1.00	1.00
A_3,$\phi\pi\pi$	0.85 ± 0.17	0.89 ± 0.21	0.00	0.99 ± 0.18	0.66 ± 0.10
A_4,ρK^+K^-	1.74 ± 0.64	1.40 ± 0.69	2.13 ± 0.45	1.21 ± 0.45	0.00
A_5, $K^{*0}\overline{K^{*0}}$	0.77 ± 0.34	0.76 ± 0.30	0.52 ± 0.27	1.05 ± 0.33	0.66 ± 0.16
A_6,$K^{*0}K\pi$	0.37 ± 0.43	0.00	1.26 ± 0.34	0.74 ± 0.35	0.55 ± 0.19
A_7,$\overline{K^{*0}}K\pi$	0.27 ± 0.34	0.00	0.37 ± 0.35	0.12 ± 0.21	0.03 ± 0.16
A_8,$K^{*+}(1270)$	0.00	0.00	0.00	0.00	0.00
A_9,$K^{*-}(1270)$	0.00	0.00	0.00	0.00	0.00
A_{10},$K^{*+}(1410)$	0.00	0.00	0.00	0.00	0.00
A_{11},$K^{*-}(1410)$	0.00	0.00	0.00	0.00	0.00
α_1, non-res.	1.71 ± 0.41	1.69 ± 0.40	1.48 ± 0.53	0.00	1.78 ± 0.51
α_2, $\phi\rho$	0.00	0.00	0.00	0.00	0.00
α_3, $\phi\pi\pi$	3.16 ± 0.33	-3.23 ± 0.36	0.00	2.99 ± 0.30	-3.77 ± 0.21
α_4, ρK^+K^-	4.74 ± 0.41	-1.72 ± 0.46	-0.97 ± 0.37	-2.44 ± 0.43	0.00
α_5, $K^{*0}\overline{K^{*0}}$	-1.32 ± 0.49	-1.35 ± 0.51	-0.99 ± 0.78	-1.15 ± 0.48	-2.39 ± 0.38
α_6, $K^{*0}K\pi$	3.25 ± 0.93	0.00	-2.78 ± 0.41	0.96 ± 0.57	-0.44 ± 0.42
α_7, $\overline{K^{*0}}K\pi$	0.74 ± 1.03	0.00	0.19 ± 0.89	2.30 ± 2.12	1.72 ± 5.89
α_8, $K^{*+}(1270)$	0.00	0.00	0.00	0.00	0.00
α_9, $K^{*-}(1270)$	0.00	0.00	0.00	0.00	0.00
α_{10}, $K^{*+}(1410)$	0.00	0.00	0.00	0.00	0.00
α_{11},$K^{*-}(1410)$	0.00	0.00	0.00	0.00	0.00
f_1, non-res	0.69 ± 0.57	0.55 ± 0.56	0.41 ± 0.32	0.00	0.24 ± 0.21
f_2, $\phi\rho$	0.19	0.23	0.21	0.31	0.95
f_3, $\phi\pi\pi$	0.14 ± 0.06	0.18 ± 0.09	0.00	0.30 ± 0.11	0.41 ± 0.13
f_4, ρK^+K^-	0.59 ± 0.43	0.45 ± 0.45	0.96 ± 0.40	0.45 ± 0.33	0.00
f_5, $K^{*0}\overline{K^{*0}}$	0.11 ± 0.10	0.13 ± 0.10	0.06 ± 0.06	0.33 ± 0.21	0.42 ± 0.20
f_6, $K^{*0}K\pi$	0.03 ± 0.06	0.00	0.33 ± 0.18	0.17 ± 0.16	0.28 ± 0.19
f_7, $\overline{K^{*0}}K\pi$	0.02 ± 0.04	0.00	0.03 ± 0.05	0.00 ± 0.02	0.00 ± 0.01
f_8, $K^{*+}(1270)$	0.00	0.00	0.00	0.00	0.00
f_9, $K^{*-}(1270)$	0.00	0.00	0.00	0.00	0.00
f_{10}, $K^{*+}(1410)$	0.00	0.00	0.00	0.00	0.00
f_{11}, $K^{*-}(1410)$	0.00	0.00	0.00	0.00	0.00
$\frac{\phi}{total}$	0.17 ± 0.05	0.19 ± 0.052	0.21 ± 0.054	0.25 ± 0.091	0.44 ± 0.14
$-2 \ln \mathcal{L}$	4690.264	4689.693	4689.693	4693.357	4697.685

Table 5.4: Fit results for different fits. Amplitudes (A_i), phases(α_i), and normalized fractions (f_i) are shown. Values without errors were fixed during the fit at that value. Errors on f_i do include the error on N_P.

parameter	fit 6	fit 7	fit 8	fit 9	fit 10
A_1, non res	0.54 ± 0.13	0.76 ± 0.14	1.54 ± 1.09	2.04 ± 1.22	1.89 ± 0.65
A_2, $\phi\rho$	1.00	1.00	1.00	1.00	1.00
A_3, $\phi\pi\pi$	0.62 ± 0.12	0.68 ± 0.13	1.09 ± 0.45	0.92 ± 0.67	0.85 ± 0.21
A_4,ρK^+K^-	0.00	0.00	4.58 ± 2.58	0.00	1.74 ± 0.63
A_5, $K^{*0}\overline{K^{*0}}$	0.41 ± 0.09	0.00	0.68 ± 0.46	0.78 ± 0.46	0.80 ± 0.34
A_6, $K^{*0}K\pi$	0.00	0.00	1.73 ± 0.80	1.84 ± 0.66	0.00
A_7,$\overline{K^{*0}}K\pi$	0.00	0.00	0.41 ± 0.51	0.43 ± 0.49	0.00
A_8,$K^{*+}(1270)$	0.00	0.00	3.48 ± 1.71	2.49 ± 1.19	0.00
A_9,$K^{*-}(1270)$	0.00	0.00	2.05 ± 1.50	1.05 ± 0.69	0.00
A_{10}, $K^{*+}(1410)$	0.00	0.00	0.00	0.00	0.35 ± 0.46
A_{11},$K^{*-}(1410)$	0.00	0.00	0.00	0.00	0.29 ± 0.32
α_1, non res.	1.42 ± 0.53	1.09 ± 0.71	0.91 ± 0.71	1.23 ± 0.71	1.71 ± 0.36
α_2, $\phi\rho$	0.00	0.00	0.00	0.00	0.00
α_3, $\phi\pi\pi$	2.56 ± 0.24	2.67 ± 0.26	3.62 ± 0.65	-2.19 ± 0.95	3.16 ± 0.31
α_4, ,ρK^+K^-	0.00	0.00	-0.05 ± 0.61	0.00 ± 1.41	4.74 ± 0.40
α_5, $K^{*0}\overline{K^{*0}}$	-2.43 ± 0.48	0.00	-1.98 ± 0.94	-1.51 ± 0.93	-1.25 ± 0.48
α_6, $K^{*0}K\pi$	0.00	0.00	-3.50 ± 0.60	-3.27 ± 0.72	0.00
α_7, $\overline{K^{*0}}K\pi$	0.00	0.00	-0.96 ± 1.37	-0.29 ± 1.32	0.00
α_8, $K^{*+}(1270)$	0.00	0.00	-2.43 ± 0.67	-1.22 ± 0.83	0.00
α_9, $K^{*-}(1270)$	0.00	0.00	-2.52 ± 0.92	-1.24 ± 0.84	0.00
α_{10}, $K^{*+}(1410)$	0.00	0.00	0.00	0.00	3.47 ± 1.06
α_{11}, $K^{*-}(1410)$	0.00	0.00	0.00	0.00	1.07 ± 0.90
f_1, non res	0.26 ± 0.13	0.53 ± 0.19	0.27 ± 0.38	0.38 ± 0.45	0.70 ± 0.48
f_2, $\phi\rho$	0.90	0.91	0.11	0.09	0.19
f_3, $\phi\pi\pi$	0.35 ± 0.13	0.42 ± 0.16	0.13 ± 0.11	0.08 ± 0.11	0.14 ± 0.07
f_4,ρK^+K^-	0.00	0.00	2.37 ± 2.67	0.00	0.59 ± 0.43
f_5, $K^{*0}\overline{K^{*0}}$	0.15 ± 0.07	0.00	0.05 ± 0.07	0.05 ± 0.06	0.12 ± 0.10
f_6, $K^{*0}K\pi$	0.00	0.00	0.34 ± 0.31	0.31 ± 0.22	0.00
f_7,$\overline{K^{*0}}K\pi$	0.00	0.00	0.02 ± 0.05	0.02 ± 0.04	0.00
f_8,$K^{*+}(1270)$	0.00	0.00	1.37 ± 1.34	0.57 ± 0.54	0.00
f_9,$K^{*-}(1270)$	0.00	0.00	0.47 ± 0.69	0.10 ± 0.13	0.00
f_{10}, $K^{*+}(1410)$	0.00	0.00	0.00	0.00	0.04 ± 0.06
f_{11}, $K^{*-}(1410)$	0.00	0.00	0.00	0.00	0.02 ± 0.06
$\frac{\phi}{total}$	0.43 ± 0.21	0.46 ± 0.22	0.20 ± 0.081	0.20 ± 0.11	0.17 ± 0.05
$-2\ln\mathcal{L}$	4692.385	4724.552	4682.321	4684.765	4690.461

Table 5.5: Continuation of Table 5.4

parameter	fit11	fit12	fit13	fit14	fit15
A_1, non res	0.00	0.00	1.62 ± 1.15	1.89 ± 0.82	1.74 ± 0.85
A_2, $\phi\rho$	1.00	1.00	1.00	1.01 ± 0.23	1.12 ± 0.26
A_3, $\phi\pi\pi$	0.96 ± 0.18	0.98 ± 0.18	0.93 ± 0.89	0.85	1.00
A_4, ρK^+K^-	1.25 ± 1.31	0.00	3.10 ± 1.34	1.76 ± 0.74	1.61 ± 0.72
A_5, $K^{*0}\overline{K^{*0}}$	1.01 ± 0.31	0.94 ± 0.31	0.00	0.80 ± 0.39	0.86 ± 0.32
A_6, $K^{*0}K\pi$	0.69 ± 0.32	0.57 ± 0.31	2.19 ± 0.77	0.38 ± 0.36	0.00
A_7, $\overline{K^{*0}}K\pi$	0.17 ± 0.24	0.17 ± 0.26	0.53 ± 0.49	0.30 ± 0.34	0.00
A_8, $K^{*+}(1270)$	0.82 ± 0.75	0.62 ± 0.45	0.00	0.00	0.00
A_9, $K^{*-}(1270)$	0.49 ± 0.40	0.75 ± 0.46	0.00	0.00	0.00
A_{10}, $K^{*+}(1410)$	0.00	0.00	0.00	0.00	0.00
A_{11}, $K^{*-}(1410)$	0.00	0.00	0.00	0.00	0.00
α_1, non res.	0.00	0.00	1.09 ± 0.8	1.70 ± 0.20	4.88 ± 0.47
α_2, $\phi\rho$	0.00	0.00	0.00	0.00 ± 0.25	3.21 ± 0.36
α_3, $\phi\pi\pi$	3.03 ± 0.31	2.98 ± 0.29	4.18 ± 1.25	3.16	0.00
α_4, ρK^+K^-	3.49 ± 0.49	0.00	4.96 ± 0.73	4.74 ± 0.23	1.48 ± 0.48
α_5, $K^{*0}\overline{K^{*0}}$	-1.26 ± 0.48	-1.34 ± 0.50	0.00	-1.25 ± 0.38	1.86 ± 0.54
α_6, $K^{*0}K\pi$	0.76 ± 0.61	0.82 ± 0.72	3.05 ± 0.84	3.24 ± 0.71	0.00
α_7, $\overline{K^{*0}}K\pi$	2.42 ± 1.42	2.59 ± 1.29	4.34 ± 1.18	0.82 ± 0.71	0.00
α_8, $K^{*+}(1270)$	-0.48 ± 1.04	10.79 ± 0.82	0.00	0.00	0.00
α_9, $K^{*-}(1270)$	2.66 ± 1.47	3.45 ± 0.86	0.00	0.00	0.00
α_{10}, $K^{*+}(1410)$	0.00	0.00	0.00	0.00	0.00
α_{11}, $K^{*-}(1410)$	0.00	0.00	0.00	0.00	0.00
f_1, non res	0.00	0.00	0.25 ± 0.36	0.68 ± 0.60	0.54 ± 0.53
f_2, $\phi\rho$	0.31	0.32	0.10	0.19 ± 0.09	0.23 ± 0.11
f_3,$\phi\pi\pi$	0.29 ± 0.11	0.30 ± 0.11	0.08 ± 0.16	0.14	0.18
f_4,ρK^+K^-	0.48 ± 1.01	0.00	0.93 ± 0.81	0.59 ± 0.50	0.47 ± 0.42
f_5, $K^{*0}\overline{K^{*0}}$	0.31 ± 0.19	0.28 ± 0.18	0.00	0.12 ± 0.12	0.13 ± 0.10
f_6,$K^{*0}K\pi$	0.15 ± 0.14	0.10 ± 0.11	0.47 ± 0.33	0.03 ± 0.05	0.00
f_7,$\overline{K^{*0}}K\pi$	0.01 ± 0.02	0.01 ± 0.03	0.03 ± 0.05	0.02 ± 0.04	0.00
f_8,$K^{*+}(1270)$	0.21 ± 0.38	0.12 ± 0.18	0.00	0.00	0.00
f_9,$K^{*-}(1270)$	0.07 ± 0.12	0.18 ± 0.22	0.00	0.00	0.00
f_{10} ,$K^{*+}(1410)$	0.00	0.00	0.00	0.00	0.00
f_{11} ,$K^{*-}(1410)$	0.00	0.00	0.00	0.00	0.00
$\frac{\phi}{total}$	0.26 ± 0.11	0.26 ± 0.11	0.22 ± 0.054	0.17 ± 0.051	0.19 ± 0.054
$-2\ln\mathcal{L}$	4691.80	4692.462	4690.368	4689.396	4691.750

Table 5.6: Continuation of Table 5.4

estimate was done for these modes.

Fit 1 finds a small (and statistically not very significant) $K^{*0}\overline{K^{*0}}$ fraction (0.11 ± 0.10). Fit 13 was made forcing this to zero and the log likelihood increased by only 0.1, indicating that it is consistent with zero. An upper limit for this decay was estimated based on fit 2 results.

Fit 1 finds negligible contributions from $K^{*0}K\pi$ modes. However since both $K^{*0}K\pi$ modes and $K(1400)K$ modes are similar (as can be seen in fit 10), there may be contributions hidden by interferences. When both $K^{*0}K\pi$ and $K(1400)K$ were included, the fit did not converge. So it was not possible to make any quantitative estimate for these modes.

Although fit 1 finds a somewhat significant $\phi\pi\pi$ contribution, fit 3 done forcing it to zero increased log likelihood only by 0.5 . So it may be just an interference effect with $\phi\rho$. An upper limit was estimated based on fit 2 results.

The mode $\phi\rho$ was predetermined to exist (Figure 5.3) and used as the reference in fits 1-13. The presence of $\phi\rho$ was confirmed in fit 14 and fit 15 where the $\phi\rho$ amplitude and phase were allowed to float.

The following quantitative estimates were make from the above observations.

decay mode	fit(s) used	fractional contribution	phase
ϕ+ X	1, 2	0.18 ± 0.051	
$\phi\rho$	14,15	0.21 ± 0.10	0
$\overline{K^{*0}}K^{*0}$	2	0.13 ± 0.10	1.35 ± 0.49

5.4 Systematic Errors:

Several sources of systematic uncertainties on the fit results were considered and estimated by performing many fits with different conditions.

	$K^{*0}(892)$		ρ		ϕ	
, MeV	52	48	145	157	5.8	6.2
A_1	0.87 ± 0.71	0.88 ± 0.70	0.81 ± 0.68	0.92 ± 0.62	0.97 ± 0.61	0.86 ± 0.61
A_2	0.16	0.16	0.17	0.15	0.16	0.16
A_3	0.11 ± 0.05	0.11 ± 0.07	0.10 ± 0.05	0.11 ± 0.06	0.08 ± 0.05	0.11 ± 0.07
A_4	0.74 ± 0.66	0.74 ± 0.60	0.70 ± 0.64	0.77 ± 0.64	1.05 ± 0.62	0.73 ± 0.58
A_5	0.10 ± 0.10	0.10 ± 0.09	0.11 ± 0.08	0.11 ± 0.11	0.09 ± 0.08	0.11 ± 0.06
A_6	0.04 ± 0.08	0.04 ± 0.06	0.04 ± 0.08	0.04 ± 0.08	0.20 ± 0.15	0.04 ± 0.06
A_7	0.02 ± 0.04	0.02 ± 0.04	0.02 ± 0.03	0.02 ± 0.04	0.05 ± 0.07	0.02 ± 0.03
α_1	1.72 ± 0.43	1.72 ± 0.41	1.75 ± 0.39	1.68 ± 0.39	1.69 ± 0.40	1.71 ± 0.40
α_2	0.0	0.0	0.0	0.0	0.0	0.00
α_3	3.27 ± 0.51	3.26 ± 0.39	3.31 ± 0.50	3.23 ± 0.45	1.76 ± 0.39	3.26 ± 0.46
α_4	-1.40 ± 0.44	4.88 ± 0.40	4.89 ± 0.41	4.88 ± 0.41	5.34 ± 0.38	4.87 ± 0.43
α_5	-1.21 ± 0.52	-1.26 ± 0.50	-1.12 ± 0.53	-1.19 ± 0.57	-0.31 ± 0.58	-1.17 ± 0.55
α_6	3.33 ± 0.81	-2.96 ± 0.82	3.37 ± 0.82	3.29 ± 0.83	4.16 ± 0.46	3.32 ± 0.84
α_7	0.73 ± 1.06	-2.96 ± 0.82	0.82 ± 0.98	0.76 ± 1.00	0.82 ± 0.76	0.79 ± 1.05
ϕ	0.16 ± 0.05	0.16 ± 0.05	0.16 ± 0.05	0.16 ± 0.05	0.16 ± 0.05	0.16 ± 0.05

Table 5.7: Variation of fit results with the width of the resonances.

5.4.1 Widths and Masses of Resonances

Particle Data Group [30] values for widths and masses of resonances (Table 5.1) were used in the fit. To estimate the effect of errors on those parameters on the fit results, several fits were performed by changing the widths and the masses of resonances.

As shown in Table 5.7, the variations of the fit results with widths of the resonances were small. They were within statistical errors and unlikely to introduce any major systematic error. Similar comparisons done with changing the masses of resonances within errors showed that such effects were also negligible.

5.4.2 Systematic Differences between Monte Carlo and Data

This analysis depend heavily on Monte Carlo calculations of E_{ij} which take account of the relative efficiency throughout phase space. The systematic uncertainty due to differences between data and Monte Carlo was estimated by performing fits with tight and loose cuts (same as used in section 4.4.2).

As seen in the results in Table 5.8, the variation of results with different cuts

	tight cuts	optimized cuts	loose cuts
f_1	0.55 ± 0.43	0.68 ± 0.63	0.34 ± 0.39
f_2	0.18	0.19	0.16
f_3	0.17 ± 0.10	0.13 ± 0.07	0.10 ± 0.14
f_4	0.46 ± 0.36	0.59 ± 0.58	0.87 ± 0.78
f_5	0.08 ± 0.07	0.12 ± 0.12	0.05 ± 0.07
f_6	0.10 ± 0.20	0.05 ± 0.10	0.07 ± 0.15
f_7	0.08 ± 0.07	0.02 ± 0.04	0.02 ± 0.04
f_8	0.00	0.00	0.00
f_9	0.00	0.00	0.00
f_{10}	0.00	0.00	0.00
f_{11}	0.00	0.00	0.00
α_1	1.27 ± 0.40	1.69 ± 0.43	1.36 ± 0.82
α_2	0.00	0.00	0.00
α_3	2.25 ± 0.26	3.19 ± 0.48	-1.67 ± 1.67
α_4	-1.44 ± 0.42	-1.59 ± 0.45	-1.10 ± 0.73
α_5	-0.54 ± 0.57	-1.23 ± 0.53	-1.21 ± 0.97
α_6	4.24 ± 0.43	-3.08 ± 0.76	-3.04 ± 0.91
α_7	0.27 ± 0.61	0.84 ± 1.22	-0.12 ± 1.50
α_8	0.00	0.00	0.00
α_9	0.00	0.00	0.00
α_{10}	0.00	0.00	0.00
α_{11}	0.00	0.00	0.00
$\frac{\phi}{total}$	0.20 ± 0.13	0.17 ± 0.051	0.22 ± 0.08

Table 5.8: Fit results with different cuts applied on $KK\pi\pi$ events

are within the statistical errors. Therefore no systematic error was considered to be introduced from differences in Monte Carlo and data. This also shows that errors due to any biases of the event sample used are within statistical errors.

5.4.3 Width, Mass and Background of D^0 signal.

In the fit, the width, the mass and the slope of the background were fixed at values determined by a fit with no resonances. This reduced the number of floating parametrs of the fit and made the fit faster. Fits done allowing these parameters to float in the fit converged to same values. So there were no systamatic effects due to width mass or background slope were expected.

5.4.4 Finite size of the Monte Carlo Sample Used:

In calculating phase space integrals, it was assumed that the Monte Carlo samples filled phase space adequately. Table 5.9 shows the variation of N_i and E_{ij} calculated with different subsets of the event sample used. With a sample of 90% of the Monte Carlo, normalizations N_i have converged better than 0.1% and E_{ij} better than 1%.

To estimate the error due to a possible 1% uncertainty on E_{ij}, several fits were performed by randomly fluctuating E_{ij}s by 1%. There was 10% variation of fractions calculated from fit results averaged over large number of fits. Phase angles were consistent within errors.

5.4.5 Possible Presence of Additional Amplitudes

There is a variation of normalized fractions with different decay modes present due to possible interference effects. The systematic error for this was estimated by taking the variance of the results form the the fits which have possible interferences.

% of the MC sample	50%	70%	80%	90%
A_1	1.000000	1.000000	1.000000	1.000000
A_2	1.000958	0.999613	1.000867	1.003638
A_3	0.996640	0.992866	0.998515	1.003509
A_4	0.999232	1.001826	1.000892	0.999672
A_5	1.011632	0.999275	0.995832	1.001621
A_6	1.002421	1.002090	1.000531	1.000454
A_7	1.000140	1.000705	0.999162	1.001089
A_8	0.998605	1.002523	1.001659	1.000259
A_9	0.997691	1.000218	1.000007	1.000047
A_{10}	1.002742	1.002144	1.000613	1.000526
A_{11}	0.999692	1.000282	0.998968	1.001104
$E_{1,1}$	1.000000	1.000000	1.000000	1.000000
$E_{2,2}$	0.968701	0.986766	0.978386	0.991619
$E_{3,3}$	0.966682	0.971990	0.958721	0.994248
$E_{4,4}$	1.002229	1.004641	1.004434	1.003511
$E_{5,5}$	0.958499	0.963877	0.975200	0.989918
$E_{6,6}$	0.977693	0.987057	0.989270	0.998115
$E_{7,7}$	0.992035	0.993718	0.998160	0.996399
$E_{8,8}$	1.002104	1.004914	1.003310	1.004803
$E_{9,9}$	1.001488	1.000281	1.000369	0.999903
$E_{10,10}$	0.976899	0.986914	0.989110	0.998054
$E_{11,11}$	0.991586	0.993303	0.997670	0.995939

Table 5.9: N_i and E_{ij} calculated with different subsets of Monte Carlo samples used. All values are normalized to the values from the full sample

decay mode	$\phi+$ other	$\phi\rho$	$\overline{K^{*0}}K^{*0}$
error from E_{ij} %	10	10	10
error from N_P %	31	31	28
error possible % extra amplitudes	12	21	30
Total %	35	38	42

Table 5.10: Estimate of systematic errors for fractional contributions

decay mode	fractional contribution
$\phi+$ other	$0.18 \pm 0.051 \pm 0.063$
$\phi\rho$	$0.21 \pm 0.10 \pm 0.08$
	< 0.37 90% confidence
$\overline{K^{*0}}K^{*0}$	$0.13 \pm 0.10 \pm 0.06$
	< 0.28 90% confidence

Table 5.11: Fractional contributions with systematic errors

5.4.6 Error in N_p

There is an error in the normalization N_p (Equation 5.28) which has not been included in the results of the table 5.4. Since this is an uncertainty in the fraction, not in the significance of the fraction, the error in N_p also is taken as an systematic error. Including these errors in fractional contributions, estimates of systematic errors are given in Table 5.11. Since $\overline{K^{*0}}K^{*0}$ is not statistically significant it is expressed as an upper limit.

5.5 Goodness of the Fit

The ability of the fit to extract correct parameters form a given distribution was tested with Monte Carlo generated with known distributions. Monte Carlo events

parameter	generated at	value from the fit
A_1, non-res.	1.8882	1.6777 ± 0.5384
A_2, $\phi\rho$	1.0000	1.0000 ± 0.0000
A_3, $\phi\pi\pi$	0.8507	0.8418 ± 0.1712
A_4, ρKK	1.7421	1.3565 ± 0.4791
A_5, $K^{*0}\overline{K^{*0}}$	0.7704	0.7381 ± 0.2649
A_6, $K^{*0}K\pi$	0.3709	0.3339 ± 0.1746
A_7, $\overline{K^{*0}}K\pi$	0.2692	0.2751 ± 0.2238
α_1	1.7067	1.9688 ± 0.4190
α_2	0.0000	0.0000 ± 0.0000
α_3	3.1611	3.1626 ± 0.2448
α_4	-1.5446	1.5175 ± 0.4595
α_5	-1.3166	-1.2823 ± 0.5582
α_6	-3.0280	2.1793 ± 0.9592
α_7	0.7352	0.7304 ± 0.7273

Table 5.12: Fit results for Monte Carlo events generated with a given distribution

corresponding to results of different fits to data were generated (in fact selected) by a random number throw away method. From a sample of $D^0 \to KK\pi\pi$ phase space Monte Carlo events which passed all analysis cuts, for each event $r = \mathcal{P}_S/\mathcal{P}_{S\ Max}$ was calculated, where $\mathcal{P}_S$ is the probability for the event to be a signal event for a given set of A_i and α_i (as defined in 5.2). The event was kept if a random number generated between 0 and 1 was less than r. The resulting sample had the structure corresponding to the given distribution. (Figure 5.5). Table 5.12 shows the results of a fit with a known distribution produced this way. From 5.5 million Monte Carlo events generated, there were 17,000 events which passed the analysis cuts. Out of these, 135 events passed the above selection process. Within errors fit results were in very good agreement with the generated values.

Table 5.13 shows the different fit results for Monte Carlo events generated similar to fit 1 results. With different amplitudes fit results follow that of data very closely.

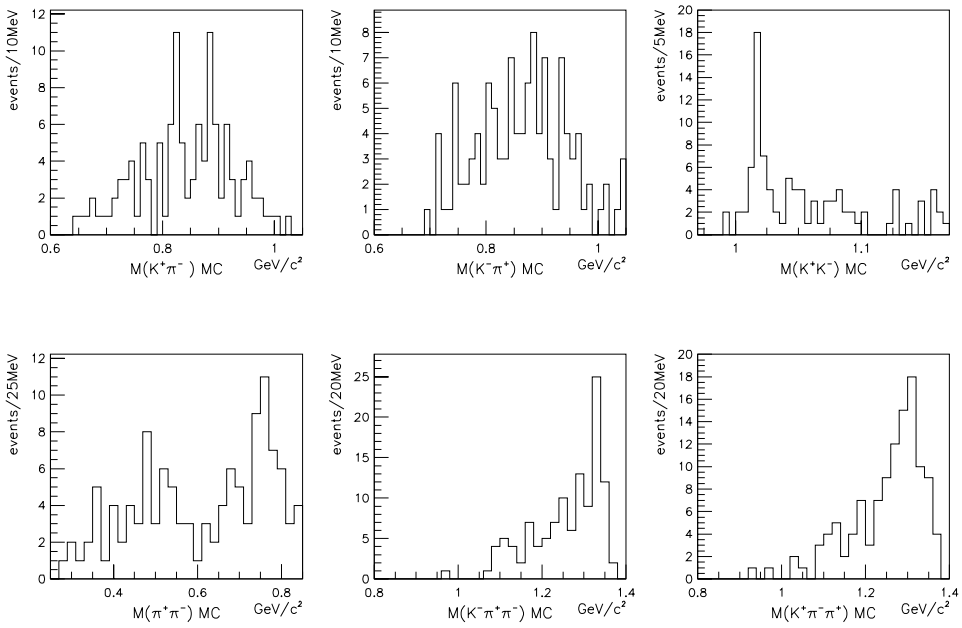

Figure 5.13: Mass distributions from Monte Carlo events generated according to fit results

A_1, non-res.	1.70 ± 0.49	1.66 ± 0.50	1.74 ± 0.48	0.55 ± 0.12	0.00	1.71 ± 0.53
A_2, $\phi\rho$	1.00	1.00	1.00	1.00	1.00	1.00
A_3,$\phi\pi\pi$	0.87 ± 0.17	0.87 ± 0.16	0.87 ± 0.18	0.63 ± 0.07	0.81 ± 0.11	0.86 ± 0.19
A_4,ρK^+K^-	1.31 ± 0.45	1.15 ± 0.42	1.32 ± 0.44	0.00	0.85 ± 0.16	0.49 ± 1.22
A_5, $K^{*0}\overline{K^{*0}}$	0.71 ± 0.24	0.64 ± 0.18	0.00	0.40 ± 0.13	0.77 ± 0.18	0.68 ± 0.26
A_6,$K^{*0}K\pi$	0.36 ± 0.19	0.00	0.71 ± 0.21	0.17 ± 0.10	0.62 ± 0.18	0.32 ± 0.22
A_7,$\overline{K^{*0}}K\pi$	0.28 ± 0.22	0.00	0.29 ± 0.15	0.17 ± 0.14	0.19 ± 0.17	0.19 ± 0.24
A_8,$K^{*+}(1270)$	0.00	0.00	0.00	0.00	0.00	0.48 ± 0.79
A_9,$K^{*-}(1270)$	0.00	0.00	0.00	0.00	0.00	0.63 ± 0.76
A_{10},$K^{*+}(1410)$	0.00	0.00	0.00	0.00	0.00	0.00
A_{11},$K^{*-}(1410)$	0.00	0.00	0.00	0.00	0.00	0.00
α_1, non-res.	1.71 ± 0.41	1.95 ± 0.42	1.84 ± 0.42	0.85 ± 0.40	0.00	1.90 ± 0.45
α_2, $\phi\rho$	0.00	0.00	0.00	0.00	0.00	0.00
α_3, $\phi\pi\pi$	9.36 ± 0.25	-3.24 ± 0.22	3.14 ± 0.22	2.63 ± 0.13	2.60 ± 0.12	3.12 ± 0.25
α_4, ρK^+K^-	4.94 ± 0.46	11.11 ± 0.46	5.05 ± 0.44	0.00	16.95 ± 0.34	5.03 ± 1.84
α_5, $K^{*0}\overline{K^{*0}}$	-1.36 ± 0.54	-7.73 ± 0.54	0.00	-3.17 ± 0.43	1.53 ± 0.33	-1.34 ± 0.54
α_6, $K^{*0}K\pi$	8.95 ± 0.84	0.00	3.68 ± 0.51	0.90 ± 0.91	2.81 ± 0.33	2.73 ± 0.96
α_7, $\overline{K^{*0}}K\pi$	0.49 ± 0.77	0.00	-1.83 ± 0.75	-1.20 ± 0.65	2.02 ± 0.96	0.75 ± 1.11
α_8, $K^{*+}(1270)$	0.00	0.00	0.00	0.00	0.00	5.77 ± 1.14
α_9, $K^{*-}(1270)$	0.00	0.00	0.00	0.00	0.00	4.44 ± 1.05
α_{10}, $K^{*+}(1410)$	0.00	0.00	0.00	0.00	0.00	0.00
α_{11}, $K^{*-}(1410)$	0.00	0.00	0.00	0.00	0.00	0.00
f_1, non-res.	0.73 ± 0.42	0.73 ± 0.45	0.74 ± 0.41	0.29 ± 0.13	0.00	0.72 ± 0.45
f_2, $\phi\rho$	0.25	0.27	0.25	0.96	0.61	0.25
f_3, $\phi\pi\pi$	0.19 ± 0.07	0.20 ± 0.08	0.18 ± 0.08	0.37 ± 0.09	0.39 ± 0.11	0.18 ± 0.08
f_4, ρK^+K^-	0.43 ± 0.30	0.35 ± 0.25	0.43 ± 0.28	0.00	0.43 ± 0.16	0.06 ± 0.29
f_5, $K^{*0}\overline{K^{*0}}$	0.13 ± 0.09	0.11 ± 0.06	0.00	0.16 ± 0.10	0.36 ± 0.17	0.11 ± 0.09
f_6, $K^{*0}K\pi$	0.03 ± 0.03	0.00	0.12 ± 0.07	0.03 ± 0.03	0.23 ± 0.13	0.02 ± 0.03
f_7, $\overline{K^{*0}}K\pi$	0.02 ± 0.03	0.00	0.02 ± 0.02	0.03 ± 0.04	0.02 ± 0.04	0.01 ± 0.02
f_8,$K^{*+}(1270)$	0.00	0.00	0.00	0.00	0.00	0.06 ± 0.19
f_9, $K^{*-}(1270)$	0.00	0.00	0.00	0.00	0.00	0.10 ± 0.23
f_{10}, $K^{*+}(1410)$	0.00	0.00	0.00	0.00	0.00	0.00
f_{11}, $K^{*+}(1410)$	0.00	0.00	0.00	0.00	0.00	0.00
$\frac{\phi}{total}$	0.21 ± 0.03	0.21 ± 0.03	0.22 ± 0.03	$0.470.05\pm$	0.29 ± 0.03	0.21 ± 0.03
$-2\ln\mathcal{L}$	1466.162	1471.538	1477.778	1472.590	1463.229	1465.01

Table 5.13: Fit results with different amplitudes for Monte Carlo events generated according to fit 1 results of Table 5.4

Chapter 6

Conclusions

From the analysis described in this thesis, the branching ratio of the Cabibbo suppressed decay $D^0 \to K^+K^-\pi^+\pi^-$ is estimated to be $0.254 \pm 0.030 \pm 0.033$ %.

There is a 2 σ $D^0 \to \phi\rho$ mode. The fit fails to find any statistically significant contributions from other modes. Interference among amplitudes makes it difficult to distinguish between modes which differ only by broad Breit-Wigners (as in the case of ρKK compared to the non-resonant mode). Large errors in fit results reflect this uncertainty.

The presence of $D^0 \to K^{*0}\overline{K}^{*0}$ mode is not very significant, and its fractional contribution is estimated to be < 0.28 at 90% confidence level. Although invariant mass distributions (Figure 5.2-5.4) show excess events in $K\pi\pi$ mass distributions, the fits do not find significant contributions from higher mass resonces. So the apparent enhancement may result from the presence of a strong ϕ signal (Figure 5.7). Also, there is no convincing evidence for modes $K^{*0}K\pi$. With our limited statistics, we cannot make any quantitative estimates of these modes. The results of Chapter 5 are not conclusive enough to rule out non-resonant or three body modes.

A comparison of this $D^0 \to K^+K^-\pi^+\pi^-$ branching ratio measurement with other

experimental measurements is given in the Table 6.1. The results in table 5.10 have been converted to relative branching ratio using the relative branching ratio of $D^0 \rightarrow K^+K^-\pi^+\pi^-$ given in chapter 4. Also, PDG branching ratios for $\phi \rightarrow K^+K^-$ and $K^{*0} \rightarrow K^+\pi^-$ have been used in calculating the branching ratios presented here.

decay mode (f)	$\frac{BR(D^0 \rightarrow f)\times 100}{BR(D^0 \rightarrow K^-\pi^+\pi^-\pi^+)}$				
	E791	E691 (1991)	CLEO (1991)	ARGUS(1994)	E687(1995)
inclusive	$3.13 \pm 0.37 \pm 0.36$	$2.8^{+0.8}_{-0.7}$	3.14 ± 1.0	$4.1 \pm 0.7 \pm 0.5$	$3.4 \pm 0.4 \pm 0.4$
non-resonant		$1.0^{+1.1}_{-0.1}$			< 1.1 (90% CL)
$D^0 \rightarrow K^{*0}\overline{K}^{*0}$	< 2 (90/% CL)	$3.6^{+2.0}_{-1.6}$	< 3.3 (90% CL)		1.6 ± 0.6
$D^0 \rightarrow K^{*0}K^-\pi^+$		$01.0^{+1.6}_{-1.0}$		$4.3 \pm 1.4 \pm 0.9$	< 1.7 (90% CL)
$D^0 \rightarrow \overline{K}^{*0}K^+\pi^-$				$2.3 \pm 1.3 \pm 0.9$	
$D^0 \rightarrow \phi\pi^+\pi^-$	$0.18 \pm 0.05 \pm 0.06$	$0.76^{+0.66}_{-0.49}$			< 0.6 (90% CL)
$\phi\rho$	$1.40 \pm 0.6 \pm 0.5$		2.4 ± 0.6	$2.0 \pm 0.6 \pm 0.5$	0.5 ± 0.3
$K^+K^-\rho$					0.5 ± 0.3

Table 6.1: Comparison of E791 (this thesis results) with other measurements.

As mentioned earlier, the E791 estimated fractional contributions have larger errors than some other measurements. This results from allowing amplitudes to interfere. But it is the correct description of the underlying physical process, and a correct description of the uncertainty.

Table 6.2 shows some results compared with theoretical predictions. $D^0 \rightarrow K^+K^-\pi^+\pi^-$ branching ratio was used to convert results inTable 5.11 to branching ratios. Since the errors on them are large, they do not strongly support or rule out one prediction or another. Within errors, they agree with all the predictions.

The results are not conclusive enough to observe whether GIM suppression is

occurring in $K^{*0}\overline{K}^{*0}$, $K^{*0}K^{+}\pi^{-}$ and non-resonant modes. The clear signal in the $\phi\rho$ mode is mostly due to the narrow width of the ϕ rather than its large fraction. The contribution from $K^{*0}K^{+}\pi^{-}$ seems to be low. Again, this may be due to interference with $K(1400)K^{+}$ mode. Within the statistical power of E791, it is not possible to see if such suppression actually occurs.

Decay	Branching ratio %			
		Theory		
	E791	BSW	BDM	KVS
$D^0 \to \phi\rho$	$0.12 \pm 0.051 \pm 0.045$	0.1 ± 0.03	0.022	0.026-0.08
$D^0 \to K^{*0}\overline{K^{*0}}$	< 0.2 (90% CL)		0.0026	

Table 6.2: Comparison of E791 results with theoretical predictions

Appendix A

Widths and Form Factors

To simplify the formulation, fixed partial widths were used in signal amplitudes and momentum dependent form factors were ignored. Possible effects of this on the fit results will be examined here.

Most of the resonances have broad natural widths, and the detector resolution has no significant effect on them. However the natural width of ϕ is about 1.5 MeV, which is below the resolution of the detector. Widths and their dependence on the signal amplitudes for ϕ and $K^{*0}(892)$ were studied fitting to relatively clean large ϕ and $K^{*0}(892)$ real events (which came from $D^+/D^{s+} \rightarrow K^+K^-\pi^+$). The signal amplitude was fitted with

$$\frac{\sqrt{,}}{(m^2 - m_0^2) + i(m_{0,\ 0})} \frac{1}{\sqrt{1 + R^2 p_{cm}^2}} \tag{A.1}$$

and a linear background. Here , $\propto p_{cm}^2$ is the partial width and p_{cm} is the decay particle momentum in the resonant rest frame.

As a means of study the effects of the form factor and momentum dependant partial width fit was done with different values of R and with , $= p^{2L}$ and , $= 1$.

R	signal	mean (m_0) GeV	width ($,_0$) GeV	χ^2/N
0	815 ± 46	1.02 ± 0.0002	0.006 ± 0.0005	0.813
2.5	816 ± 46	1.02 ± 0.0002	0.006 ± 0.0005	0.815
5.0	807 ± 45	1.02 ± 0.0002	0.006 ± 0.0005	0.822
7.5	804 ± 45	1.02 ± 0.0002	0.006 ± 0.0002	0.835
10.0	803 ± 45	1.02 ± 0.0002	0.006 ± 0.0002	0.848
$\phi \to K^+K^-$ with $, = p^2_{cm}$				
0	817 ± 47	1.02 ± 0.0002	0.006 ± 0.0005	0.891
2.5	816 ± 47	1.02 ± 0.0002	0.006 ± 0.0005	0.906
5	818 ± 47	1.02 ± 0.0002	0.006 ± 0.0005	0.940
7.5	824 ± 47	1.02 ± 0.0002	0.006 ± 0.0005	0.977
10	832 ± 49	1.02 ± 0.0002	0.006 ± 0.0005	1.005
$\phi \to K^+K^-$ with $, = 1$				
0	933 ± 89	0.893 ± 0.0002	0.0453 ± 0.006	0.638
2.5	922 ± 87	0.894 ± 0.002	0.0452 ± 0.006	0.618
5	921 ± 86	0.895 ± 0.002	0.0449 ± 0.006	0.602
7.5	924 ± 87	0.895 ± 0.002	0.0448 ± 0.006	0.597
10	927 ± 87	0.896 ± 0.002	0.0448 ± 0.006	0.595
$K^{*0}(892) \to K^+\pi^-$ with $, = p^2_{cm}$				
0	931 ± 88	0.896 ± 0.002	0.0447 ± 0.006	0.591
2.5	934 ± 89	0.897 ± 0.002	0.044 ± 0.006	0.583
5	947 ± 95	0.897 ± 0.002	0.0441 ± 0.006	0.579
7.5	959 ± 97	0.898 ± 0.002	0.0442 ± 0.006	0.578
10	832 ± 49	1.02 ± 0.002	0.0441 ± 0.006	0.577
$K^{*0}(892) \to K^+\pi^-$ with $, = 1$				

Table A.1: Fit results for $K^{*0}(892)$ and ϕ

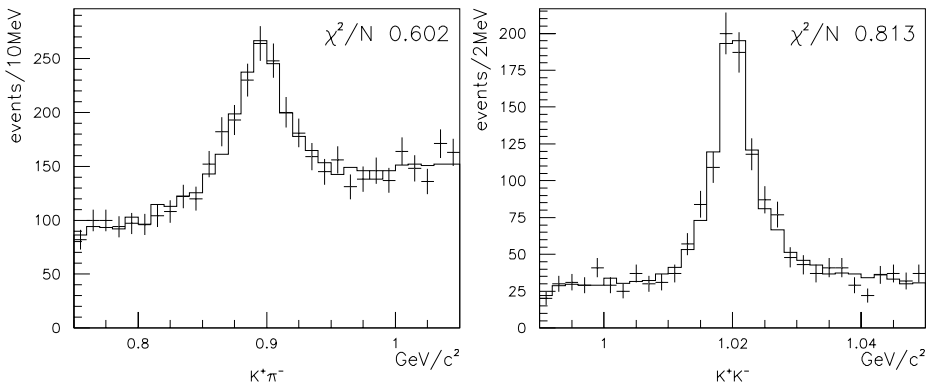

Figure A.1: projections of the fit for $K^{*0}(892) \to K^+\pi^-$ and $\phi \to K^+K^-$ signals.

Results shown in the table A indicate that there is not much effect from the form factor and the momentum dependent width on the fit results (at least for K^{*0} and ϕ).

Bibliography

[1] M. Wise, in Proceedings of the International Symposium on Heavy Flavour Physics, Montreal,1993. Editions Frontieres, (1994). p.5.

[2] I.I Bigi, On Charm Decays- Present Status and Future Goals, in Charm Physics, editors Ming-han Ye and Tao Huang,(Gordon and Breach) p. 339.

[3] D. F. DeJongh, PhD thesis, California Institute of Technology (1990)

[4] H. Albrecht *et el*, Physics Letters B 308, (1993) , p.435

[5] P.L. Frabetti *et el*, Physics Letters B 331 (1994) p.217

[6] J. F. Donoghue, Phys Lett. 193B, (1986) p.331

[7] M. Bauer, B. Stech and M Wirbel, Z. Physics. 34 (1987) p.103

[8] R. S. Orr, Heavy Flavor Decay and Mixinging in Selected Topiccs in Electroweak Interations. Editor J. M. Cameron, World Scientific (1987). p. 1

[9] P. Renton, Electro Week Interactions, Cambridge University Press (1990).

[10] Ammar *et el*, Physical Review D44, (1991), p.3383.

[11] Albrecht *et el*, Z. Physics. C64 (1994), p.375

[12] Anjos *et el*, Phys Rev. D 43 (1991), R6351.

[13] C. J. Kennedy, PhD Thesis. University of Norte Dame. (1993). P.L. Frabetti *et al.* Physics Letters B 354 (1995) p. 486.

[14] P. Bedaqu, A. Das and V.S. Mathur Physical Review D, (1994) p.269

[15] A.N. Kamal, R.C.Verma and N.Sinha, Physical Review D43 (1991) p. 843

[16] D. Barlett *et el*, Nuclear Instruments and Methods A260, (1987) p.55.

[17] J. Dinkel *et el*, Nuclear Instruments and Methods A138, (1976) p.567.

[18] J. A. Appel *et el*, Nuclear Instruments and Methods A243, (1986). p. 361.

[19] V. K. Bharadwaj *et el*, Nuclear Instruments and Methods A228 (1985), p. 361.

[20] S. Amato *et el*, Nuclear Instruments and Methods, A324,(1993) p. 535.

[21] E791 offline document 95.

[22] E791 offline document 140.

[23] E791 offline document 125.

[24] E791 offline document 239, S. Bracker *et el* Submitted to Nuclear Instruments and Methods (1995).

[25] Pythia 5.7 and Jetset 7.4 Physics and Manual. CERN-TH-7112/93 (1993)

[26] MINUIT reference Manual, CERN Program Library Long Writeup. D506, PM0020, (1994).

[27] D. H. Perkins, Introduction to High Energy Physics, Addison Wesley, (1987)., p. 424,p.119

[28] J. D. Jackson, Nuovo Cimento Vol.XXXIV, N.6. (1964), 1645.

[29] Blatt and Weisskopf, Theoretical Nuclear Physics, Wiley (1952), p. 361.

[30] Physical Review D, Particles and Fields, August 1994.

[31] J.D. Richman, California Institute of Technology Pre Print. CALT-68-1148 (1984)